



HAL
open science

Microlasers based on polymer composites

Nina Sobeshchuk

► **To cite this version:**

Nina Sobeshchuk. Microlasers based on polymer composites. Optics / Photonic. Université Paris Saclay (COmUE); ITMO University, 2015. English. NNT : 2015SACLN031 . tel-01304906

HAL Id: tel-01304906

<https://theses.hal.science/tel-01304906>

Submitted on 20 Apr 2016

HAL is a multi-disciplinary open access archive for the deposit and dissemination of scientific research documents, whether they are published or not. The documents may come from teaching and research institutions in France or abroad, or from public or private research centers.

L'archive ouverte pluridisciplinaire **HAL**, est destinée au dépôt et à la diffusion de documents scientifiques de niveau recherche, publiés ou non, émanant des établissements d'enseignement et de recherche français ou étrangers, des laboratoires publics ou privés.

NNT : 2015SACLN031



DOCTORATE THESIS
OF
ITMO UNIVERSITY
AND
UNIVERSITÉ PARIS-SACLAY
PREPARED IN ITMO UNIVERSITY AND ENS CACHAN

ÉCOLE DOCTORALE N°575
Ecole doctorale Electrical, Optical, Bio - physics and Engineering (EOBE)

Speciality: Physics

By

Nina SOBESHCHUK

Micro-lasers based on polymer composites

Thesis defended in St Petersburg, the 16th of December 2015

Members of the French jury:

Valery BARACHEVSKY
Sébastien CHENAIS
Igor DENISYUK
Mélanie LEBENTAL
Rober PANSU
Marco ROMANELLI

Russian Academy of Science
Paris XIII University
ITMO University
ENS Cachan
ENS Cachan
University of Rennes I

Reviewer
Reviewer
Thesis supervisor
Thesis supervisor
Head of the jury
Examinator

Abstract

The aim of the thesis is the fabrication and optical characterization of three-dimensional organic microlasers based on organic dyes and luminescent erbium/ytterbium nanoparticles.

At the beginning, we considered formation of submicron polymer structures with high aspect ratio, as well as the phenomenon of redistribution of nanoparticles in the volume of the composite during the exposure by a periodic light pattern.

The main part of the work is devoted to obtaining three-dimensional polymer microlasers by UV-lithography. Comparison of the lasing threshold for microcavities obtained by different methods was performed. Periodic orbits in cuboid microlasers with square cross-section were identified. Analysis of possible periodic orbits in microlasers Fabry-Perot showed that the shape of the orbit depends on the dye, the type of substrate and the size of the microlaser (width, height).

The last part of the work contains a study of low-temperature synthesis of luminescent nanoparticles of erbium and ytterbium oxides in an anhydrous medium and polymer composites based on them. Three dimensional organic microlasers doped by these luminescent nanoparticles were obtained and investigated.

Acknowledgments

First of all I would like to thank my both advisors: Melanie Lebental and Igor. Yu. Denisyuk. I thank Igor Denisyuk for long-term fruitful collaboration and assistance. I'm very grateful to Melanie Lebental for giving me opportunity to perform such interesting project. I also thank her for her help with experimental work and especially for her patience and positive attitude in the aspects not directly connected with the work.

I also want to thank Isabelle Ledoux-Rak and Service des relations internationales for the possibility of carrying out my joint PhD project in LPQM department of ENS Cachan. I express my gratitude to all the members of the jury for a positive assessment of my work and valuable comments.

My sincere thanks to all staff of Department of Engineering Photonics and Quantum and Molecular Photonics Laboratory. For help with the experiments and measurements I thank Joseph Lautru, Andrey Veniaminov and Dominique Decanini.

Special thanks for my colleagues - Vera Bulgakova, Stefan Bittner and Clement Lafargue.

Personal thanks to Mikhail Pakhnin, Eugenio Efimov and Victoriia I. Sobeshchuk for their help and support.

TABLE OF CONTENTS

INTRODUCTION.....	1
CHAPTER 1. ANALYTICAL REVIEW	7
1.1 Microlasers.....	7
1.2 2D and 3D microlasers	9
1.3 Nanoparticles and nanocomposites.....	11
Chapter 1 conclusions.....	14
CHAPTER 2. SELF-ORGANIZATION PROCESSES IN POLYMERS AND NANOCOMPOSITES	15
2.1 Self-organization processes in polymers	15
2.2 Self-organization processes in nanocomposites	24
2.2.1 Materials	25
2.2.2 Fabrication of polymer composites and nanocomposites	27
2.2.3 Movement of nanoparticles during the holographic recording.....	28
2.2.4 Fabrication of subwavelength structures by projection lithography.....	29
Chapter 2 conclusions.....	32
Chapter 3. FABRICATION OF THREE-DIMENSIONAL ORGANIC MICROLASERS	33
3.1. Projection lithography.....	33
3.2. UV-lithography	34
3.2.1 Materials: polymers and dyes	35
3.2.2 Structures fabrication	38
3.3. Direct laser writing by two-photon polymerization (2PP)	45
Chapter 3 conclusion.....	49

Chapter 4. CHARACTERIZATION OF 3D-MICROLASERS	50
4.1 The measurement setup	50
4.2. Tresholds measurements.....	52
4.3 Spectra and periodic orbits	54
4.3.1 Periodic orbits in three-dimensional cuboid microlasers.....	56
4.3.2 Refractive index determination	59
4.3.3 Periodic orbits in three dimensional Fabry-Perot microlasers	61
Chapter 4 conclusions.....	79
CHAPTER 5. LUMINESCENT RARE EARTH OXIDE NANOPARTICLES.....	82
5.1 Materials	82
5.2 Synthesis of nanoparticles	82
5.2.1 Syntheses I and II	83
5.2.2 Synthesis III and IV.....	84
5.3 Introduction of nanoparticles into polymer matrix.....	85
5.4 Study of synthesized nanoparticles.....	86
5.5 Study of nanocomposites	93
5.6 Fabrication of three-dimensional polymer microlasers based on inorganic luminescent nanoparticles.....	95
Chapter 5 conclusions	98
GENERAL CONCLUSIONS	99
BIBLIOGRAPHY	100
ANNEX A	112
ANNEX B	114

INTRODUCTION

The development of optical communication systems shows a tendency towards the miniaturization of its components and optical sensors. The focus is on the production of all elements within a single microchip, when all the components are produced within a single production cycle. It is important to design and fabricate microelements using the planar process, without prefabricated parts or alignment. One of the critical elements of the microchip is the frequency generator for the DWDM system.

The study presented in this thesis provides theoretical analysis and experimental verification of the new physical principles of laser generation in three-dimensional microresonators.

A single production cycle is incompatible with interconnection components. Microresonator is a structure in which the light travels in a closed loop — along a circle, or repetitively reflecting from the sides. The well-known examples are single wavelength microring lasers and micron-sized circular or square planar resonators. In all cases, the light is generated by luminescence and stimulated emission. Its spectrum is determined by the geometry of the resonator and the nature of the active medium. Pumping is provided by the excitation of the luminescent substance introduced into the resonator by an external narrow band laser.

The most important and challenging open research topics include developing a laser that would generate frequency grid for the large number of channels in the DWDM system, and improving the robustness of the luminescent substance in comparison with the currently used organic luminophores.

This thesis addresses both of these research topics by studying 3D microresonator generating a frequency grid according to its geometry. To increase the durability, the luminescent organic dye is replaced with erbium oxide nanoparticles. The synthesis of nanocomposite with erbium nanoparticles is also studied.

Ideally, a 3D microresonator is a cube or a cylinder about 100 μm in size with flat surfaces and straight angles which contains the light beam. Important parameters that determine the Q factor of the resonator are:

- minimum light scattering losses;
- accurate value of the angle between the sides, so that light travels along a closed trajectory;
- minimum surface roughness;
- gap between the resonator and the substrate.

According to the above requirements, the following issues were studied:

- theoretical and experimental estimates of microresonator radiation properties;
- fabrication method of the luminescent nanocomposite with low light scattering, which can be used as a material for 3D microresonators fabrication by photolithography;
- self-focusing of light in the photopolymer medium by changing the photopolymerization conditions. This is needed to control the angle of the vertical side wall relative to the substrate surface, and thus to form 3D structures with vertical side walls at right angles with the substrate surface;
- surface roughness and the deformation of the surface due to polymer shrinkage.

The thesis consists of several independent chapters related to a common research objective.

The main **objects of the study** are three-dimensional polymer organic microlasers and luminescent acrylic nanocomposites. Cuboid and Fabry-Perot microlasers based on the SU-8 negative photoresist doped with fluorescent dyes Pyrromethene 597 and Rhodamine 640 were fabricated by UV-lithography. Nanocomposites fabricated based on Er and Yb nanoparticles were obtained by low temperature synthesis.

The main **research objectives** are:

1. Study of three-dimensional polymer microresonators, required materials and fabrication methods.
2. Analysis of the fabricated microlasers and their emission spectrum characteristics, comparison of the lasing thresholds and investigation of periodic orbits in simply shaped microlasers.
3. Study of luminescent Er and Yb nanoparticles synthesis with and without silica nanoparticles in an anhydrous alcoholic medium.

In order to reach the research objectives, the following **tasks** should be accomplished:

1. Select a technology and optimize its parameters to obtain three-dimensional structures with high vertical side walls, low surface roughness and low shrinkage. Find the optimal method to introduce an organic dye into the polymer matrix.
2. Study the emission spectrum characteristics of microlasers fabricated by different techniques.
3. Analyze the dependence of the spectral shape and periodic orbits on the shape of the microlaser, type of the dye and the substrate material.
4. Study the methods of the luminescent nanoparticles low temperature synthesis in liquid anhydrous medium. Compare the obtained results with the standard high temperature synthesis results.
5. Introduce the synthesized nanoparticles into the polymer composite and photoresist. Study the possibility of fabrication of organic microlasers doped with inorganic nanoparticles.

The originality of the research work is that it is the first study in which

1. Three-dimensional organic microlasers are fabricated based on the SU-8 photoresist doped with fluorescent dyes. The width/length of the microlasers is 20–150 μm , and the height is 10–150 μm . Coherent generation in three-dimensional cubic and Fabry-Perot microresonators is obtained.
2. Lasing thresholds for the microresonators fabricated by different techniques (UV lithography, two-photon polymerization, microlasers on the substrate and

microlasers decoupled from substrate) are compared. It is shown that the lasing threshold for microlasers fabricated by two-photon polymerization is two or three times lower than the lasing threshold for the same size and shape microlasers fabricated by UV-lithography. Hence the lasing threshold depends far more on the surface roughness of the sides than on their mutual perpendicularity.

3. Periodic orbits in the cuboid microlasers (with a square cross-section) and the Fabry-Perot microlasers are studied. It is shown that two-dimensional «diamond» periodic orbit is present in the cubic microresonators regardless of the material of the substrate, type of the dye and the size of the microlaser. It is shown that the shapes of the periodic orbits in the Fabry-Perot microlasers can be more complicated, with reflections from the horizontal facets. The configuration of these orbits depends on the material of the substrate, the type of the dye and the linear dimensions of the microlaser.
4. Transparent luminescent acrylic nanocomposite is fabricated and investigated. The nanocomposite is based on the Er and Yb oxide nanoparticles, obtained by low temperature synthesis in the presence of silica nanoparticles in an anhydrous alcoholic medium. Three-dimensional microlasers based on the SU-8 photoresist doped with inorganic luminescent nanoparticles are fabricated.

The practical significance of the study is that working samples of the three-dimensional microlasers were fabricated. These samples can be used as generators for the DWDM optical communication systems, and as optical sensors to measure various physical values.

The following **research methods and instruments** were used during the study: fabrication of polymer microstructures via projection lithography (LUMAM-I3, LOMO), UV lithography (Manual Mask Aligner MJB4, Suss MicroTec) and direct laser writing by two-photon polymerization (Lithography laser system, Nanoscribe). A polymer mask engraved by laser ablation (LaserGraver LG2500 SP47). Application of thin and thick films by spin-coating. Study of the quality of the obtained surfaces by optical microscopy (Olympus STM 6) and scanning electron microscopy (Hitachi S3400N). Measuring the sizes of the fabricated microstructures by profilometry (Veeco,

Dektak 3ST). Measuring the spectra and the lasing thresholds using the optical setup (see paragraph 4.1 for details) with a number of optical elements and devices, including spectrometer Spectra Pro 2500i (Acton Research). Study of the luminescent properties of nanoparticles and nanocomposites using the luminescent microscope Zeiss LSM-710.

Main results of the study:

1. Three-dimensional microlaser operates at a fixed set of wavelengths. For the cuboid microresonators, periodic orbits lie in a plane parallel to the substrate. For Fabry-Perot microresonators, periodic orbits lie in a plane perpendicular to the substrate.
2. The shape of periodic orbits in the Fabry-Perot microlasers depends on the type of the dye, the difference between the refractive indices of the substrate and the microresonator material, and the width of the microresonator.
3. The surface roughness of the microresonator, which depends on the fabrication technique, has the greatest impact on the lasing threshold. The impact of the deviation of the angle between the horizontal and vertical surfaces of the microresonator from 90° on the lasing threshold seems to be much smaller.
4. During the study, working samples of three-dimensional cuboid and Fabry-Perot microresonators generating a coherent fixed-wavelength grid were fabricated for the first time. The position of each band is determined by the geometry of the microresonator. The lasing threshold and the dependence of the radiation power on the pump power are determined by the parameters of the microresonator material.
5. Novel method for synthesizing luminescent Er and Yb nanoparticles with silica matrix is invented. Synthesis in the liquid anhydrous medium without high temperature anneal allows one to maintain the nanometer particle size and ensure their low light scattering.

The validity of the results and conclusions is provided by the reproducibility of the data, clear physical interpretation consistent with the current scientific knowledge, and consistency with the results of other authors known from the literature.

Major research findings were reported and discussed at 6 international conferences. The author of the thesis was three-time awarded with the grant of the St. Petersburg Government for students, postgraduates, young scientists and PhDs (2012–

2014). Main results of the study are stated in 11 articles, including 7 articles in the peer-reviewed journals (indexed by Scopus and Web of Science) and 4 publications in international conference proceedings.

The content of the thesis and main results of the study reflect the author's personal contribution. The author was involved in setting research goals and objectives, in the development of techniques and construction of experiments, as well as in the analysis of the results and forming of conclusions. Preparation for publication of the results was carried out in collaboration with co-authors, and the contribution of the author was decisive.

CHAPTER 1. ANALYTICAL REVIEW

1.1 Microlasers

In recent decades, a large number of organic solid-state lasers with various resonator types were developed [1]. The miniaturization and development of optical microchips required the fabrication of the miniature lasers within a single production cycle with other elements, which is impossible for traditional designs. Microlasers are the new micro-sized elements of integrated optics. They are designed using planar process without mounting and configuration. The parameters of the resonator depend on its geometry specified by fabrication technique [2]. Examples include microdisks [2–8], microspheres [9–12] and microcylinders [13–15], microtoroids [16–18], micropillars [19–20], etc. Both active and passive microresonators are widely used as various sensors [21–27], including biosensors [28–34], and as light sources and converters in integrated optical circuits [35–42].

SEM images in figure 1.1 are some examples of microspherical, microdisk and microtoroid resonators generating fixed-wavelength grid for optical communication systems.

Materials and fabrication techniques are also different. Organic dyes [4, 5, 43–44], quantum dots [2, 45–47], glass materials doped with rare earth ions [10, 11] can be used as the active laser medium. The fabrication techniques that are widely used include multilayer lithography [17, 48] with subsequent etching and/or melting [12, 16, 49], molecular beam epitaxy [15, 50], ion, electron or proton beam writing [4–5], self-assembly of the polymer rings [6], nanoimprint lithography [51], etc.

Organic dyes as the active laser medium have always been of interest, even despite their low radiation resistance due to a wide emission spectrum of the dyes. Dyes molecules usually consist of 20-60 atoms and as a result have over 100 of vibrational degrees of freedom. Vibrational states are grouped near the electronic states and merge that leads to such wide and continuous absorption and fluorescence spectra.

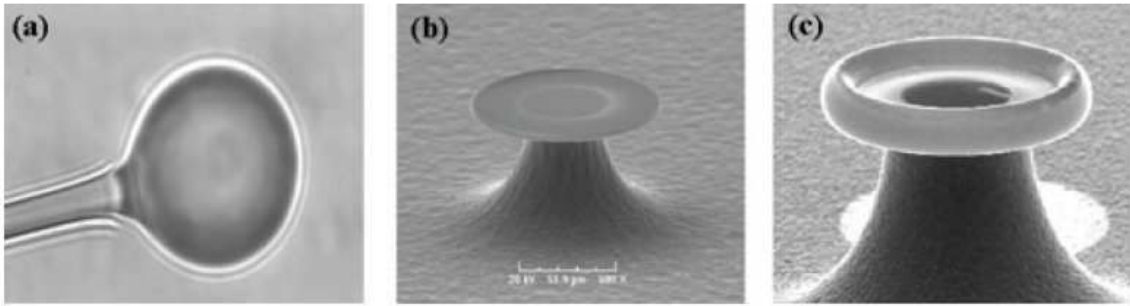


Figure 1.1 — Examples of microresonators: (a) microsphere, (b) microdisk, and (c) microtoroid [9]

Dye lasers operate in a four-level scheme. Figure 1.2 shows the energy level diagram of a typical organic dye molecule.

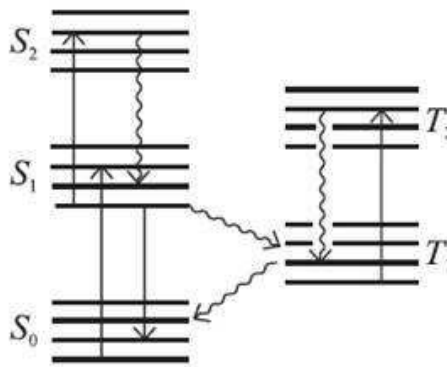


Figure 1.2 — Energy level diagram of the dye laser [52]

The molecule has two groups of electronic states: the singlet states (S_0 , S_1 , and S_2) and the triplet states (T_1 and T_2). Singlet–triplet transitions and triplet–singlet transitions are less likely, compared with singlet–singlet and triplet–triplet transitions. Under pump the molecule transits from the groundstate S_0 to the excited state S_1 , and then there is a rapid non-radiated transition within the vibration band to the lower energy states of S_1 .

Stimulated emission occurs when the molecule transits between a state near the bottom of S_1 and an intermediate state S_0 . There are many vibrational rotational sublevels within S_0 and S_1 , hence the outgoing radiation contains a large set of frequencies, i.e., the resulting emission line is very broad. The triplet states T_1 and T_2 are not directly involved in laser action. However, there is a small probability that the

excited molecule will transit to the triplet state T_1 . Since the transition $T_1 \rightarrow S_0$ is forbidden, the lifetime of the excited triplet state T_1 is quite large. If the laser operating frequency is within the triplet absorption band, the increase in the number of molecules in the excited state T_1 leads to the increase in losses, and therefore increases the lasing threshold. Therefore, many organic dye lasers are pulsed lasers. In pulsed dye lasers, steep fronts of pumping pulses create population of the state S_1 , which is required for laser action. Laser action continues until the number of molecules accumulated in the state T_1 is too large [53].

1.2 2D and 3D microlasers

All considered microlasers fall into two categories: two-dimensional and three-dimensional. 2D microlasers are the structures whose size in one dimension (height/thickness) is comparable to the wavelength, while two other dimensions are significantly greater than the wavelength. 3D microlasers are the structures whose height is comparable to the other dimensions and is much larger than the wavelength. The most common disadvantages of the various 3D microresonator fabrication techniques are small number of available shapes, impossibility to control the resulting shape, and low rate of the structure formation. Hence the simpler fabricated 2D microlasers are better studied. For more than ten years the study of two-dimensional organic microlasers [54–62] is successfully conducted by the research team in the Laboratoire de photonique quantique et moléculaire (LPQM, ENS Cachan, France). The active member of this research team is Dr. Melanie Lebental, thesis co-supervisor.

Various types of flat 2D microlasers were fabricated by UV-lithography with the subsequent reactive-ion etching [54,55]. Polymethylmethacrylate (PMMA) was used as the polymer matrix. Different organic dyes [60] were used as the active laser medium, mostly a 5%-by-mass DCM [54–56]. The polymer-dye solution (typically anisole was used as the solvent) was deposited on the wafer (silicon substrate covered by 2 μm of silica) by spin-coating and dried before exposure. Later on, the technique was modified: the structures in the polymer film were formed not by photolithography and etching, but

by electron-beam lithography [56, 62]. The height of all structures was about 400–700 nm [58], and their linear dimensions were about 100–400 μm . Figure 1.3 shows images of various two-dimensional microlasers studied in the LPQM.

Studies of their spectral characteristics were performed using the setup which will be described in detail in paragraph 4.1. Figure 1.4 shows the examples of typical spectra of 2D microlasers. Periodic orbits in the simply shaped 2D microlasers such as squares [59], Fabry-Perot [59], disks [59], triangles [62], etc., were also thoroughly studied. The spatial distribution of the microlaser radiation was analyzed, and the emission diagrams were obtained [56, 58, 62].

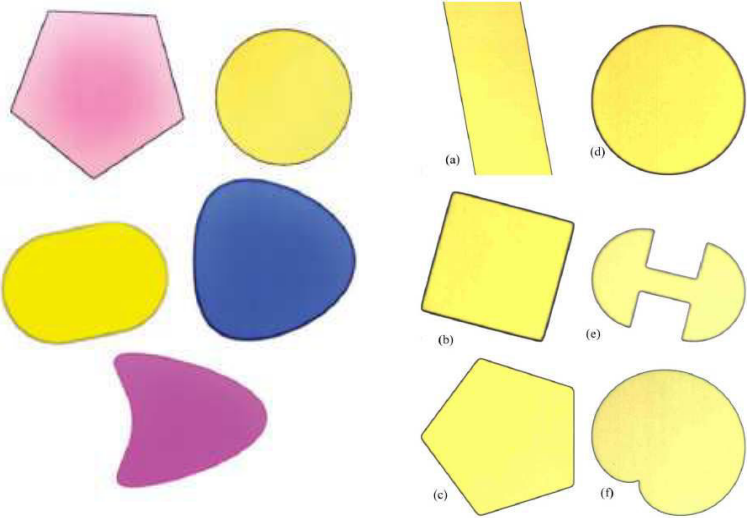


Figure 1.3 – Photos with an optical microscope in real colors of various 2D microlasers. Left: microlasers of different shapes doped with different dyes [60]; Right: microlasers of different shapes doped with a 5%-by-mass DCM [59]. Typical scale, 100 μm in-plane

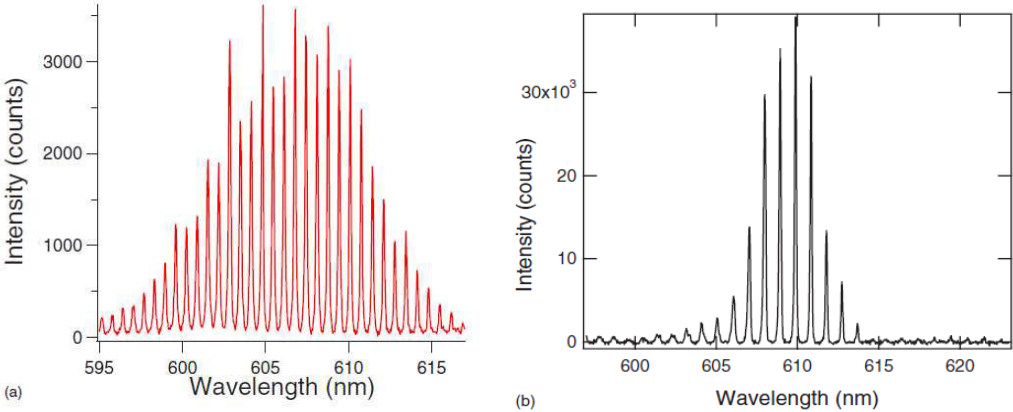


Figure 1.4 — Spectra of 2D microlasers, (a) - square [59] (DCM) and (b) - stadium [58]

One of the research objectives of this thesis is the fabrication of three-dimensional organic microlasers. This objective is based on the ideas discussed in the studies of 2D microlasers and extends the research of the thesis co-supervisor. 3D microlasers represent a new type of microlasers, so the study of their spectral properties and periodic orbits is immensely interesting. Presumably, the larger volume of the resonator would lead to the higher radiation power or to increased sensitivity of the microsensors.

1.3 Nanoparticles and nanocomposites

There exist a large number of working technologies for fabricating systems with nano-sized particles. All technologies can be classified by the type of nano-sized materials formation: dispersion technologies (top-down) based on the deaggregation of larger polymer particles towards nano-sized particles, and aggregation technologies (bottom-up) when nanoparticles are obtained by a chemical reaction or are grown (assembled) from single atoms. Synthesis methods can also be classified as chemical and physical, but there is no clear boundary. For instance, physical action in many technologies (such as solvothermal synthesis, spray pyrolysis and gas phase nanoparticles synthesis) is used for the chemical reaction initiation, and not directly for deaggregation of the substance. Thus these technologies are physico-chemical.

The «top-down» synthesis methods include mechanical milling, sonochemistry, removing one of the components of the heterogeneous system by chemical reaction or anodic dissolution, and various lithography techniques. The most common «bottom-up» technologies include sol-gel method, laser evaporation, electric arc evaporation, magnetron sputtering, hydrothermal synthesis, nanoreactor synthesis, chemical vapor deposition and others.

All technologies considered above have their own advantages and disadvantages. For instance, high-energy methods based on rapid condensation, rule out aggregation and growth of nanoparticles, and allow one to obtain nanocomposite materials with different microstructures. However, the nanoparticles are always randomly located on

the substrate. The nanoparticles obtained by mechanical milling are sufficiently polydisperse, but it is hard to obtain very small-sized particles.

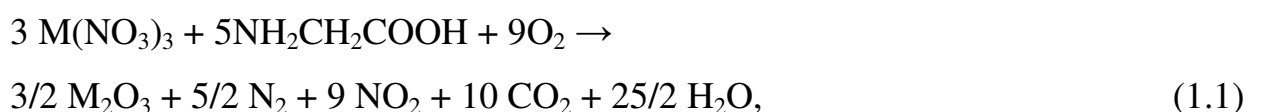
In this study, rare earth (Er and Yb) oxide nanoparticles are considered. Lanthanides are of interest because of their electronic configuration. The electronic structure of the lanthanide elements is either $[\text{Xe}] 4f^n 6s^2$ or $[\text{Xe}] 4f^{n-1} 5d^1 6s^2$ (here n is an integer number from 1 to 14) [63]. Lanthanum, the first element in a series, has no electrons in f -orbitals. With the increase in atomic number of the element, electrons fill the $4f$ subshell. Lutetium has fully filled f -orbital [64]. Since electrons are added to the internal $4f$ subshell while the outer electron shells remain intact, the lanthanides have similar chemical properties [64]. Moreover, since the valence electrons are well shielded by the $5s$ and $5p$ subshells, the spectral characteristics of the lanthanides remain practically unchanged when the environment into which the ion is implanted changes. Due to their structural-induced magnetic, spectroscopic and luminescent properties, the lanthanides are widely used in optoelectronics (development of laser and non-linear optical elements), solar cells [65, 66], fiber optic amplifiers [67], biological labeling [68], photodynamic therapy [69], etc.

A recent achievement in the telecommunications field is the introduction of the erbium-doped fiber amplifiers. The shift from regenerators to amplifiers allowed one to develop purely optical network. In 1990 the first erbium-doped fiber amplifiers (EDFA) were developed, and the possibility of their wide use in the extended communication lines became apparent [67]. One of the objectives required to develop the integrally built erbium-doped fiber amplifiers is the increase in the erbium concentration. The erbium concentration should be sufficient to ensure the operation of the amplifier in a waveguide section, which is no more than 10 mm long. The current required length is about 1 m. The first integrated optical amplifiers were based on the erbium-doped oxide films (Al_2O_3 , Y_2O_3 , SiO_2), polymers and silicon [70]. The largest gain per unit length, 4 dB/cm, was obtained for silicon doped with Er ions. The current challenge is to reduce the waveguide length to 1–10 mm. This would allow one to remove the coil and thus greatly reduce the size of the amplifier.

In order to solve the mentioned problems, planar waveguide amplifiers based on erbium-doped polymers or nanoparticles are actively studied in recent years. A significant (by several orders of magnitude) increase in the erbium concentration allows one to reduce the active waveguide length to several millimeters. In [71] the results of experimental study of planar optical waveguide based on PMMA polymer doped with erbium organic compound are provided.

In [72] the waveguide amplifier whose core material is nanocomposite based on Y₂O₃/Er nanoparticles in the PMMA matrix is considered. The interaction length of the amplifier made from nanocomposite material is about 5 mm, so that this amplifier can be used in integrated optics. The main present disadvantage of nanocomposite materials, which prevents their practical application, is the high light scattering. This requires research to develop optically transparent nanocomposites with no less than 10% optically active nanoparticles.

Various temperature methods are commonly used for the rare earth oxide nanoparticles synthesis, including thermal decomposition of rare earth salts and hydrates [73–78], physical vapour deposition (PVD) method [79], liquid phase deposition method [80], high energy milling [81], hydrolysis [82–83], sol-gel method [84], pyrolysis [85], etc. For instance, [86] considers decomposition of the rare earth salts in aqueous glycine solution and compares polymer, carbonate, oxalate precursors. The combustion method is also widely used [87]. Its general reaction equation can be expressed as follows:



where M = Y or Eu in this particular case.

Most of the abovementioned methods allow one to obtain rare earth oxide nanoparticles whose size exceeds 10 nm [88]. Moreover, these methods in whole or in part include high temperature synthesis stage (about 400–800°C). The typical consequence of the high temperature treatment is the aggregation of the nanoparticles. Figure 1.5 shows the images of nanoparticles obtained by high temperature synthesis.

Recent studies of the luminescent nanoparticles synthesis do not involve high temperature treatment. In [89–92] the synthesis of rare earth nanoparticles at low temperature and in anhydrous polyalcohol solutions is considered.

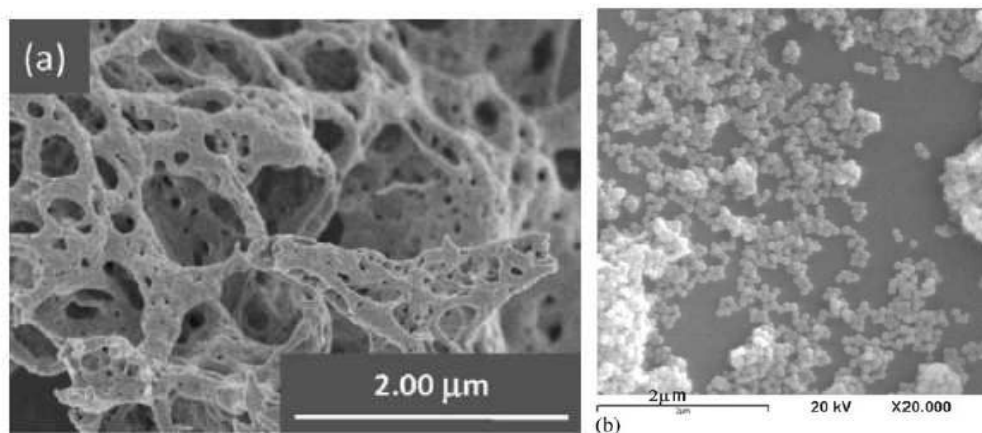


Figure 1.5 — SEM images of nanoparticles obtained by high temperature synthesis from a mixture of rare earth nitrates in glycine, (a) [85] and (b) [86]

In these kinds of syntheses, hydroxides are not formed, because the reaction takes place in an anhydrous medium. Instead, low-dimensional rare earth oxide nanoparticles are formed, so there is no need in subsequent high temperature treatment of reaction intermediates.

Chapter 1 conclusions

Chapter 1 surveys two recent trends in photonics: organic microlasers and luminescent nanoparticles synthesis. The design and materials for microlasers, the new microelements of integrated optics, are considered. The production technology, emission characteristics, and applications of microlasers are discussed. The importance and prospects of the studies of three-dimensional organic microlasers generating a fixed-wavelength grid conducted in this thesis are shown. Low temperature synthesis of luminescent nanocomposites and possibility of fabricating microlasers based on inorganic luminescent nanoparticles are considered.

CHAPTER 2. SELF-ORGANIZATION PROCESSES IN POLYMERS AND NANOCOMPOSITES

This chapter studies in detail self-organization processes in acrylate-based polymer composites and in nanocomposites based on ZnO nanoparticles. The question of composite structuring using nanoparticles is also considered.

2.1 Self-organization processes in polymers

Study of self-focusing of light began in my master's thesis. This was a continuation of a work in this area, previously undertaken at the Department of Photonics Engineering (ITMO University, St. Petersburg, Russia).

The underlying idea of the work is coupling of optical fibers by microlenses on their ends. Nitrogen laser (LGI-21, $\lambda=337\text{nm}$) radiation focused by a lens was introduced into one of the ends of a multimode optical fiber (total fiber diameter — $125\mu\text{m}$, core diameter — $50\mu\text{m}$). On the other end of the fiber, which was vertically fixed, a drop of monomer composition was placed. The size of the drop was visually controlled using a microscope. After the exposure by the nitrogen laser, the top of the fiber was washed in isopropyl alcohol to remove liquid monomer, and then dried. Exposure time varied from 3 seconds to 1 minute. A series of experiments were conducted to investigate the growth processes of elements on the top of the optical fiber, and to identify the corresponding regularities such as the dependence of element's form and radius of curvature on the exposure time, etc.

As a result, microlens elements were fabricated (see figure 2.1).

During the process, the dynamics of microelement formation was studied in detail. All monomers considered throughout this chapter have free-radical polymerization mechanism (the structure of monomer compositions is explicitly examined in paragraph 2.2).



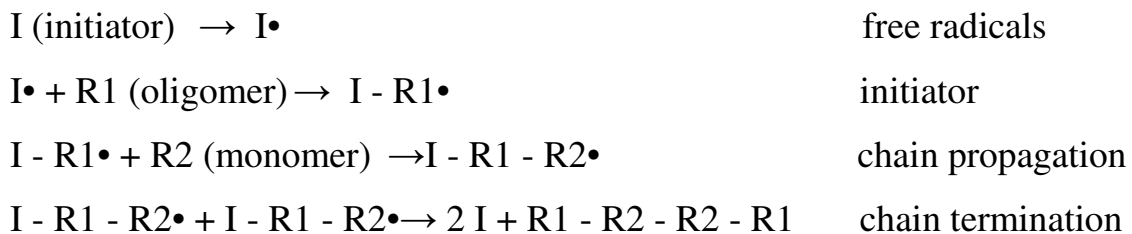
Figure 2.1 — Microlens elements obtained via polymerization on the top of the optical fiber. Images made by optical microscope, exposure for structure in the left is 5 seconds, in the right – 45 seconds

Polymerization is a process of high molecular weight material (polymer) formation, in which molecules of low molecular weight material (monomer, oligomer) add onto the active site of a growing polymer molecule. To initiate the chain polymerization, a certain number of free radicals or ions must be produced inside the monomer. This can be arranged using light, ionizing radiation or chemically active additives.

Photopolymerization is a process of polymer formation by light, mainly by ultraviolet radiation. In our case, UV curing is based on the radical chain reaction. Energy of UV radiation is too low for rapid breaking of the carbon-carbon double bond (C=C) and free radical production, so photoinitiators and photosensitizers are used. They are special materials that generate free radicals under the exposure.

The curing process can be shown in the following diagram:

UV



The photopolymerization mechanism and kinetics of the process are determined by several factors: the structure of the monomer composition, the type and concentration of the initiator, the presence of light-absorbing components.

Two questions are noteworthy: why is it even possible to obtain microstructures presented in figure 2.1, and why there is no broadening of the obtained elements. To answer this question, we consider the process of microelement formation step by step.

Polymerization does not begin immediately; it begins when the energy absorbed by the monomers reaches a certain threshold. The delay is due to the fact that first pulses burn the oxygen which is an inhibitor of the process [93], and generate free radicals from the initiator molecules. Most free radicals are produced in the area where intensity of the outgoing radiation is maximal (see figure 2.2).

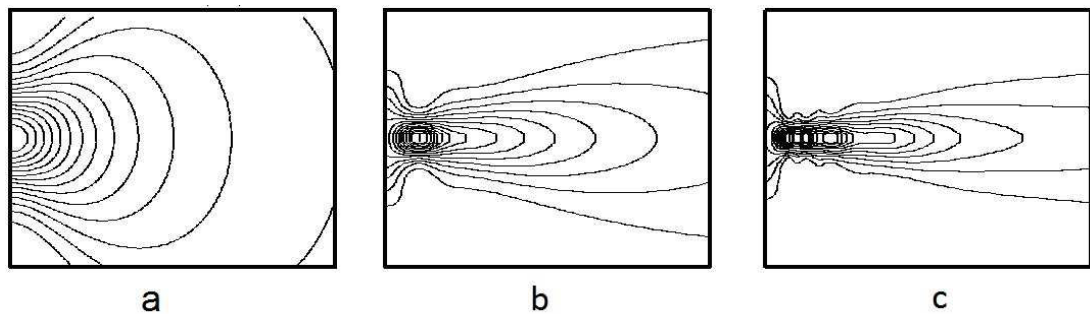


Figure 2.2 —Light intensity redistribution with the polymeric structure formation: a – initial stage, no redistribution is observed; b and c – polymer element formation followed by redistribution of outgoing light intensity

This is an incubation stage. After the energy threshold is reached, polymerization takes place continuously and is accompanied by a smooth change of refractive index. This change begins not after formation of polymer chains, but directly after bond breaking and free radical formation, (see figure 2.3) [94]. Refractive index increases due to the increase in the total number of bonds per unit volume and a more dense molecular packing.

At the next stage of formation, the element corresponding to the quasi-lens arises. Then the formation of cone-shaped element with rounded top begins, see figure 2.1 (left). With further increasing of exposure time, there is an alignment of the profile of the element, but the width of the element does not increase. This is due to self-written polymeric waveguide in monomeric mixture which is formed because of the difference in the refractive indices (1.48 for the monomer composition, and 1.52 for the polymer). Self-focusing effect is present from the beginning of polymerization, because the

refractive index of the monomeric mixture increases after free radical formation, as mentioned above.

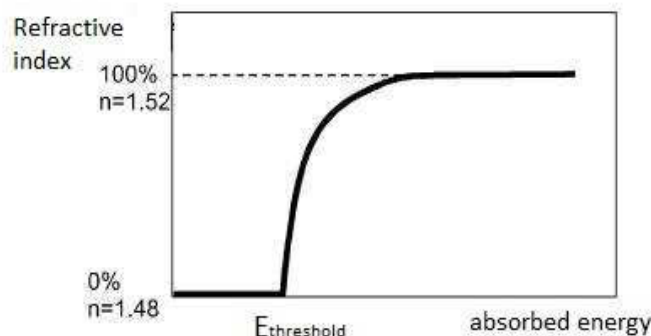


Figure 2.3 — Dependence of the refractive index of the composition on the absorbed energy

Figure 2.4 shows how the intensity distribution of the outgoing radiation changes along the time, when escaping from the top of the fiber. Initially (figure 2.4a) the intensity distribution is as usual: the divergence angle of the outgoing light is the same as the angle at which light was introduced into the waveguide. Maximum intensity occurs in the area located in the immediate vicinity of the top of the fiber. As a consequence, most free radicals are produced in this area, and polymerization process primarily begins here. As mentioned above, the refractive index of the polymer is higher than that of the surrounding liquid monomeric mixture. Thus self-focusing — redistribution of light intensity — occurs (figure 2.4b). Now the formed thin layer located near the area with maximum intensity of radiation serves as the top of the fiber. As the polymer chain grows, it becomes itself an extension of the optical waveguide core and has a constant diameter (figure 2.4c).

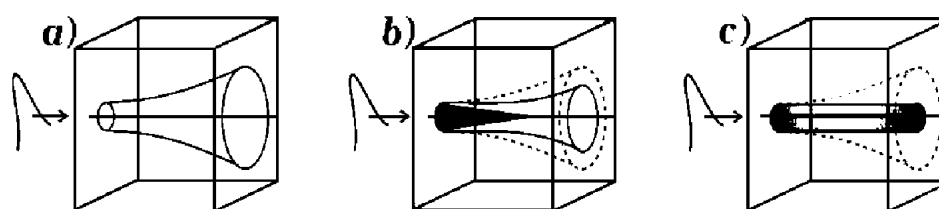


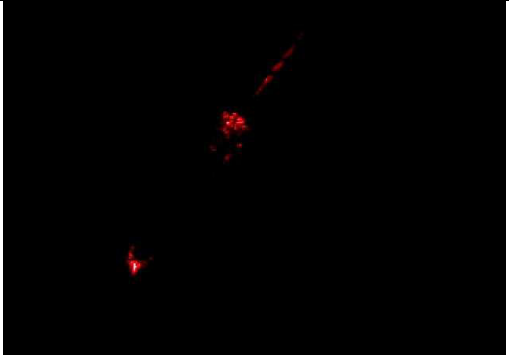
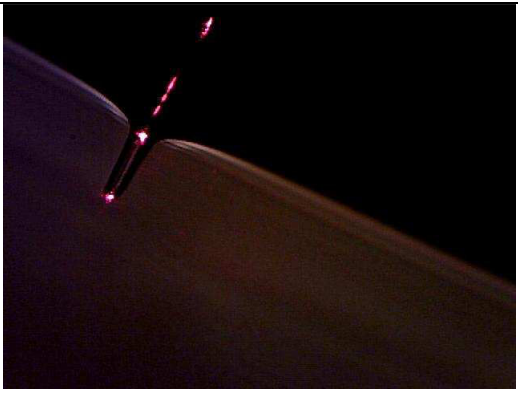
Figure 2.4 — Self-focusing of light in a medium with a varying refractive index

It is known that even totally internally reflected light comes out of the substance for one-half of a wavelength due to Goos–Hänchen shift. Hence a slow increase in

width of the element might be expected. However, there is no increase in width, because energy of the outgoing radiation is too low to burn the oxygen, initiate radicals and begin polymerization. Finally, after sufficient exposure, cylindrical-shaped elements with rounded top were fabricated, see figure 2.1 (right).

To confirm the waveguide structure of microelements, a series of experiments were conducted. Laser radiation was introduced into the fiber with the element on its top. Table 2.1 presents side view of the elements, left — without radiation, right — during the transmission of light.

Table 2.1 — Sideview of polymeric microelements with (right) and without (left) radiation laser beam introduced within the fiber.

Polymeric element	Polymeric element with introduced radiation
	
	

It is clearly seen that there are almost no losses in the cylindrical part of the element. This indicates that the formed element is indeed a waveguide. There is an excessive luminescence at the boundary of fiber and microelement. It can be explained by boundary reflection losses (refractive index of silica is 1.46, while that of polymer is

1.52) and by the fact that diameter of the microelement is smaller than diameter of the fiber core.



Figure 2.5 — Sideview of polymeric microelement, 220 μm length. Laser light introduced within the fiber. Radiation is observed only on the top of microelement

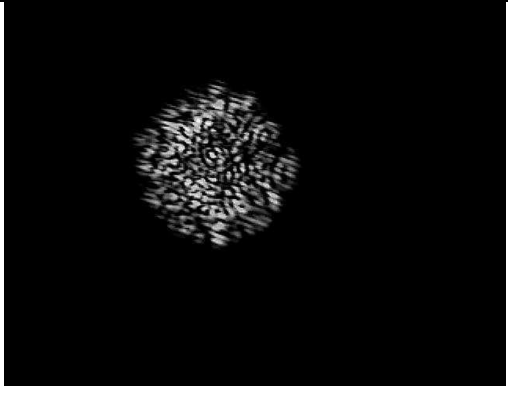
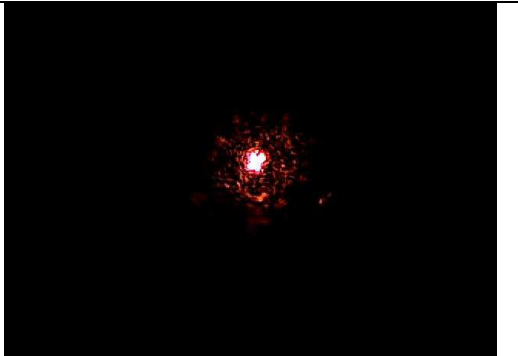
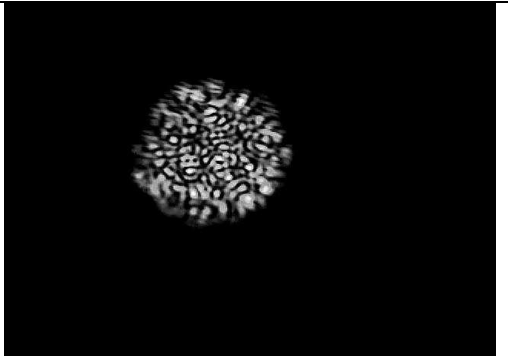
It was also proved that fabricated microstructures are indeed microlenses and are able to focus the radiation. One of the ends of the fiber was vertically fixed on a microscope stage. The laser diode radiation was introduced inside the fiber through the second fiber's end. One microscope eyepiece was replaced by a webcam connected to the laptop. This allowed us to move the webcam with the desirable pitch and observe the outgoing radiation from the fiber in real time at different distances from the top. The experiment consisted of two stages. First, the fiber without polymeric microelement was examined. After focusing on the surface of its top, webcam recorded the distribution of the light field (10 μm pitch). Second, the same procedure was applied to the fiber with microelement on the top. Initial focusing was on the vertex of the microelement. Further processing and data analysis using special software allowed us to estimate the spatial distribution of luminosity (radiation intensity).

Table 2.2 shows an example of measurement results for the sample shown on figure 2.5. Table 2.3 provides their comparative analysis. A series of photos clearly show that a redistribution of the light field occurs in the microelement — the outgoing radiation has higher luminosity than in the case of fiber without microelement. As the distance from the element increases, the defocusing of the laser beam is observed. It follows that

polymeric microelement is a microlens (mode converter), which can significantly reduce losses when radiation from a multimode fiber is introduced into a single-mode fiber.

Data from table 2.3 allow us to qualitatively estimate the efficiency of microelement focusing. Images from the table 2.2 were analyzed using ImajeJ program, which allows to evaluate spatial distribution of brightness (in our case, the intensity of light). Data show that the luminosity of the radiation outgoing from the microelement indeed exceeds that from the ordinary fiber. Defocusing of the radiation is fast enough; the focal length of element is rather small and lies in the range 0-10 μm from the top of the polymeric microelement. However to use the microelement for coupling fiber is still efficient even with 40 μm distance between the element and the top of another fiber.

Table 2.2 — The intensity distribution of the radiation field outgoing from the fiber with and without the microelement at different distances from the top of the element (pitch is 10 microns)

Pitch, μm	With element on the top	Without element on the top
0		
10		

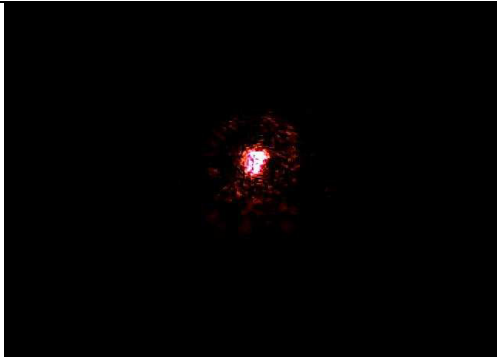
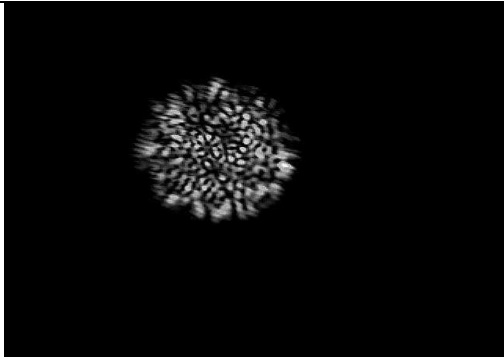
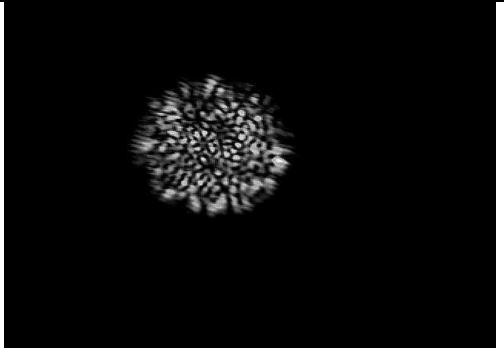
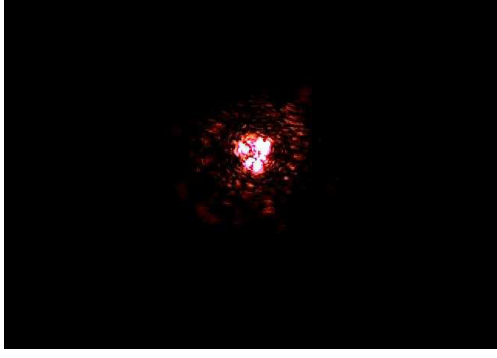
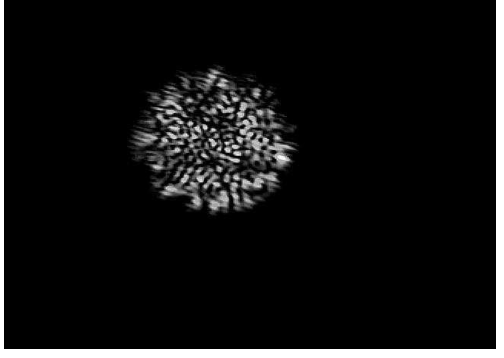
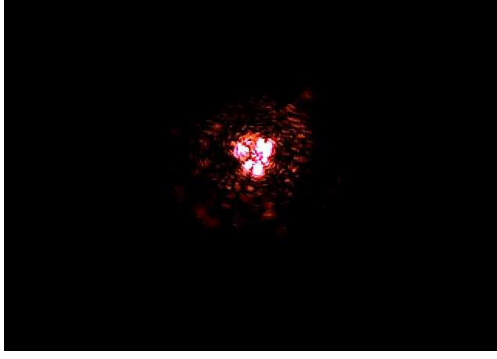
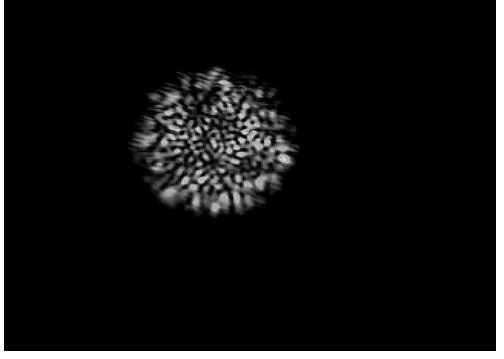
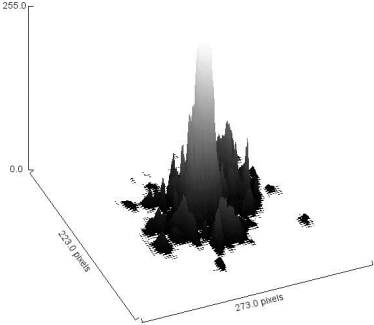
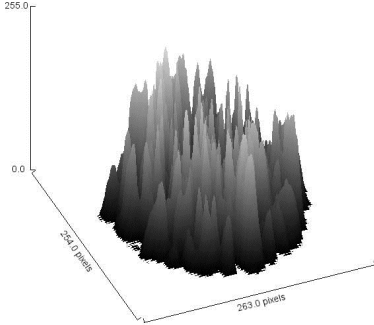
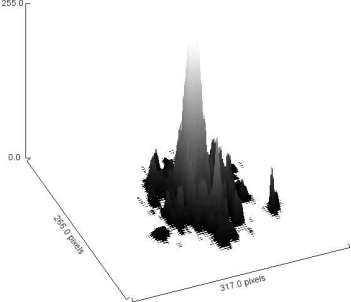
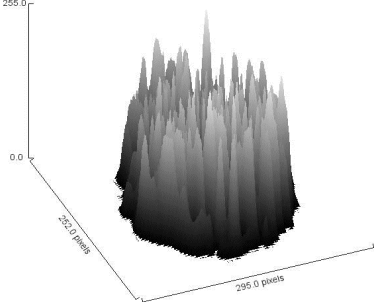
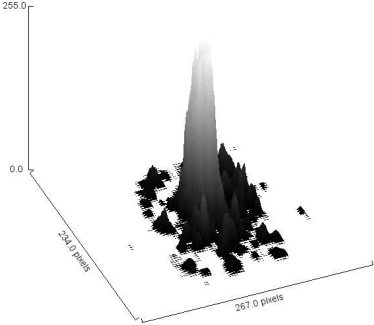
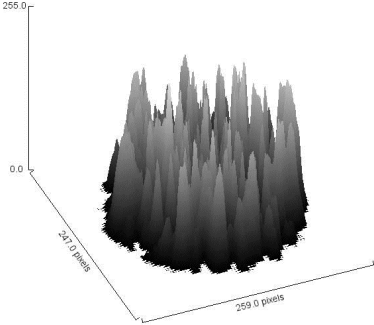
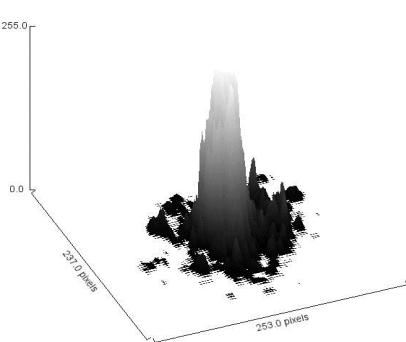
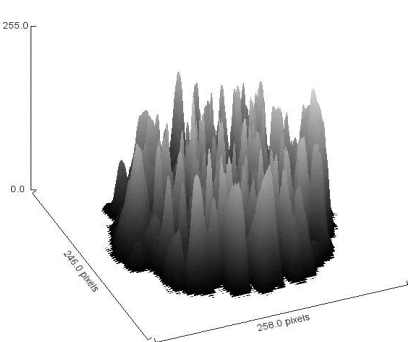
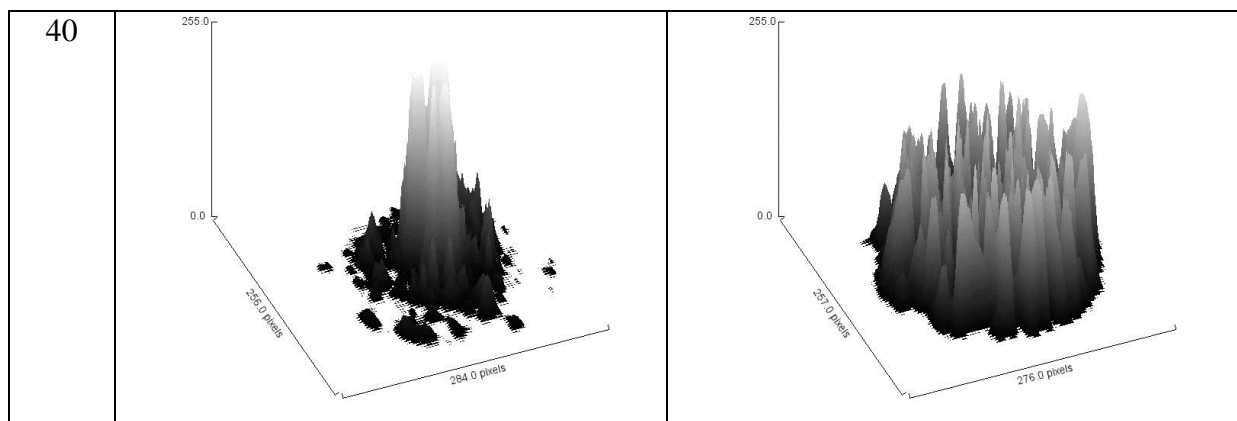
20		
30		
40		
50		

Table 2.3 — Comparison of the radiation intensities outgoing from the fiber with and without the microelement at different distances from the top of the element (pitch is 10 microns)

Pitch, μm	With element	Without element
0		
10		
20		
30		



2.2 Self-organization processes in nanocomposites

Next stage in the study of self-organization processes is the study of nanocomposites instead of a pure monomer. The effect of light-induced transfer of nanoparticles in the nanocomposite was first described in 2005 in [95]. The effect is present when polymer nanocomposites are periodically exposed, for instance by interference pattern from two laser beams. In [95] the diffusion of inorganic nanoparticles in an organic polymer matrix to the unexposed areas of the monomer was observed.

Difference between refractive indices of organic photopolymers is not sufficient, that is not the case of different inorganic nanoparticles. Hence the use of such organic-inorganic systems allows one to create substances with a much greater difference in refractive indices Δn .

Explanation of nanoparticles redistribution effect was suggested in [96]. A spatially heterogeneous radiation initiates the production of free radicals in the exposed areas of the monomers. These free radicals react with the monomers. Polymerization lowers the chemical potential of the monomers in the exposed areas, and leads to diffusion (transfer over short distances) of monomers from unexposed areas of the composite to exposed areas. On the other hand, inorganic nanoparticles diffuse also to unexposed areas (figure 2.6), because they are not involved in the polymerization process, and their chemical potential in exposed areas increases while the monomers expend.

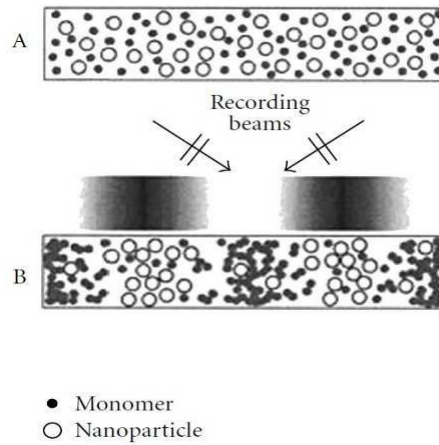


Figure 2.6 — Movement of nanoparticles in the composite which is exposed with a periodical intensity [95]: A - before exposure, B - after exposure and diffusion

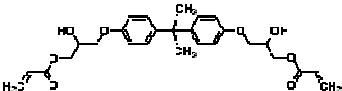
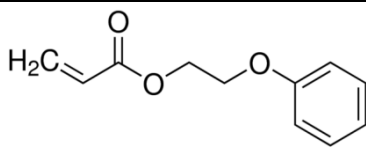
This interdiffusion process continues while polymerization takes place, until the high viscosity of the exposed material leads to their immobility of the polymer molecules and nanoparticles. As a result, due to the redistribution of nanoparticles, we notice the formation of a periodic structure with refractive index difference between the exposed and unexposed regions.

2.2.1 Materials

Table 2.4 describes the materials that were used in the study (for a more detailed information on all the used materials, see Annex A).

Table 2.4 — Characteristic of monomers used in the study

№	Name	Structural formula	Function
1	2-carboxyethyl acrylate (2-Car)	$\text{H}_2\text{C}=\text{CH}-\overset{\text{O}}{\parallel}{\text{C}}-\text{OCH}_2\text{CH}_2-\overset{\text{O}}{\parallel}{\text{C}}-\text{OH}$	Surfactant acrylate

2	Bisphenol A glycerolate (Bis A)		Acrylic Monomer
3	2-Phenoxyethyl acrylate (PEA)		Linear acrylate
4	ZnO		Zinc oxide nanoparticles, 20nm diameter
5	2,2-dimethoxy-2-phenyl-acetophenone (In II)		Photoinitiator of polymerization, The maximum absorbance is in UV spectrum

The required component in the used composites is 2-carboxyethyl acrylate (2-Car). Due to the presence of the carboxyl group, this monomer is able to react with the surface of quartz or glass. This increases the adhesion to the substrate material, and provides directional growth of microstructures from the substrate.

2-Car is also able to interact with the surfaces of the nanoparticles, creating around them the organic membrane and preventing their aggregation in the composite. Bisphenol A ensures the lateral binding of the monomers and increases the strength of the microstructures. 2-Phenoxyethyl acrylate can be used to reduce the viscosity of the monomer mixture and to modify the refractive index.

As was explained in paragraph 2.1, the photoinitiator of polymerization, the source of free radicals, is the essential component of the polymer composite. In our case 2,2-dimethoxy-2-phenyl-acetophenone was used as the initiator. Its structural formula and absorption spectrum are shown in figure 2.7. Mass concentration of the initiator was 0.02%.

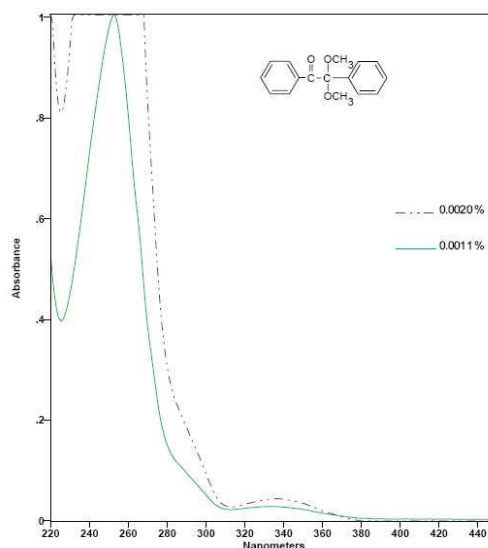


Figure 2.7 — 2,2-Dimethoxy-2-phenyl-acetophenone: structural formula and absorption spectrum depending on its weight concentration

It is worth mentioning that photoinitiator absorption maximum is shifted relative to the laser operating wavelength. This slows the polymerization process and allows the light to propagate deep into the composite volume.

2.2.2 Fabrication of polymer composites and nanocomposites

In this study a three-component acrylate composite was used. The composite consisted of BisA/2-Car/PEA in 25:55:20 mass percentage.

Fabrication technology of the monomer composite is as follows.

1. For 2 hours the monomers are preheated to reduce their viscosity, until they reach a temperature of 65°C;
2. 2-Car is placed in a thermostat at 100°C. Small portions of Bis A (which has a greater viscosity) are introduced in a thermostat with constant stirring;
3. After the solution is homogenized, it is restrained for another 1 hour at 100°C;
4. PEA is injected into the monomer mixture, the solution is stirred and heated;
5. Photoinitiator is introduced into the prepared monomer mixture;
6. For 24 hours the solution is incubated at 35°C.

The nanocomposite under investigation was fabricated using the same monomer matrix as described above. ZnO nanoparticles are preannealed at 300°C for an hour.

After steps 1–3 from the above list are accomplished, and the mixture of 2-Car and Bis A is homogenized, ZnO nanoparticles are gradually introduced. The solution is constantly stirred and incubated at 100°C until particles are completely dissolved. Then steps 4–6 from the above list are accomplished.

2.2.3 Movement of nanoparticles during the holographic recording

To study the photoinduced transfer of nanoparticles, a holographic recording was used. Composites were deposited on a glass substrate precleaned with an alkaline solution (NaOH). The monomer layer was enclosed into a lamsan film to prevent the access of oxygen from the air, because oxygen inhibits polymerization process. The thickness of the monomer film was adjusted by spacers.

Recording of the microstructures was implemented using a two-beam interference scheme. The 325nm wavelength Helium–Cadmium (He–Cd) laser source of coherent radiation was used. The angle between the two interfering beams was 10°, so the period of the structure was 2 μ m. During the polymerization, the interference pattern is transferred into the polymer. Post-exposure treatment involves an uniform exposure of the sample to finish the polymerization of unexposed areas.

Figure 2.8 shows the cross-section of the microstructure under investigation obtained by optical microscopy and confocal microscopy.

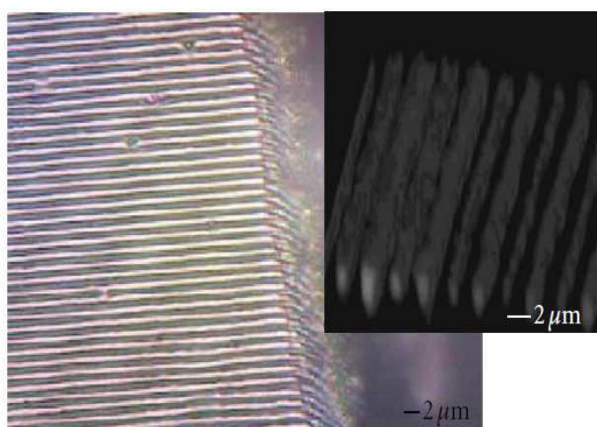


Figure 2.8 — Images of the microstructure under investigation: optical microscopy (in the left) and confocal microscopy (in the right, the sample is rotated by 90 degrees). Structure period is 2 μ m

We observe a regular structure consisting of periodically alternating bands of polymerized material (with a period of $2\mu\text{m}$) with nanoparticles and without them. These results prove that when nanocomposites are periodically exposed, the process, which was described above, occurs (figure 2.6). Nanoparticles move to unexposed areas, so the formation of three-dimensional structure increases.

Figure 2.9 shows the three-dimensional structure obtained by ion etching of another sample fabricated by holographic recording. The ion beam easily evaporates areas without nanoparticles in the polymer, but does not affect areas «intensified» with nanoparticles. Hence the spatial distribution of the nanoparticles becomes visible. Ion etching forms three-dimensional periodic subwavelength structure with high aspect ratio.

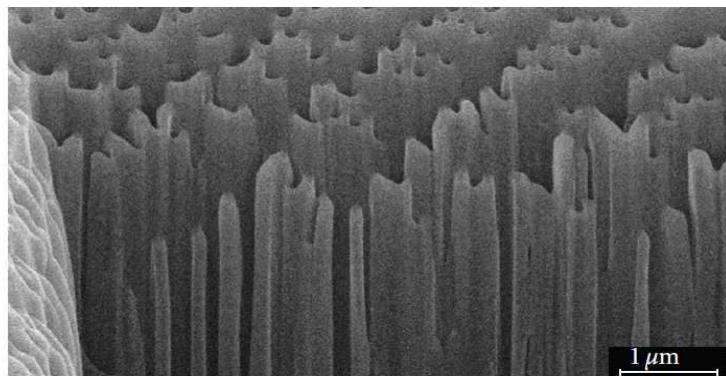


Figure 2.9 — SEM image of an ion-etched structure fabricated by holographic recording (period is $2\mu\text{m}$). The height of the vertical elements is $100\mu\text{m}$

2.2.4 Fabrication of subwavelength structures by projection lithography

Self-writing and self-focusing effects discussed above are applicable for diminishing polymerized area initially corresponding to light distribution in objective spot as well as to overcome geometric distribution of the light in focus. The main effect is light self-focusing that can be reinforced by oxygen inhibition and nanoparticles redistribution at photopolymerization. Figure 2.10 illustrates a short scheme of the projection lithography system. Recordings of the microstructures were obtained using a LUMAM–I3 fluorescence microscope (LOMO, Russia). A 355nm wavelength laser was used. The

width and intensity of the laser beam was adjusted by a system of lenses and optical filters. A sample with the monomer composition (without nanoparticles) was located on the microscope stage. The laser beam was focused on the sample surface with a lens (figure 2.10, left). A mask with a prepared image was placed before the lens.

The mask is a relief polymer film with the contour obtained by laser ablation using the engraver. Initially this is a lavsan film with a thermosensitive layer based on polybutylmethacrylate (PBMA) with smoke-black particles that absorb laser radiation. The template of the desired mask is created using graphic editors (Corel Draw, Canvas) and is transferred to the lavsan film by a laser beam which evaporates PBMA in the required areas. The thickness of the evaporated (removed) layer is 10–13 μm . The mask was made by Vera Balya using the LaserGraver LG2500 SP47 ($\lambda = 1.06\mu\text{m}$, pitch 2.5 μm , focal spot diameter 2.5 μm).

Figure 2.10 (right) shows the mask which is used in the experiments describe in this section, for the fabrication of polymeric micro- and subwavelength structures. There are four circles with diameters of 10 μm , 20 μm , 40 μm , and 60 μm . Due to the 10-fold lens, they form light spots with diameters of 1 μm , 2 μm , 4 μm , and 6 μm respectively.

Samples were fabricated as described in subparagraph 2.2.2. Two series of samples were fabricated: polymer composite made up of BisA/2-Car/PEA (25:55:20) and nanocomposite with the same matrix doped with 10% ZnO nanoparticles. The exposure was chosen depending on the thickness of the samples. After the process, the unpolymerized areas were washed away by isopropyl alcohol.

The results differ for compounds with and without nanoparticles. In the case of non-doped polymer matrix, some of the desired structures were fabricated, but not all of them. All cylindrical elements have diameters no less than 3 μm (measurements were performed by optical microscope). The element with the smallest diameter (light spot size 1 μm) was not obtained in any of the experiments. Figure 2.11 shows the fabricated elements.

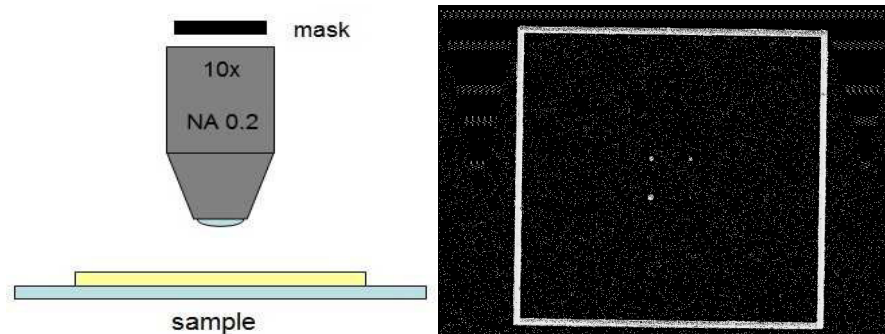


Figure 2.10 — In the left - scheme of the setup to record subwavelength microstructures. In the right – sample of the used polymer masks; this mask has four circles with 10µm, 20µm, 40µm and 60µm diameter

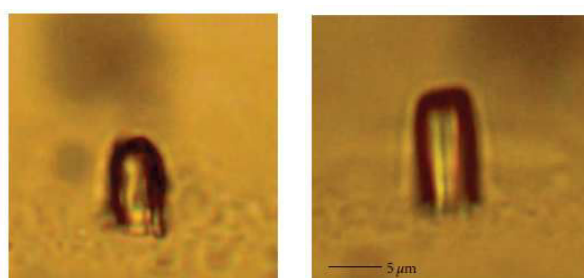


Figure 2.11 — Microstructures fabricated from pure polymer composite. Left: cylindrical microelement with a diameter of 4µm (light spot size 4µm). Right: cylindrical microelement with the diameter of 6.5µm (light spot size 6µm)

When a nanocomposite was used, cylindrical microelements were fabricated for all four light spots. It should be noted that these elements have less widening (deviation from the expected diameter was about 0.2µm). Moreover, it is possible to fabricate subwavelength microelements due to the self-organization of nanoparticles. Figure 2.12 shows microelements with diameters less than 1µm, fabricated in the nanocomposite compound (light spot size 1µm).

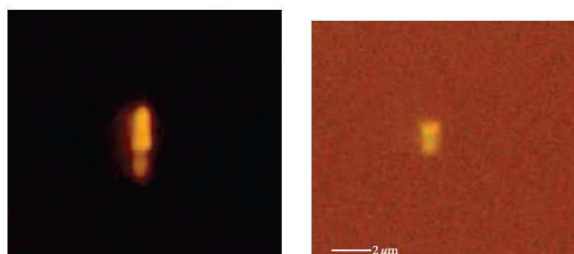


Figure 2.12— Cylindrical nanostructures fabricated by projection lithography in the nanocomposite. The height of the structures is 2µm. Diameters of the structures: 0.7µm (left), 0.6µm (right)

Chapter 2 conclusions

Self-organization processes in polymer composites and nanocomposites were studied.

1. The dynamics of the growth processes of self-organized polymeric microelement on the top of the optical fiber were investigated. Performed research shows that formation of the self-organized elements can be described as a superposition of processes occurring during photopolymerization, including self-focusing of light in a medium with a positive change of the refractive index and inhibiting effect of oxygen on the photopolymerization. It was proved that this element is able to focus the light, and its focal length was estimated.

2. Light-induced transfer of inorganic nanoparticles when the nanocomposite is exposed by periodic wave of light was investigated. It was shown that due to this phenomena using nanocomposite instead an undoped polymer composite increases the resolution of the lithography process.

Chapter 3. FABRICATION OF THREE-DIMENSIONAL ORGANIC MICROLASERS

In the Chapter 1, three-dimensional microlasers were considered just a little. This chapter deals with all steps of the fabrication of 3D microcavities. The methods used in the group to obtain flat, two dimensional structures, for example electron beam etching, does not work in the case of 3D. So, it was necessary to find new ways of fabrication. Three different technologies were investigated: projection lithography, deep ultra-violet (UV) lithography and direct laser writing by two-photon polymerization (2PP).

3.1. Projection lithography

The first experiments were performed on the set-up in St. Petersburg described in the section 2.3. The methods of the mask creation and the sample preparation were the same (See sec. 2.3). In this case, the composition of the polymer matrix was the following: 2-Carboxyethyl acrylate and Bisphenol A glycerolate (see annex A) in the mass ratio 7:3. As the laser dye the DCM was used in the concentration 0,5% wt. Dye was introduced in the monomer composition by stirring and heating. The mask contained series of squares with a side length of 400 microns. The lens magnification factor was 4. So, eventually it was expected to obtain the cuboids with the size length 100 μ m. Images of a cube obtained by this technique are presented on the Fig. 3.1. The mask was obtained by ablation of a polymer film by laser graver machine LG2500 SP47. Due to this fact the quality of the mask elements was not very high. So the bad quality of the structure can be explained by significant diffraction on the defects of the polymer mask. No lasing was observed during characterization with set-up in Cachan.

Other experiments were performed by George Taverne during his master's work. He used the same monomer composition with a dye, but used contact lithography. In this case the mask obtained by the same way was pasted to the thin glass and this glass was deposited directly on the monomer layer. In this method no optical system was used and the mask has the scale 1:1. The quality of the surfaces was not the best one, but these

microcavities showed multimode lasing. So, they were the first 3D microlasers which were investigated.

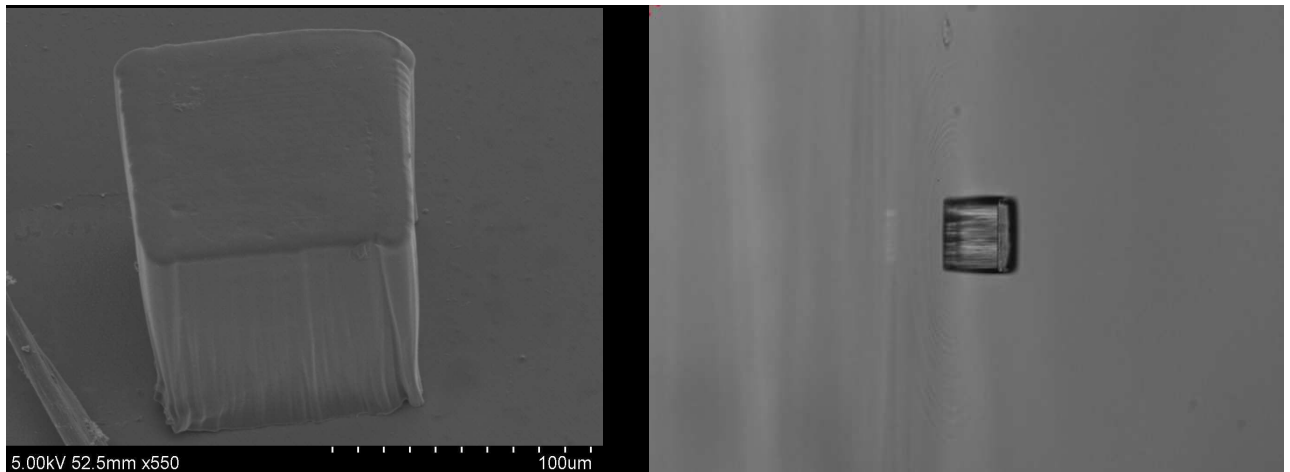


Figure 3.1 — Images of cuboid structures obtained by projection lithography made by scanning electron microscopy (on the left) and optical microscopy (on the right).

3.2. UV-lithography

The second and the main technology considered in this work as a way for obtaining tree-dimensional microlasers is the UV-lithography. The main difference from other types of photolithography is that the exposure is performed with ultraviolet or visible radiation, whereas other types of lithography consider X-rays, electron or ion flow, deep ultraviolet, etc.

UV-lithography is widely used in microelectronics. This technological method allows obtaining a certain pattern on the surface of a substrate. It is one of the main methods of planar technology used in the manufacture of semiconductor devices. In the standard lithography process, the photoresist is deposited on the surface of the substrate, and then exposed to light through a photomask with a predetermined pattern. During the next step, the exposed/unexposed areas of the photoresist are removed by a solution called developer. The resulting pattern is then used for further process steps of planar technology as etching, vacuum deposition, sandblasting, etc. After one of these processes, photoresist residues are removed. In this work, the resist is used not as an intermediate material to transfer a pattern to another substrate, but as a material to directly obtain the microstructures.

3.2.1 Materials: polymers and dyes

For the widely investigated two-dimensional microcavities, the typical polymer matrix is polymethylmethacrylate (PMMA) spin-coated from different solvents (anisole, dioxane, dichloroethane, etc.) [97]. In this work, it was appropriate to use another polymer matrix, the SU8 photoresist, which is well known and commercially available. Actually it was demonstrated that it leads to thick microstructures with high aspect ratio [98].

The SU-8 photoresist is a negative epoxy-based resist initially developed by IBM [99] which was created for the fabrication of micro-components for micro-electrical mechanical systems (MEMS). Due to its properties - high sensitivity, high resolution, low optical absorption, high thermal stability and good chemical resistance - SU-8 is widely used for various applications, such as structures or supports for microstructures and basic material for molding or packaging [100]. Its rather good adhesion properties allow using SU-8 with various substrates which is also important for fabrication of integrated circuits.

The SU-8 resist is obtained by dissolving the EPON resin into the organic solvent GBL (Gamma-butyrolactone). EPON - is a multifunctional epoxy resin having a high branched polymer structure. It consists of a bisphenol A novolac glycidyl ether. Fig. 3.2 shows a typical structure of the molecule EPON SU-8. On average, one molecule contains eight epoxy groups what is reflected in the title of the resist. The quantity of the solvent determines the viscosity and hence the possible thickness range of the layer.

Triaryl sulfonium salt is added (10%wt of EPON SU-8) and mixed within the resin as a photoinitiator.

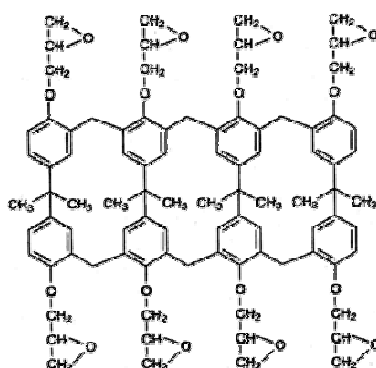


Figure 3.2 — Structure of the SU-8 EPON molecule

The key property that makes SU-8 very popular and suitable for ultra-thick resist applications is its very low optical absorption in the visible range. On the figure 3.3 the absorption spectrum of the SU-8 film with a thickness 25 μm is represented.

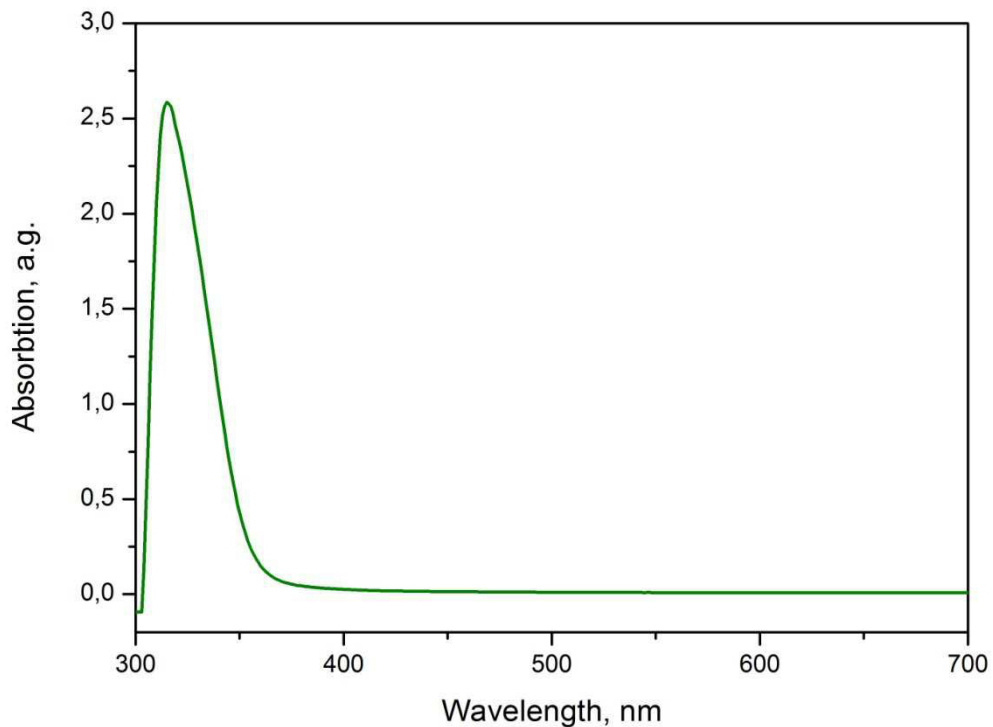


Figure 3.3 — The absorption spectrum of the SU8 2025 film (thickness about 25 microns)

This total optical transparency in the visible range guarantees a good adjustment in the case of multilayer lithography process. The maximum of the absorption is specifically shifted relative to the working wavelength (365nm). The low absorption on the polymerizing wavelength provides a uniform exposure over the entire resist volume/thickness, which gives rise to vertical sidewall profiles [101].

The polymerization mechanism of the SU-8 resist is not identical to the radical mechanism considered in the Section 2.1. The photoinitiator absorbs a photon and forms acid molecule H^+A^- , as indicated in Figure 3.4. This acid is formed only in areas directly irradiated by UV rays and plays the role of a catalyst for the polymerization taking place during the subsequent heating, called Post Exposure Bake (PEB). The PEB temperature should be higher than the glass-transition temperature (T_g) of the solid film, because at temperatures below the T_g the molecular motion is quite slow and molecules do not enter into any reaction [102].

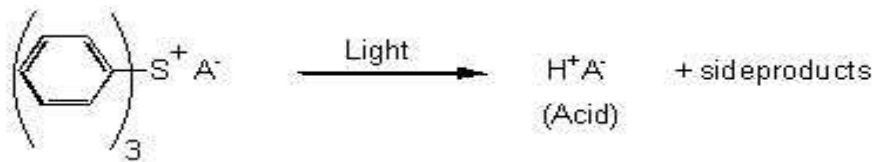


Figure 3.4 — Photochemical reaction of the photoinitiator transformation

During the post exposure heating process, the acid breaks bonds within the epoxy groups starting the reaction of polymer chains formation (Fig. 3.5).

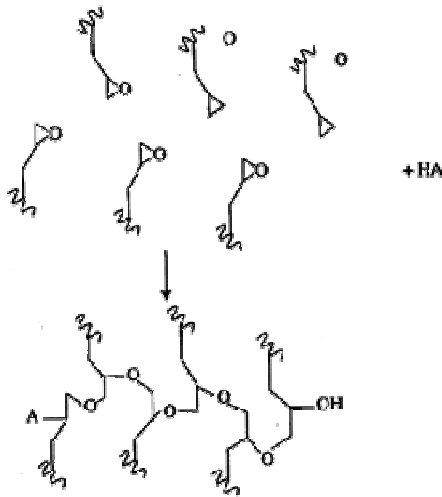


Figure 3.5 — Reaction of the polymer chains formation

This mechanism is similar to the mechanism of cationic polymerization. This process leads to the formation of a dense structure, insoluble in the organic solvent - propylene glycol methyl ether acetate (PGMEA). The material which was protected by the mask and then not exposed is dissolved in the solvent.

Using organic dyes as an active medium for lasing was considered in the section 1.1. In this experimental work, two organic laser dyes were used – Pyrromethene 597 (hereinafter PM 597) and Rhodamine 640 perchlorate (hereinafter Rhod 640). Their chemical structural formulas and absorption spectra in a solid SU8 polymer film is presented on the fig. 3.6 and 3.7 respectively. At the first stages of the experiment Pyrromethene 605 and DCM also were used.

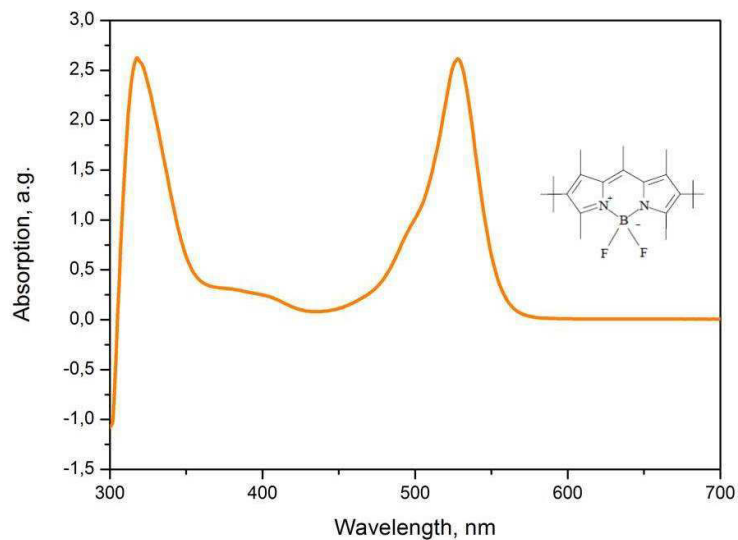


Figure 3.6 — Chemical formula of Pyromethene 597 and its absorption spectrum in the solid SU8 film (thickness 25 μm)

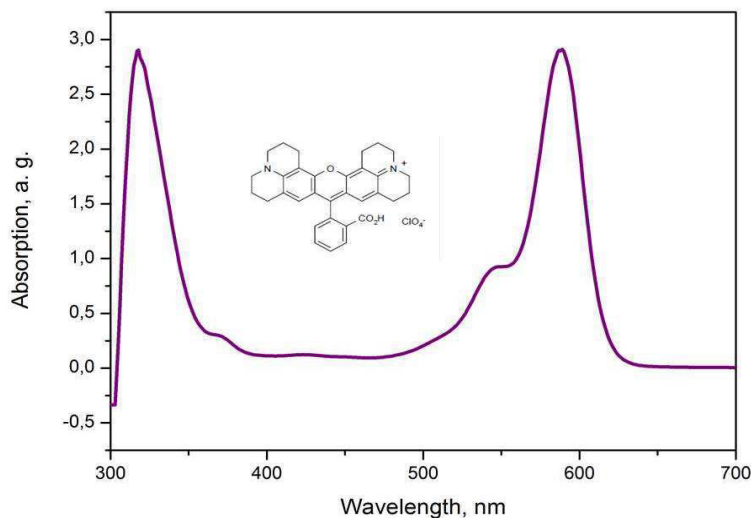


Figure 3.7— Chemical formula of Rhodamine 597 and its absorption spectrum in the solid SU8 film (thickness 25 μm)

3.2.2 Structures fabrication

UV-lithography fabrication of thick structures from the SU8 is widely used method based on the commercially available setups and the materials. But basically it is used for obtaining structured of different shapes from pure, undoped resist.

At first, we tried to fabricate the microcavities by a standard method from pure SU8 and then tried to introduce the dyes inside the cavity using the dye diffusion from the solution. Wafers with cubes (linear size 150 μm and height 54 μm) were obtained by

a standard UV-lithography technology and glass wafers covered by film from undoped SU-8 were obtained by directly UV-irradiation. DCM dye solutions with a concentration 0,5% wt were prepared in different solvents, namely: acetonitrile, tetrahydrofuran and isopropanol. The films were placed in the three solutions. After 2 hours, the films acquired a bright orange color, but they were deformed due to a significant solvent absorption and also were torn from the substrate. Using omnicoat, which is a special cover increasing adhesion between resist and substrate, didn't solve the problem. Cuboid structures were also placed in the solutions. In the case of acetonitrile or tetrahydrofuran the solvent was too aggressive, i.e. diffusion rate was significant smaller than speed of structure dissolution rate. In the case of isopropanol, no significant diffusion was observed.

This diffusion method looked not very effective, so it was decided to introduce the dyes directly into the non-polymerized resist before the lithography process. This is the main difference relative to a standard method, which requires the modification of the usual technology.

MicroChem presents a line of SU8 resists with varying viscosities, allows to obtain structures with a thickness of the order of a micron to several hundred microns. On the figure 3.8 the dependences of the film thicknesses on the viscosity of the resist and the spin-coating mode are represented [103]. The resist should be viscous enough to obtain a thick film and liquid enough to dissolve the amount of dye necessary for lasing. Due to these requirements, the SU-8 2025 (concentration of the pure polymer in resist is 0.6855% wt) with a viscosity 4500 cSt was chosen. It should be noted that this datasheets by MicroChem doesn't contain any special data about thickness dependence due to the type of the wafer etc.

The laser dyes were introduced directly into the resist using ultrasonic and magnetic stirring. The dye concentration was 0.5 %wt relative to the weight of the polymer in the photoresist. Significant increasing of the concentration was not successful, since the solubility limit is about 1%. For example, the dye concentration for 2D microlasers investigated before [62, 97] was 5% wt in PMMA. And this restriction was due to the quenching, not due to the limit of solubility.

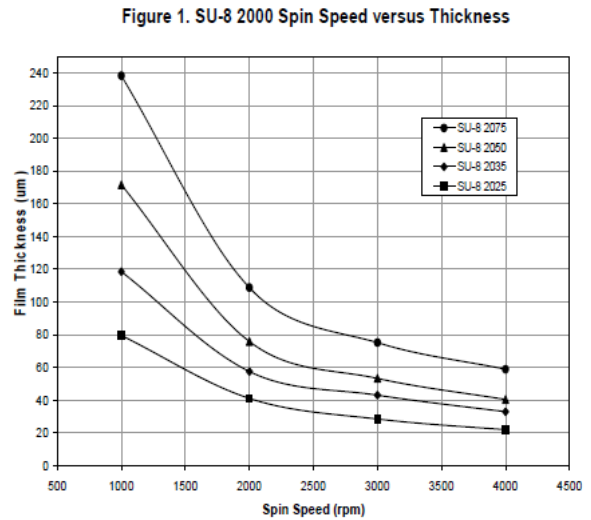
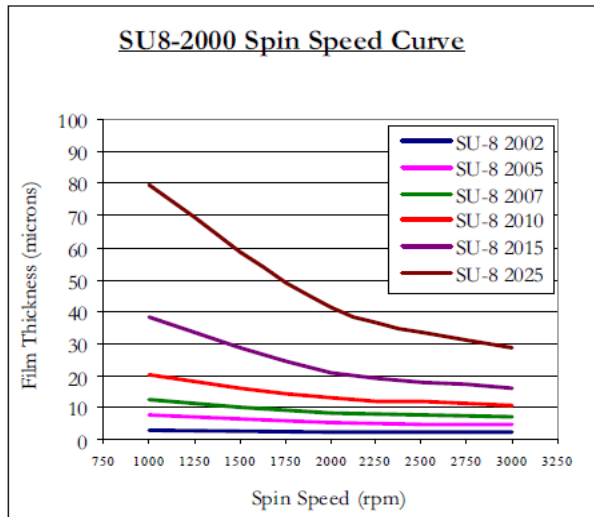


Figure 3.8 — Dependence of the film thickness on the spin speed for the SU-8 resist 2002 – 2075

At first, the solution was treated in an ultrasonic bath for 30-40 minutes. It was controlled that the temperature of solution did not exceed the T_g for the SU-8 which is about 55°C [104]. This was done to prevent any chemical interactions inside the resist, which may take place at a temperature above T_g . Then the warm solution was stirred until it gets to the room temperature. Repetition of 7-10 cycles (as a cycle we mean on iteration of ultrasonic (40min) and subsequent stirring) provides a homogeneous solution. The technology of the dye introduction does not depend on the specific laser dye.

This lithography fabrication process was completely performed in the clean room of Institut d'Alembert in the ENS de Cachan with the help of the engineer responsible of the clean room, Joseph Lautru.

SU-8 2000 series photoresists are most commonly exposed with conventional UV (350-400 nm) radiation, although i-line (365 nm) is the recommended wavelength. Also they can be exposed with e-beam or x-ray radiation. Process can involve different steps: substrate pretreat, coat, edge bead removal, soft bake, exposure, post exposure bake, develop, rinse and dry, hard bake/removal. The fabrication process presented in this work consists of the following steps: spin coat, soft bake, expose, post-exposure bake, followed by development (full list of the possible steps is represented on the fig. 3.9). A

controlled hard bake is recommended to further cross-link of the SU8 if the resist is used as part of the device.

Short description of the fabrication technology used in this work is presented below. The full description is contained in the annex B.

Due to the rather high refractive index which is 1.6 for the undoped polymer (comparing, for example, with the PMMA, which is 1.49) and a good adhesion, SU-8 can be successfully used with different substrates. In this work, experiments were performed on two different substrates: silicon wafer covered by 2 μ m silica layer (bought from Process Specialties) and glass slides (1mm thickness, cleanroom cleaned, supplied by Schott Nexterion). Also it is possible to use non pre-cleaned glass wafers. In this case wafers were cleaned by acetone, which was fully washed away by isopropanol. Both types of wafers were cleaned by compressed nitrogen directly before resist deposition. The scheme of our lithography process is presented on the Fig. 3.9. The solution was deposited on the wafer by spin-coating. The spin-coating speed mode consists of two parts: slow rotation for the uniform distribution of the resist on the substrate and the fast rotation, whose speed is determined by the targeted thickness (Fig. 3.9 (a)). The most used mode included rotation on the speed 500 RPM during 5 seconds and the fast rotation on the speed 2000 RPM during 45-60 seconds. In this case the film thickness is about 25 microns.

After the film deposition, the soft bake procedure follows. After coating, the photoresist still contains too much solvent. The soft bake procedure has several purposes: to reduce the residual solvent and resist free volume, to anneal out the residual stresses and to improve adhesion, to stabilize the film and to reduce the stickiness of the surface.

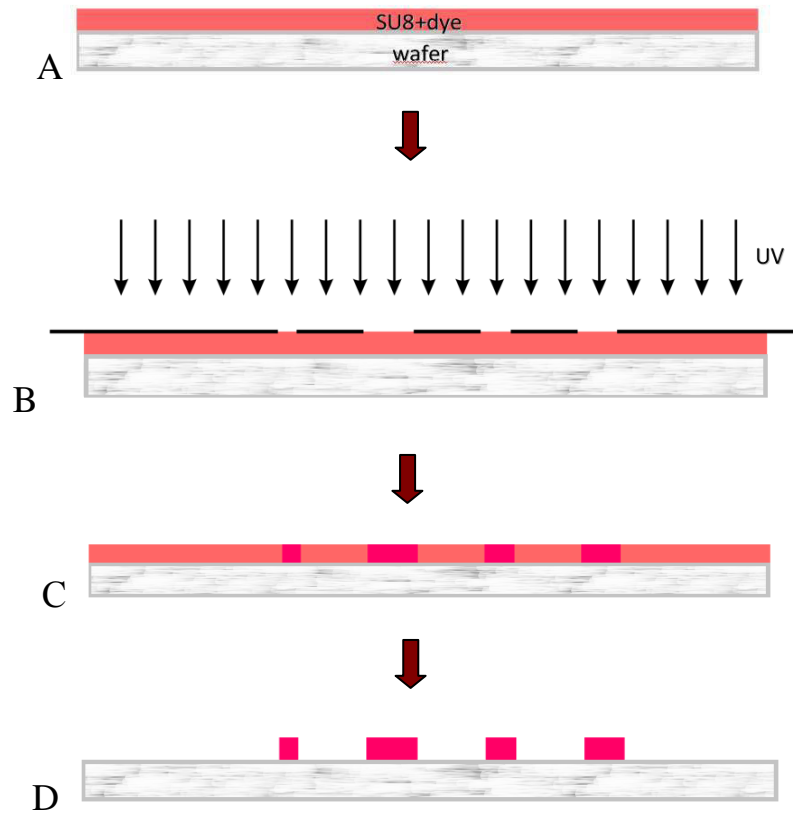


Figure 3.9 — Schematic image of the microstructures obtaining by UV-lithography

Ideally, the soft bake procedure would be performed about T_g temperature of the resist. In the case of the thick SU-8 films, it is carried out into two steps: heating at 65°C for few minutes for reducing tensions and stresses and heating at 95°C for a longer time for drying. The soft bake procedure was performed on hot plates and the duration of the second heating step was increased 6-10 times compared to what is recommended by the producer for a pure resist. This time extension is caused by the fact that recommended soft bake time was not enough for the film drying.

The exposition step was performed on the commercial lithography setup Manual Mask Aligner MJB4 by Suss MicroTec operating with i-line of mercury lamp (exposure power was 17.3 mJ/cm^2). The time of irradiation was determined by the used dye and by the thickness of the layer. In our case, for Rhod 640, the exposure time was about 10 times longer than for PM597 at the same film thickness. The average exposition for Rhodamine lies in the region 150–300 seconds and for Pyrromethene – 15–25 seconds. Exposition was carried out through negative chrome mask designed by me specifically for that purpose and produced by Photronics company. The mask scale was 1:1. It was

shown by experiments that no difference is observed with irradiation of the sample at once or by few exposure cycles with cooling intervals in between (the total time of irradiation was the same).

It should be noted that at the beginning some experiments with the DCM dye in SU-8 were performed by Clément Lafargue during his thesis. But due to the strong absorption of the DCM molecule in the UV-region, the structures were not exposed enough, even with a very long exposure time and, as a result, were washed away during development. The process of the Post Exposure Bake (PEB) also consist of two parts: reducing tensions heating at 65°C and polymerization at 95°C. PEB time was insignificantly increased compared to the recommendation of the producer and was 3 minutes for 65°C and 10-15 minutes for 95°C. After the PEB, the samples were cooled down during 5 minutes. Unexposed parts of the film were removed by developing during 5-10 minutes (depending on the film thickness) in the commercial SU-8 developer. The remnants of the developer were washed away by isopropanol.

The investigation of the quality of the obtained structures was performed with optical and Scanning Electron Microscopy (SEM). On the fig. 3.10, the images of different cuboids from one sample doped by Pyrromethene 605 are presented.

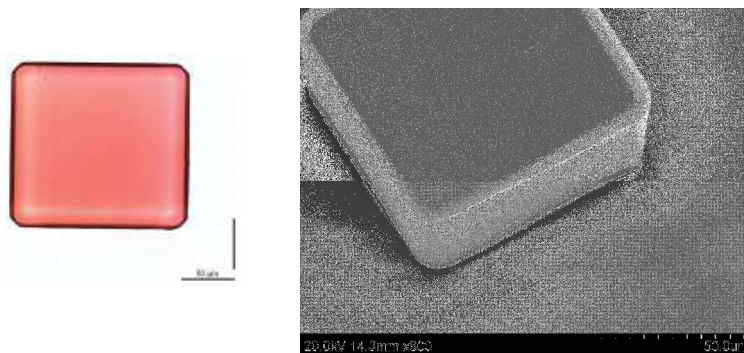


Figure 3.10 — Images of a cuboids doped by Pyrromethene 605 obtained by optical microscopy (on the left) and by SEM (on the right). Square-section size is 150 μm and height is 56 μm

This technology leads to cylindrical microlasers with different cross-sectional shapes. On the fig. 3.11, SEM images of microlasers of the various shapes are shown. All

microcavities have smooth and vertical sidewalls, parallel/perpendicular faces and few defects.

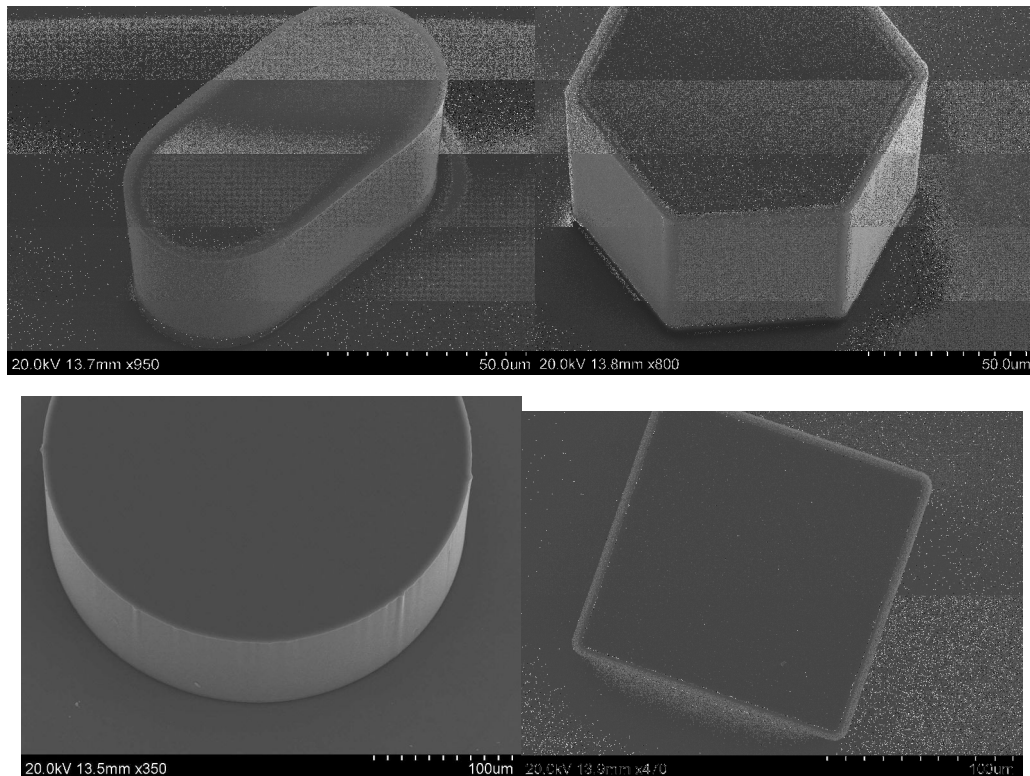


Figure 3.11 — Microlasers of various shapes made by UV-lithography (SU8 doped by dye)

Another main advantage of UV-lithography is the possibility of the simultaneous production of a large number of large structures on the same wafer. On the fig. 3.12, SEM-image of a silicon/silica wafer with Fabry-Perot and cuboid cavities is shown.

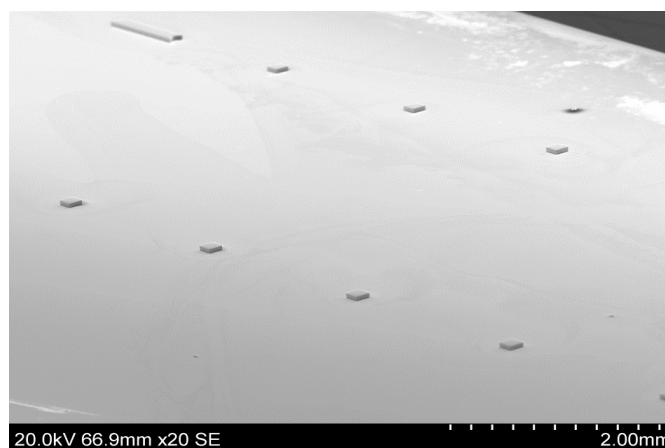


Figure 3.12 — Silicon/silica wafer with different microlasers

It was also noticed that there is a surface quality difference for the structures with Pyrromethene and Rodamine. For comparison, SEM-images of the structures obtained

by UV-lithography from SU-8 doped by Pyrromethene 597 and Prodamine 640 are presented on the figures 3.13 and 3.14, respectively. Even with an optimal exposure, the edges of the structures with Rhod 640 are smoother than with PM 597.

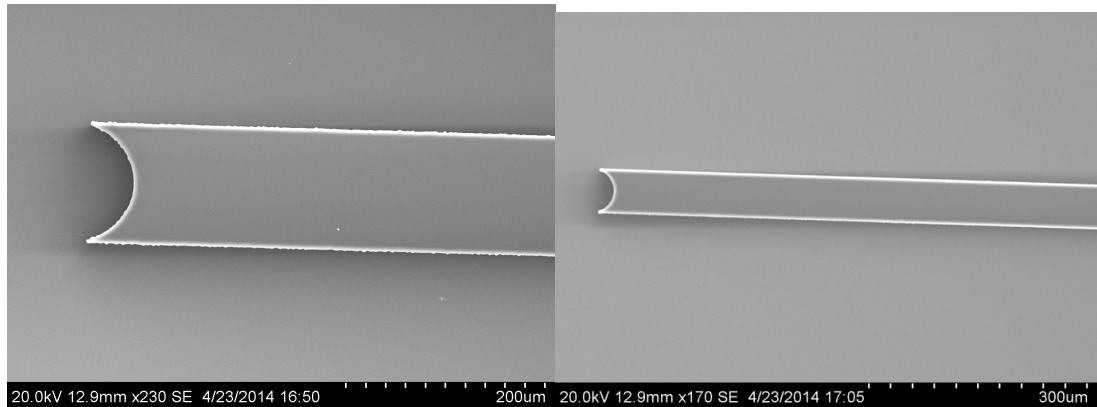


Figure 3.13 — SEM-images of Fabry-Perot microlaser (SU2025, PM 597)

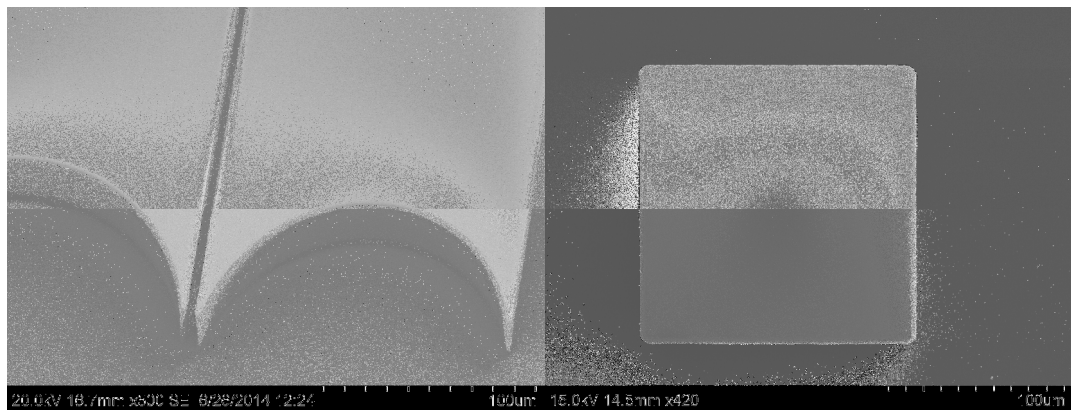


Figure 3.14 — SEM-images of Fabry-Perot microlasers (on the left) and square microlaser (on the right) (SU2025, Rhod 640)

3.3. Direct laser writing by two-photon polymerization (2PP)

Despite of the success in the fabrication of three-dimensional microlasers by UV-lithography, this technology does not allow to implement all desirable goals. For 3-D structures with the variant cross-section we turned to the method of direct laser writing in the resist with the non-linear sensitivity, so called two-photon polymerization.

Due to the short pulse duration, femtosecond pulses have a high intensity (peak power) even at low pulse energy. As a result, multiphoton processes of light absorption are effectively realized on molecular systems under the action of femtosecond pulses.

For implementation of 2PP, femtosecond light pulses are focused in a ‘voxel’ (like a pixel, but in volume) in the monomer solution mixed with an initiator. The monomer is transparent for the used laser radiation, which means that there is no one-photon absorption in the solution at this wavelength. Typically, the used monomers absorb in the UV range and are transparent in the spectral range of 700-800 nm. That is why polymerization occurs only as a result of absorption in the focus of the light beam, where the intensity is high enough to lead to two-photon absorption. The scheme of the radical polymerization mechanism is shown in Figure 3.15.

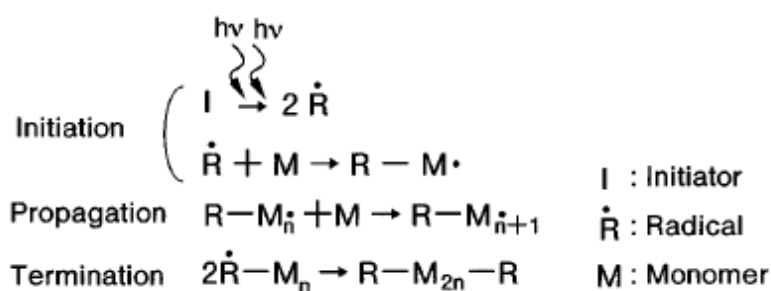


Figure 3.15 — Polymerization mechanism of two-photon absorption

Moving the focus position, the two-photon polymerization can be carried out in the neighboring areas. This means that 2PP is a very promising method of production of micro- and nanostructures of arbitrary shapes. 2PP allows to product computer designed 3D structures by direct laser "recording" in the bulk solution of monomer. Due to the threshold and non-linear nature of the two-photon polymerization, a resolution below the diffraction limit can be achieved by controlling the energy of the laser pulse and the number of these pulses. Multi-photon polymerization allows obtaining structures of high optical quality for different photonics applications: waveguides, microlenses and photonic crystals of various shapes [105]. Due to the possibility of obtaining structures with a variant cross-section (for example, tetrahedron) we were very interested in this technology. The first work in our research group in this field was started by Clement Lafargue. He tried to build the setup for two-photon polymerization by himself, but due to problems with the piezo-stage (no possibility to reduce the response time to the desired value) and the rather significant shrinkage of the resist his attempts were not very successful. Work in this direction was continued in the collaboration with the Joe

Perry group from GeorgiaTech. The results are presented in the corresponding publication [106] and in Fig. 3.18. From now on, the structures are fabricated in the clean room of LPN, Marcoussis (France), by Dominique Decanini on a commercial setup by Nanoscribe GmbH.

In our work, the fabrication process was performed on the commercial setup 3D Lithography laser system by Nanoscribe. As a material for 2PP, we used the resist IPG-780 by Nanoscribe. It is a specially developed sol-gel technology based, high-viscosity, high-resolution and low-shrinkage resist for complex 3D writing trajectories. The dye – Pyrromethene 597- was directly introduced in the resist and mixed before the lithography process. The concentration of the dye was 0.5% by weight of the solution. Scheme of the setup is presented on the fig. 3.16 [107]. A drop of the doped resist is placed on a thin glass on the piezoelectric scanning stage. A femtosecond fiber laser ($\lambda = 780 \pm 10$ nm) is focused by an inverted microscope in the predetermined point in the sample volume. The size of the voxel is represented on the Fig. 3.16 (on the right). Following the pre-written program, the piezo-stage moves and creates the polymerized tree-dimensional structure. After exposing no post bake is required. The non-polymerized material was washed away by developing in PGMEA and isopropanol.

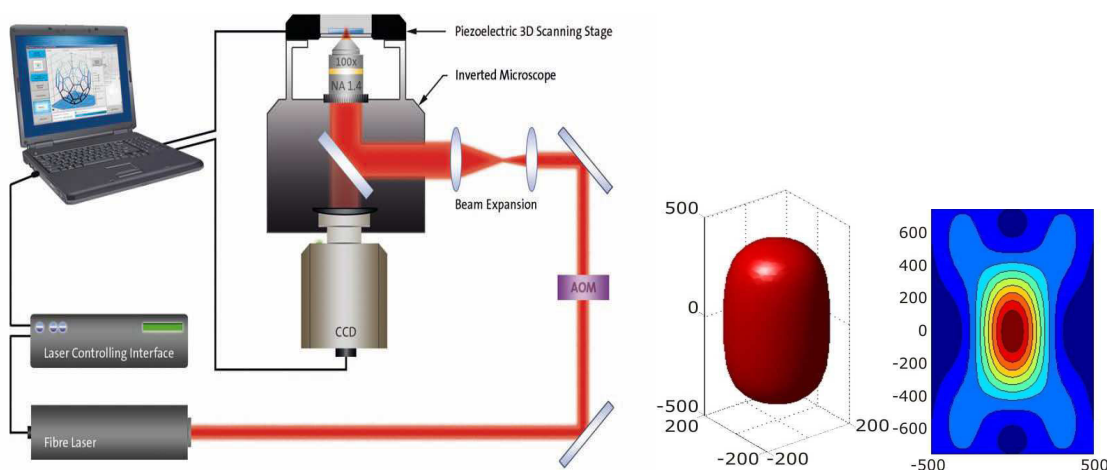


Figure 3.16 — 3D lithography laser system (on the left) and the voxel size (on the right) [107]

Two cuboid microlasers with a cross section side $30 \mu\text{m}$ and a height $10 \mu\text{m}$ obtained by two-photon polymerization are shown on the fig. 3.17. As can be clearly seen on the fig. 17, these two structures with the same form and dimensions were

created by a different algorithm, which determined the beam trajectories. Anyway, it seems that the roughness of the walls and the shrinkage are similar in both cases. The cuboid on the left was created directly on the substrate, while the right one was decoupled from the substrate by 4 posts. The microlaser presented on the fig. 3.18 was fabricated in Perry's group in Georgia Tech and was decoupled from the substrate by a photonic crystal. It can be expected that decoupling microcavities from the substrate would decrease the lasing threshold, in comparison with the usual microcavities on substrate. This question will be considered in the Section 4.2.

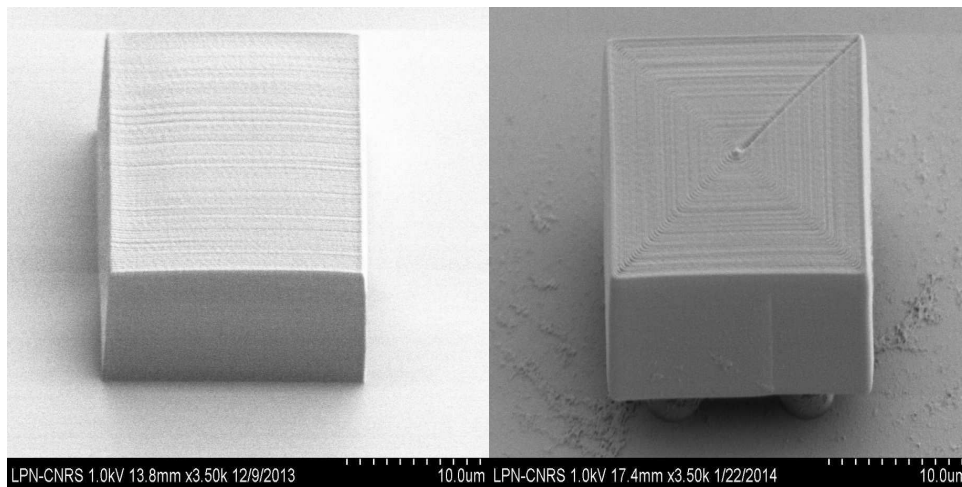


Figure 3.17 — Cuboid microlasers obtained by two-photon polymerization at LPN: directly on the substrate (in the left) and on the posts (in the right).

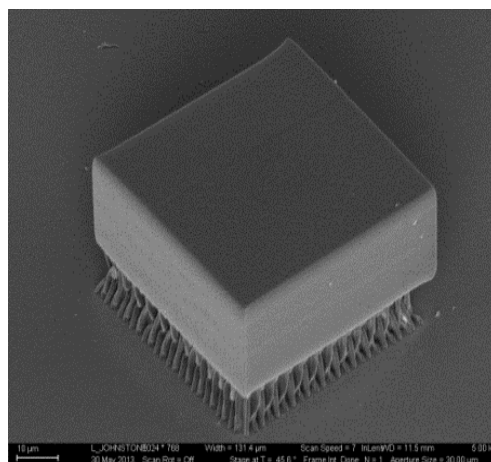


Figure 3.18 — Cuboid microlaser decoupled from the substrate by a photonic crystal obtained by two-photon polymerization at Georgia Tech [106]

Chapter 3 conclusions

In chapter 3, different techniques to fabricate tree-dimensional organic microlasers were investigated. It was shown that two of them: UV-lithography and two-photon polymerization – are efficient. The table 3.1 presents the comparison of these two methods.

Table 3.1 — Comparison of different fabrication methods

	UV-lithography	Two-photon polymerization
Microlaser shape	Only cylindrical cross-section. The thickness is determined by the spin-coating speed. Due to the mask, the angles are rounded.	Arbitrary shape. All three dimensions determined by a program. But strong shrinkage which must be compensated.
Wafer	Different substrates (glass, silicon, silicon/silica etc).	Only thin glass.
Amount of structures	Simultaneous production of a big amount of microlasers.	A single cavity at a time.
Time dependence	The exposure and process time doesn't depend on the amount of structures or on their length and width	Exposure depends on the three microlaser dimensions. For example, increasing twice the edge side of a cube increase the exposure time by 8 times. Typically, the exposure of a pyramid of section size 20 μm is 3 hour long.

Both methods based on commercial available setups and chemical materials have their own advantages and disadvantages. UV-lithography is more suited for the mass microlaser production, while two-photon polymerization has no shape restriction. The comparison of the laser thresholds for structures obtained by both methods is presented in the next section.

Chapter 4. CHARACTERIZATION OF 3D-MICROLASERS

The purpose of this chapter is the characterization of the 3D microlasers described in Chapter 3. In particular, we will describe the set-up and the experimental results. We will then compare the laser thresholds for structures obtained by different methods (UV-lithography and two-photon polymerization), and will discuss the recording of the lasing spectra and the investigation of the corresponding Periodic Orbits (PO).

4.1 The measurement setup

The recording of microlasers spectra and the measurements of lasing thresholds were carried out on the setup, schematically represented in Figure 4.1.

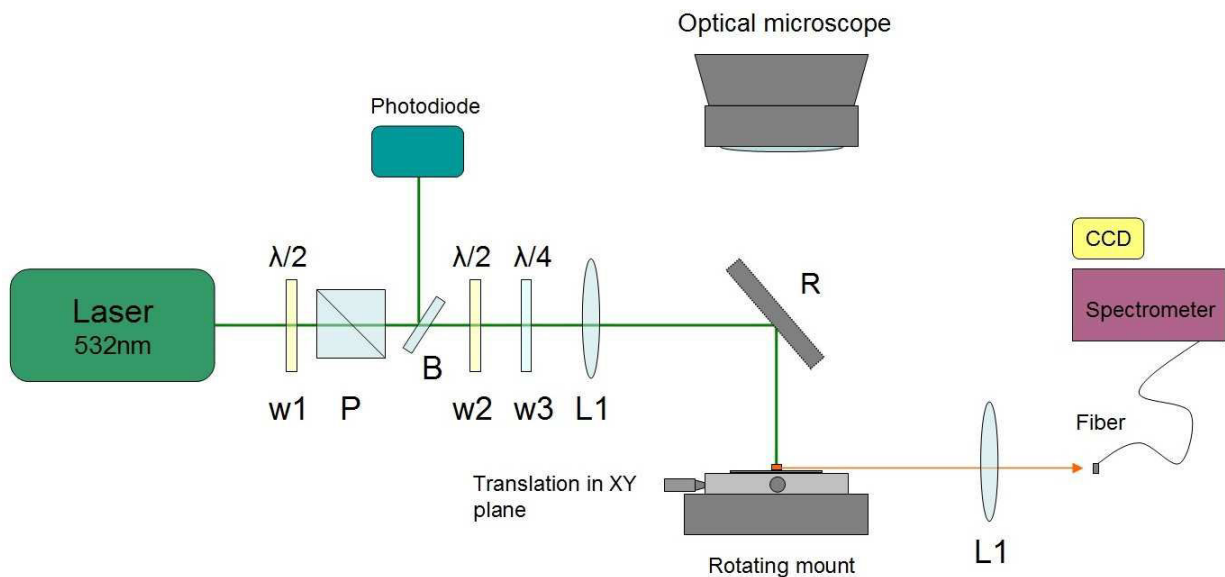


Figure 4.1 — Scheme of the spectra recording setup

Sample with microlasers (silicon/silica or glass substrate) was placed horizontally on the microscope objective table. Optical pumping was initiated from the top, strictly perpendicular to the XY-plane of the sample. As a pump source, a frequency doubled Nd:YAG laser (532 nm, 500 ps, 10 Hz) was used. Pump intensity control was carried out by using a combination of two optical elements: half-wave plate (W1) and

polarizing cube (P). The pump laser emits a linear polarized beam, but only a vertically polarized beam can pass through the cube (P). So, by rotation of the half-wave plate (W1) we change the polarization orientation and, as a consequence, the pump power.

A cube beam splitter (B) reflects a part of the pump beam to a photodetector, which allows to estimate and control the pump power. Then the polarization of the pump beam could be varied by a combination of a half-wave plate (W2) and a quarter-wave plate (W3). It was shown in the work [108] that the pump polarization has a significant influence on the emitted spectra of two-dimensional microlasers. In this work, cuboid microlasers were pumped by a circular polarized beam, but Fabry-Perot by a linear polarized beam.

Diameter of the pump beam was selected as 200 μm , which allows to pump only one individual cavity simultaneously. Beam size was reduced to the desired value by the lens (L1). The laser beam is aligned with the microscope crosshairs that makes easy alignment of the investigated cavity with the pump beam. CCD-camera makes possible to carry out an additional adjustment for the three-dimensional structures, as well as to record photos and videos.

Radiation generated by a microlaser in the XY plane was collected by a lens (L2) (in one particular direction) and transmitted via an optical fiber to the spectrometer (Spectra Pro 2500i, Acton Research). A short schematic explanation of the measurement of a cube shaped microlaser is represented on figure 4.2.

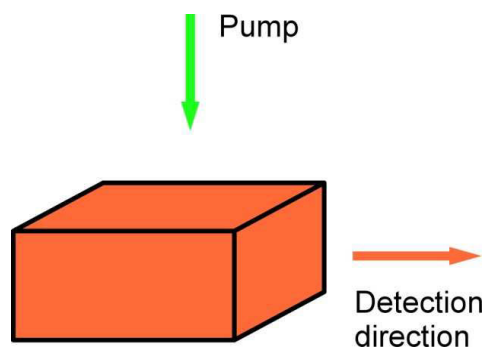


Figure 4.2 — Scheme of the spectrum measurements of a cube microlaser: green arrow - the pump, red line – selected direction of the radiation collection

Usually measurements were made in the direction perpendicular to the side face of the microlaser (red line on the figure 4.2). However, thanks to the rotation of the stage, it is possible to investigate the emission diagrams throughout the XY plane.

4.2. Tresholds measurements

All microlasers showed multimode lasing and have certain thresholds.

For continuous lasers, the laser treshold is determined as the pump intensity which is necessary to compensate the full losses by amplification in the active medium. In the case of pulsed lasers, it has sense to talk about the pump power accumulated in the active medium. In our configuration, it seems that the micro-lasers are in a stationnary regime [109].

Figure 4.3 shows the dependence of the microlaser intensity on the pump energy. This measurements corresponds to a cuboid microlaser with a square cross-section of size $35\ \mu\text{m}$ and height $26\ \mu\text{m}$.

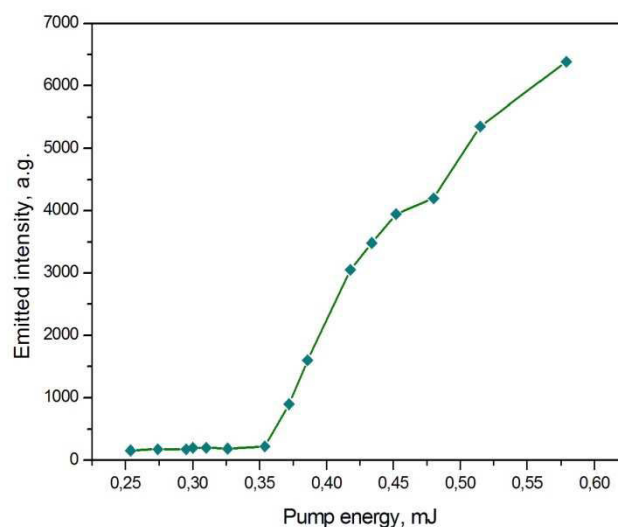


Figure 4.3 — Dependence of the emitted intensity on the pump energy for a cuboid microlaser with a square cross-section of size $35\ \mu\text{m}$ and height $26\ \mu\text{m}$ (Pyrromethene 597)

Usually threshold decreases with the increase of the cavities size due to the increase of the active medium volume. But also it looks like surface quality has an effect on the threshold value. For example, for microlasers of the same size doped with

the same laser dye and obtained by UV-lithography, the difference in values can be up to 2 times.

Besides, the comparison of the thresholds was made for three types of structures of similar size: 1 – (black curve) – cube with size 30 μm obtained by UV-lithography; 2 – (red curve) – cuboid with a square cross-section of size 30 μm and height 10 μm obtained by two-photon polymerization; 3 – (blue curve) - cuboid with a square cross-section of size 30 μm and height 10 μm obtained by two-photon polymerization and decoupled from the substrate by four posts (see figure 3.17). Results of the measurements are presented in the figure 4.4.

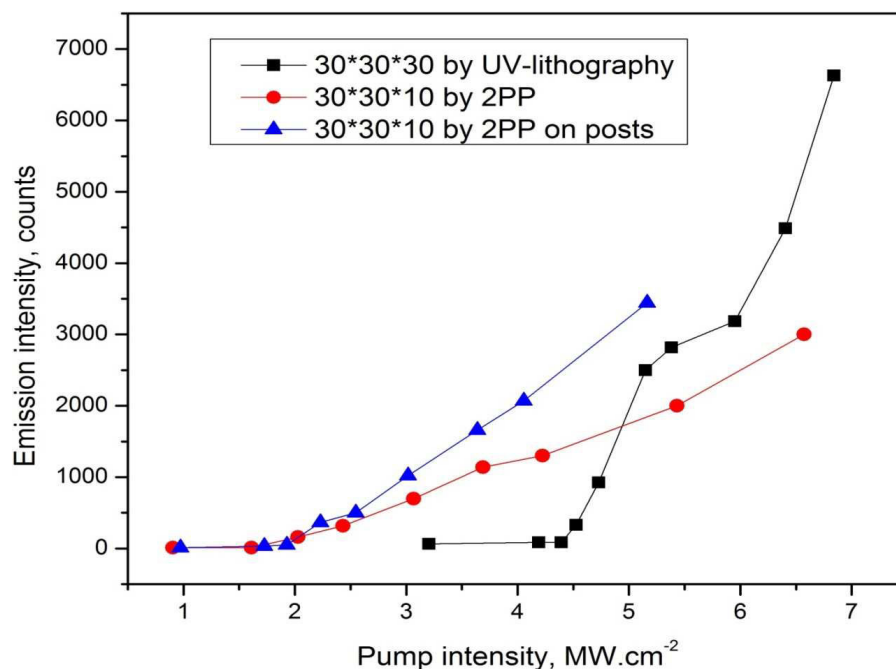


Figure 4.4 — Dependence of the emitted intensity on the pump power for cuboids microlasers (Pyromethene 597), obtained by UV-lithography (black curve), two-photon polymerization (red curve) and two-photon polymerization on posts (blue curve). The size in microns is indicated in the legend

From the series of the measurements it is possible to make the conclusion that threshold for microcavities made by UV-lithography is usually 2-3 times higher than in the case of two-photon polymerization. In particular, the experimental thresholds considered here were 4.5 $\text{MW}\cdot\text{cm}^{-2}$ vs. 2 $\text{MW}\cdot\text{cm}^{-2}$ respectively. Lower threshold for the

microlasers obtained by two-photon polymerization can be explained by the suggestion that better surface quality of the facets leads to the lower losses and, as a consequence, it is more important for the generation than the perpendicularity of the facets. Also, it should be noted that in the case of the UV-lithography the maximum of the emitted radiation, as usual, was observed in the direction perpendicular to the microlaser facet. But for the two-photon polymerization structures maximum intensity was registered at a deviation of a few degrees from the perpendicular direction.

On the other hand, the difference in laser threshold for microcavities decoupled from the substrate and not decoupled (ie. on posts vs. directly on the substrate) is rather small, contrary to expectations. In this case, it is 1.9 MW.cm^{-2} vs. 2 MW.cm^{-2} .

The issue of laser threshold for Fabry-Perot microlasers will be considered in the section dedicated to periodic orbits.

4.3 Spectra and periodic orbits

In this section, we will discuss periodic orbits in three-dimensional microlasers of simple forms.

From the geometrical point of view, the light confined inside a cavity travels along a trajectory, reflecting from the cavity walls. If the trajectory is periodic and if there is enough gain, it leads to light amplification and generation of laser emission. Such trajectory is called a Periodic Orbit (PO) and its length can be obtained from the spectrum analysis, as explained below. In a conventional laser like the typical Fabry-Perot, resonant modes are localized on the simplest periodic orbit, which passes from one mirror to the other and back (see fig. 4.5). In this case the periodic orbit length is determined as $L = 2a$ and optical length $L_{\text{opt}} = 2a \cdot n$, where n is the refractive index of the medium.

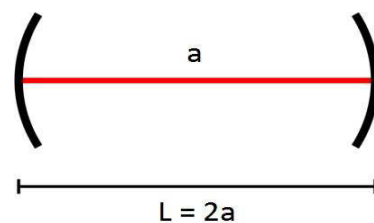


Figure 4.5 — Periodic orbit in a classical Fabry-Perot resonator

For dielectric cavities, orbits can be more complicated and also be one- two- or three-dimensional. Figure 4.6 presents some examples of the possible periodic orbits in a flat (2D) square cavity.

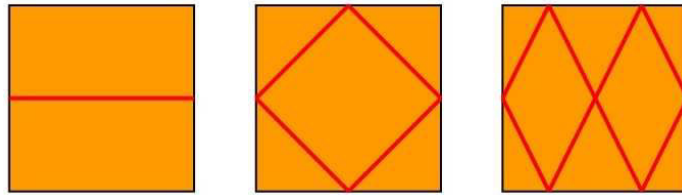


Figure 4.6 — Some possible periodic orbits in a two-dimensional square resonator

A typical spectrum from three-dimensional microlaser is shown in figure 4.7. This spectrum corresponds to a cube microlaser doped with PM597 with side length 30 μm , obtained by UV-lithography. The pump intensity was close to the laser threshold.

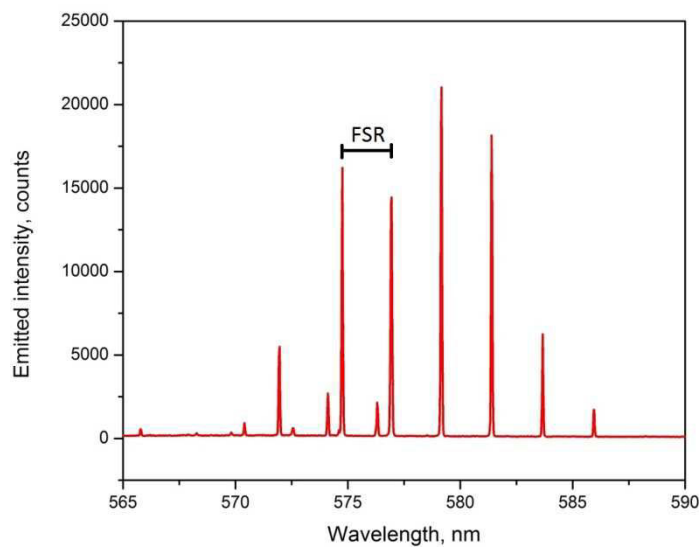


Figure 4.7 — Experimental spectrum from a cube (30×30×30 μm) microlaser, SU8 + Pyrrromethene 597

The distance between two adjacent peaks, so-called Free Spectral Range (FSR), is an important characteristic of the spectrum. In the investigated spectrum, the FSR looks constant. Such equidistant spectral comb confirms that the resonant modes are longitudinal modes, localized on a single periodic orbit inside the microlaser [59, 61]. In this case resonance condition determines the length of the periodic orbit. It is equal to an integer number of wavelengths. It can be described as:

$$\mathbf{k_m L_{po} = 2\pi m} \quad (4.1)$$

where \mathbf{k}_m – resonant wavenumbers (i.e. spectral peaks positions), $L_{po} = \mathbf{n} * \mathbf{l}$ – optical length of the periodic orbit, which can be calculated as a multiplication of the geometrical length of the periodic orbit and of the refractive index of the active medium, \mathbf{m} – integer number.

Therefore, the FSR is defined by $\Delta \mathbf{k} = \mathbf{k}_m - \mathbf{k}_{m-1}$ and is given by:

$$\Delta \mathbf{k} = \frac{2\pi}{n_g l_{po}} \quad (4.2)$$

where \mathbf{n}_g – group refractive index taking into account the dispersion of the refractive index [59].

It also should be noted that on the Figure 4.6 we observe some small peaks shifted relatively large peaks. These peaks correspond to another family of resonant modes with the higher threshold. The distance between the small peaks and the large peaks is the same that indicates that they correspond to the one periodic orbit.

It is clear that distance between adjacent peaks is in inverse ratio to the periodic orbit length. So, by changing microlasers dimensions it is possible to change the microlasers spectral properties and even to obtain single-mode lasing.

As follows from the equation (4.2), the geometrical length of the periodic orbit can be inferred from the spectrum by directly measuring its FSR. Also periodic orbits can be identified by using the Fourier Transform (FT) of the spectrum. It was shown in [59], that in the case of equidistant spectrum, its Fourier Transform displays harmonics, which first peak corresponds to the optical length of the periodic orbit in the investigated microlaser. The position of the first peak is $L_{opt} = \mathbf{l} * \mathbf{n}_g$. The value of \mathbf{n}_g for the investigated material can be obtained from ellipsometric measurements or by calibration on a similar sample.

4.3.1 Periodic orbits in three-dimensional cuboid microlasers

Unfortunately we have some problems with the refractive index definition. The ellipsometry measurements are not very reliable for our case. It is required to use the layer thinner than $1\mu\text{m}$, but it is not possible to obtain it from solutions used for 30-100 microns thickness structures. Also it will be shown later, refractive index values can be

different for samples, obtained from solutions prepared at different times. So, we used cuboid to calibrate the refractive index, since the lasing periodic orbit is clearly identified. This section deals with this issue.

One of the most expected periodic orbit in the case of cuboid microlasers is the two-dimensional diamond orbit lying in the plane XY and having total internal reflection from each wall of the cuboid. Its form is schematically represented in figure 3.8.

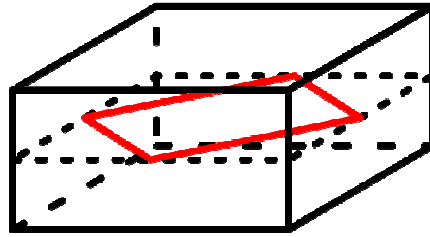


Figure 3.8 — “2D diamond” orbit in a cuboid.

The optical length of this orbit can be calculated as $L_{opt} = n_g * l$, where l is the geometrical length of this PO, which for cuboid with square cross-section with side length a is $l = 2\sqrt{2}a$. So the optical length of the 2D diamond orbit for the cuboid with square cross-section is:

$$L_{opt} = n_g 2\sqrt{2}a \quad (4.3)$$

where a is the side length of the square cross-section. The refractive index of the polymer doped by a dye should be not significantly bigger than the refractive index of the pure SU-8 which is 1.6. From the other side, the optical length L_{opt} can be experimentally identified from the spectrum analysis using the Fourier Transform as described in the previous Section.

In order to confirm or to deny the hypothesis about the 2D diamond orbit, two series of experiments were carried out. The investigated structures were obtained by Vincent Chen by multiphoton lithography in the group of Joseph Perry at Georgia Tech. In that case, the material was an acrylate host resist doped with PM597. The refractive index is expected to be close to 1.5. The measurements were performed by Stefan Bittner. In the first experiments three cuboids with the same height $42\mu\text{m}$ and with different square cross-sections were measured. The results are presented in figure 4.9:

blue line indicates the optical length for 2D diamond orbit calculated by formula 4.3, red dots – experimental data obtained from the FT of the spectra. It is clear that experimental and theoretical optical lengths correspond very well.

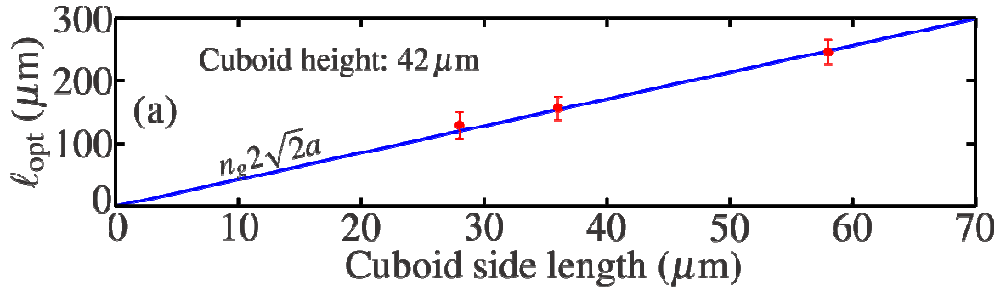


Figure 4.9 — Optical length of cuboids with the same height, but different cross section: blue line – calculated data, red dots – experimental data. The refractive index used for calculation was 1.51 [106]

In the second experiments, seven cuboids with the same square cross-section (with side length 58 μm), but with different heights were measured. These results are shown in figure 4.10: the blue horizontal line indicates the optical length for 2D diamond orbit calculated by formula 4.3 with $n_g=1.51$, red dots – the experimental optical lengths obtained from the FT of the spectra.

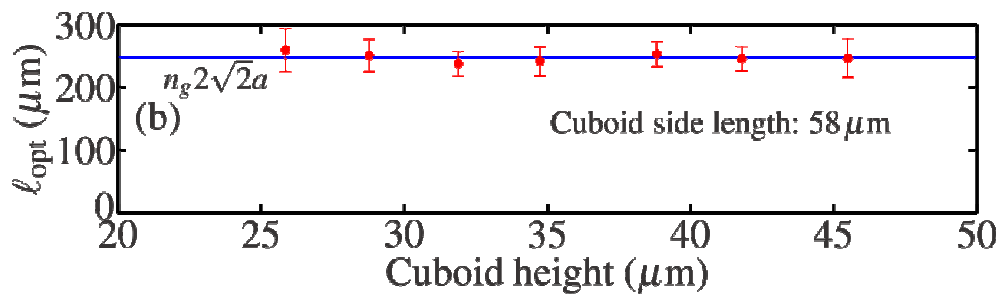


Figure 4.10 — Optical lengths of cuboids with different heights, but with the same cross-section: blue line – calculated data, red dots – experimental data. The refractive index used for calculation was 1.51 [106]

It is obvious that in the case of structures with the same cross-section and different heights the optical length of the periodic orbit has the same value. It means that periodic orbit length does not depend on the height, i.e. there is no reflection from the bottom

and top facets. This is a confirmation of the 2D nature of the periodic orbit. In practice, the 2D diamond is the only possible periodic orbit which can fit the data with a reasonable refractive index value.

Also cuboids with square cross-section with side lengths from 30 to 100 μm and height 25-30 μm , obtained by UV-lithography and doped by Pyrromethene 597 were analyzed too. The obtained results are similar to those described above. For completeness, the same experiment was carried out for cuboid microlasers doped by Rhodamine 640. It leads to similar results. These facts unequivocally confirm that the observed periodic orbit is the 2D diamond orbit.

4.3.2 Refractive index determination

Knowing which orbit we observe, it is easy to infer the refractive index of the material from equation (4.3). As a result, due to the fact that all observed orbits in cuboid microlasers with square cross-section were clearly identified as 2D diamond, we found an easy method to calibrate the refractive index.

For instance, let us consider the calibration of the refractive index for SU-8 doped by 0.5% wt of Rhodamine 640. Ten cuboids (on the same sample) with different cross-section sides were investigated. The optical lengths of the corresponding periodic orbits were obtained from the Fourier transform of the spectra. Then the geometrical lengths of the periodic orbits were calculated using the following formula (4.3) for the 2D diamond orbit (see Table 4.1).

Table 4.1. Values of the n_g obtained from the optical lengths (cuboids with different size on one sample)

Side length, μm	L_{opt} from FT	N_g
25	121	1,71
30	138	1,63
35	158	1,60
40	187	1,65

45	211	1,66
50	231	1,64
60	269	1,59
70	321	1,62
80	370	1,64
90	423	1,67
100	468	1,66
140	646	1,63

The difference in the refractive index values is not significant: the minimal obtained value is 1.59, the maximum – 1.71. The average value is **1.64**. In this case the standard deviation value is 0.032. It should be noted that at first some enlargement of the structures due to the expected dimensions were observed. But the technology improvement allowed to obtain structures with the desirable parameters. It means that the maximum difference between expected and real size is about 0.5 μ m. So, the possible error due to the different structures' size can't make a significant contribution to the variation of the refractive index values.

Similarly, for the SU-8 polymer matrix doped by Pyrromethene 597 (0,5% wt) it was found that $n_g = 1.73$ and for SU-8 doped by Rhodamine 640 (0,5% wt) $n_g = 1.64$.

For example, in Figure 4.11, the Fourier Transform of the spectrum plotted in the Figure 6 is presented.

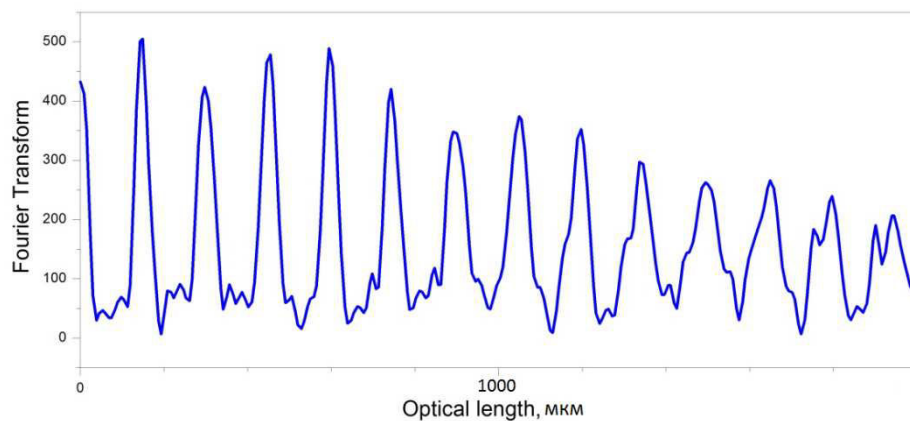


Figure 4.11 — Fourier Transform of the spectrum in Figure 6 from a cuboid microlaser (SU-8 + PM597)

The position of the first harmonics corresponds to $149\ \mu\text{m}$. Cross-section size is $30\ \mu\text{m}$. If the refractive index is $n_g = 1.73$ for SU8-PM 597, then the calculated optical length is $L_{\text{opt}} = 147\ \mu\text{m}$, which means that we have a very good correspondence between theoretical and experimental data. In practice, we estimate the precision of the geometrical length to 5%.

4.3.3 Periodic orbits in three dimensional Fabry-Perot microlasers

The second simplest investigated microlasers shape is the Fabry-Perot. At first it is necessary to give a short comment on what we mean by a Fabry-Perot shape of microlaser. The figure 4.12 contains the schematic explanation of the Fabry-Perot microlaser's shape and the explanation of its measurement algorithm.

It is a very long rectangle (1mm-along X direction) with two optical traps at the ends, which prevent light propagation in the longitudinal (X) direction. The green line on the figure is a pump beam strictly perpendicular to the top facet; red line – direction of the emitted radiation detection, this direction is perpendicular to the lateral facet. Pump polarization for all Fabry-Perot measurements was linear, along the X axis. In this work we investigate microlasers with the different size in the (Y) direction – below and thereafter the “width”.

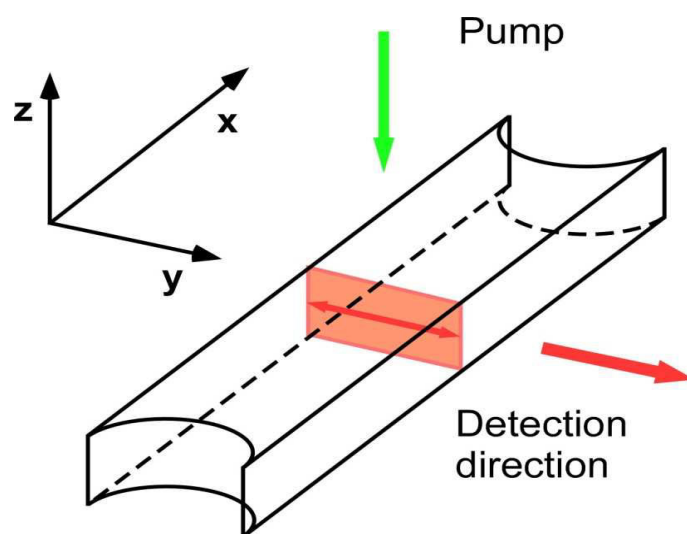


Figure 4.12 — Scheme of spectrum measurements of the Fabry-Perot microlaser: green arrow - the pump, red line – selected direction of the emission collection.

Two images of a Fabry-Perot microlaser are shown in figure 4.13, under an optical microscope, and under pumping.

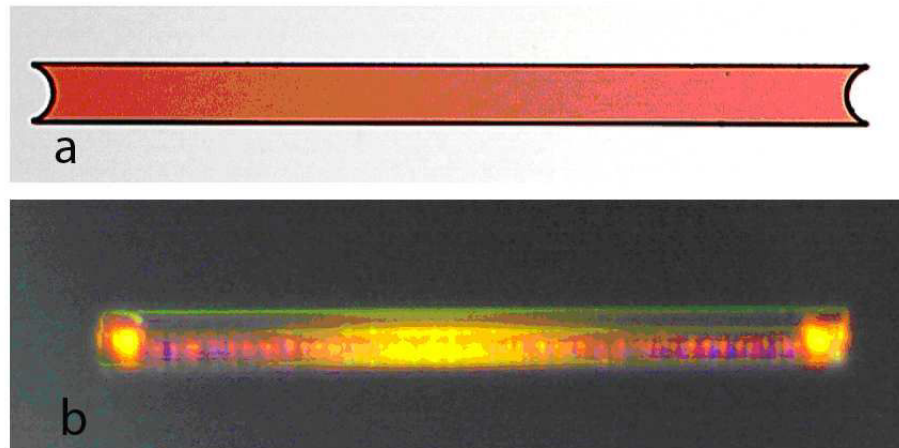


Figure 4.13 — Fabry-Perot microlaser with a width $70\mu\text{m}$ (PM597): a – top view of the microlaser with an optical microscope, image in real colors ; b – side view, green light – pump, yellow light – emission from the microlaser

This shape was studied for two different purposes. (i) It was first expected that it would be possible to use this shape for calibration and alignment. Actually in the two-dimensional case, only the simplest Fabry-Perot periodic orbit with the length $l = 2w$ was observed [59], where w is the width of the microlaser. But it appeared that using cuboids was easier for calibration. (ii) Due to the translational invariance along X , it is in fact a reduction of a 3D to a 2D system, but the plane where periodic orbits are expected to exist is vertical, as shown in Fig. 4.12. So we thought that it would be a simple 3D shape to investigate.

4.3.3.1 Fabry-Perot microlasers doped by Pyrromethene 597

At first, all the measurements were performed on structures doped by Pyrromethene 597. Microlasers with different widths (50, 60, 70, 80, 90, 100, 120, 140, 160, 180 and $200\mu\text{m}$) were investigated. The thickness of the microlasers was about 25 microns. With a width of less than 100 microns spectra look non-equidistant, without any order or periodicity. An example of such spectrum is shown in figure 4.14. It was not possible to infer a periodic orbit.

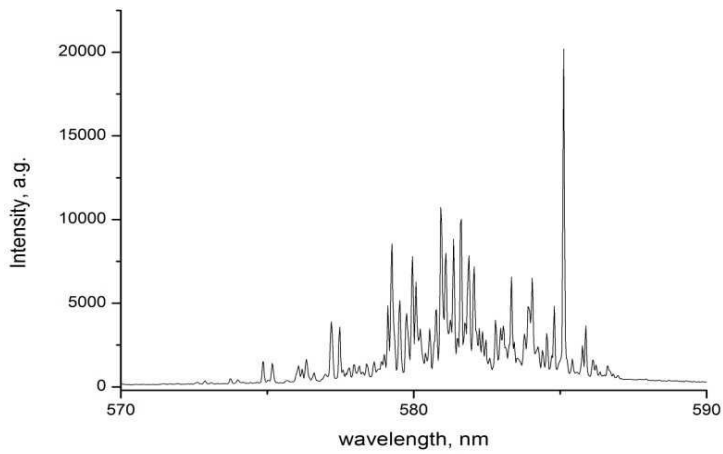


Figure 4.14 — Fabry-Perot microcavity spectrum, width 80 μ m, PM597

For a microlasers with a width bigger that 100 μ m, the spectrum consists of two parts (see Fig. 4.15): equidistant (in the left) and non-equidistant (in the right). Figure 4.16 contains the emlarged left part of the spectrum from fig. 4.15. As in the case of Figure 4. 7 here we also observed two series of the peaks corresponding to the two families of modes with the different thresholds. The Fourier analysis showed that the left part of the spectrum (both families) corresponds to the expected Fabry-Perot periodic orbit.

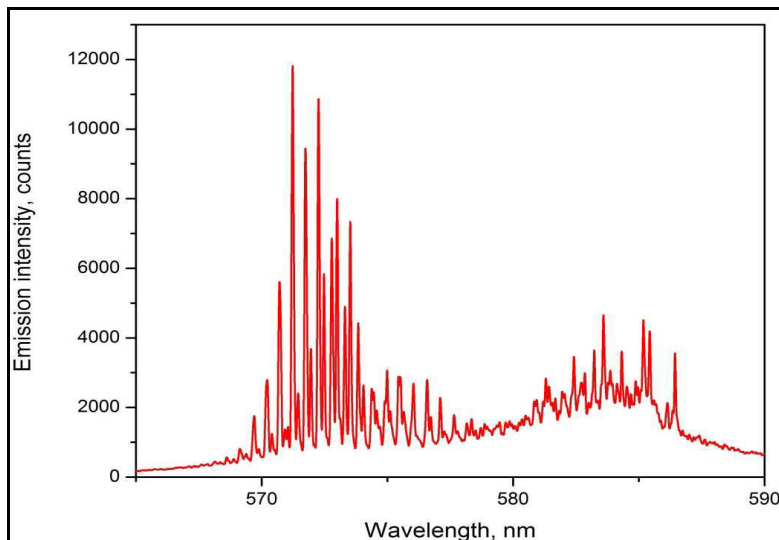


Figure 4.15 — Spectrum of Fabry-Perot microlaser with width 180 μ m (PM597)

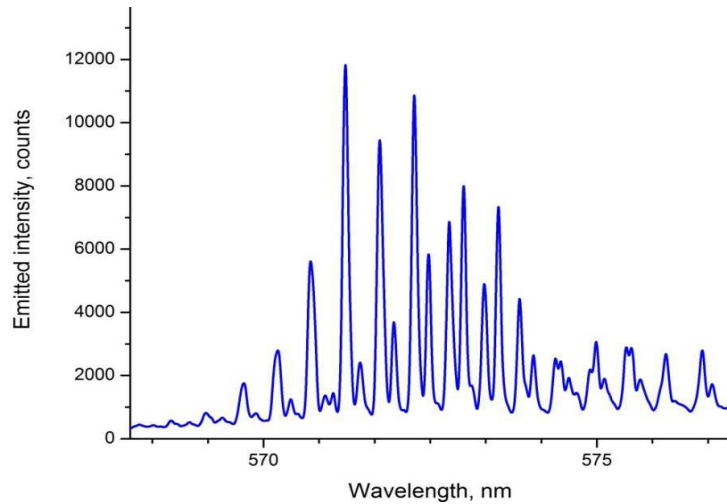


Figure 4.16 — Enlarged left part of the spectrum presented in figure 4.15

Figure 4.17 illustrates the evolution of the spectrum for a Fabry-Perot microlaser with width $180\ \mu\text{m}$ while increasing the pump intensity. It is clearly seen that in the case of the microlasers with a width less than 180 microns the “Fabry-Perot part” appears after the “non-equidistant part”. It means that the “Fabry-Perot part” has a higher threshold than the “non-equidistant part” of the spectrum. At the same time, the threshold of the “Fabry-Perot” part decreases with the increasing of the microlasers’ width. With increasing the pump intensity, the Fabry-Perot part, if it appears, always starts to dominate in the spectrum (see fig. 4.17), which means that it has a better outcoupling efficiency than the “non-equidistant part”.

The etching quality is quite poor with PM597, and aggregates are observed. Cavities with PM597 could then generate random lasing, which may be the reason why spectra of the microlasers with the widths 60-90 microns doped by Pyrromethene look non-equidistant. However, we must be careful. Spectra could also look non-equidistant due to a big amount of peaks and the insufficient resolution of the spectrometer.

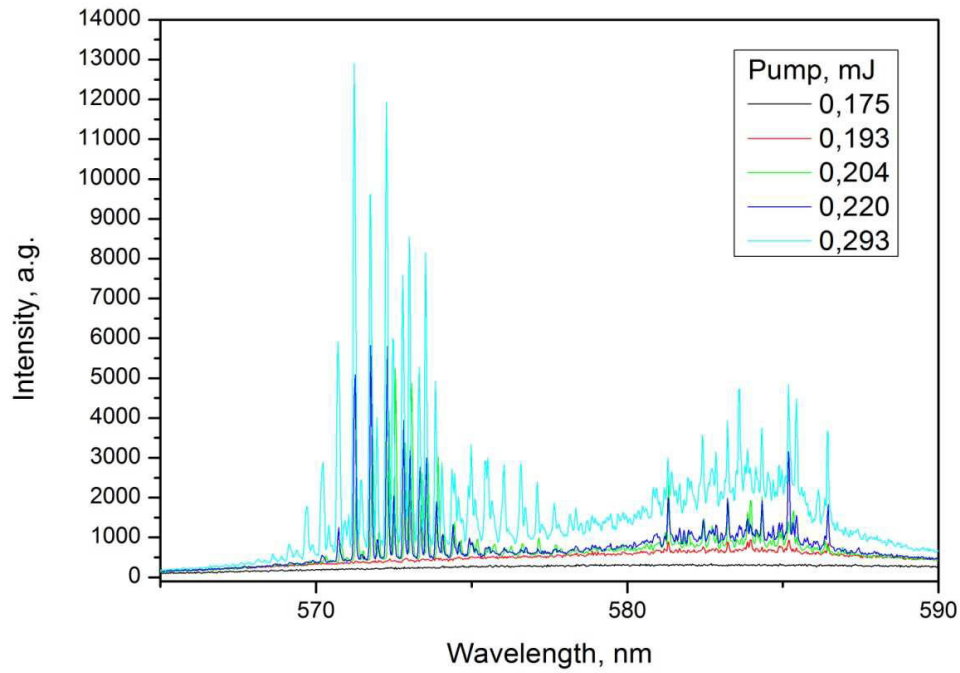


Figure 4.17— Spectrum evolution of a Fabry-Perot microlaser with width 180 μm (PM597) while increasing the pump intensity (in arbitrary unit).

However a more precise investigation of the spectra showed that “non-equidistant” doesn’t mean that there is no periodic orbit. It can be explained by using a dye with a very high gain in a non-homogeneous medium, which leads to random lasing. In some rare cases, “non-equidistant” spectra have some order, for example in figure 4.18, where the spectrum of a microlaser with width 70 μm is presented.

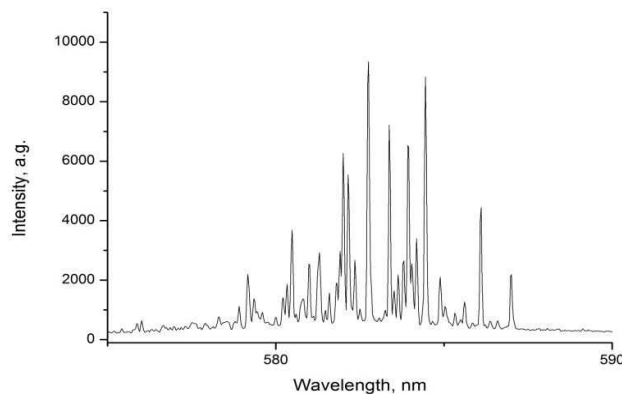


Figure 4.18 — Fabry-Perot microlaser spectrum with width 70 μm (PM597)

The orbit identification is possible and the Fourier Transform gives an optical length $L_{\text{opt}} = 320 \mu\text{m}$. Also optical length was calculated by directly measuring the FSR from

the spectrum and the results were the same. For the width 70 microns optical length for Fabry-Perot periodic orbit should be 230 microns (for $n = 1.64$). So it is clearly indicated that observed orbit is not a Fabry-Perot orbit.

For Fabry-Perot microlasers with widths in the range 100-200 μm , the observed periodic orbit is unambiguously identified as the Fabry-Perot orbit. Comparison of the experimental and calculated data is presented on figure 4.19.

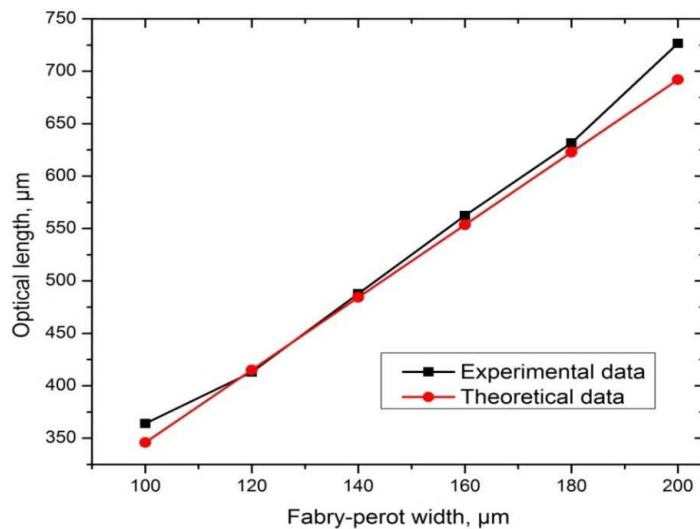


Figure 4.19 — Optical length of the periodic orbit inferred from the experimental spectra versus the microlaser width: black line – experimental data, red line – calculated (PM 597)

4.3.3.2 Fabry-Perot microlasers doped by Rhodamine 640

The same measurements and their treatment were performed for Fabry-Perot microlasers doped by another dye – Rhodamine 640. The widths range was the same: from 50 μm to 100 μm with step 10 μm and from 100 μm to 200 μm with step 20 μm . Against expectations we observed not the same results as for Pyrromethene 597. All the spectra contain only one part and look equidistant, even for the smaller widths – from 60 μm . For comparison, spectra of two microlasers with widths 70 μm and 180 μm are presented on figure 4.20.

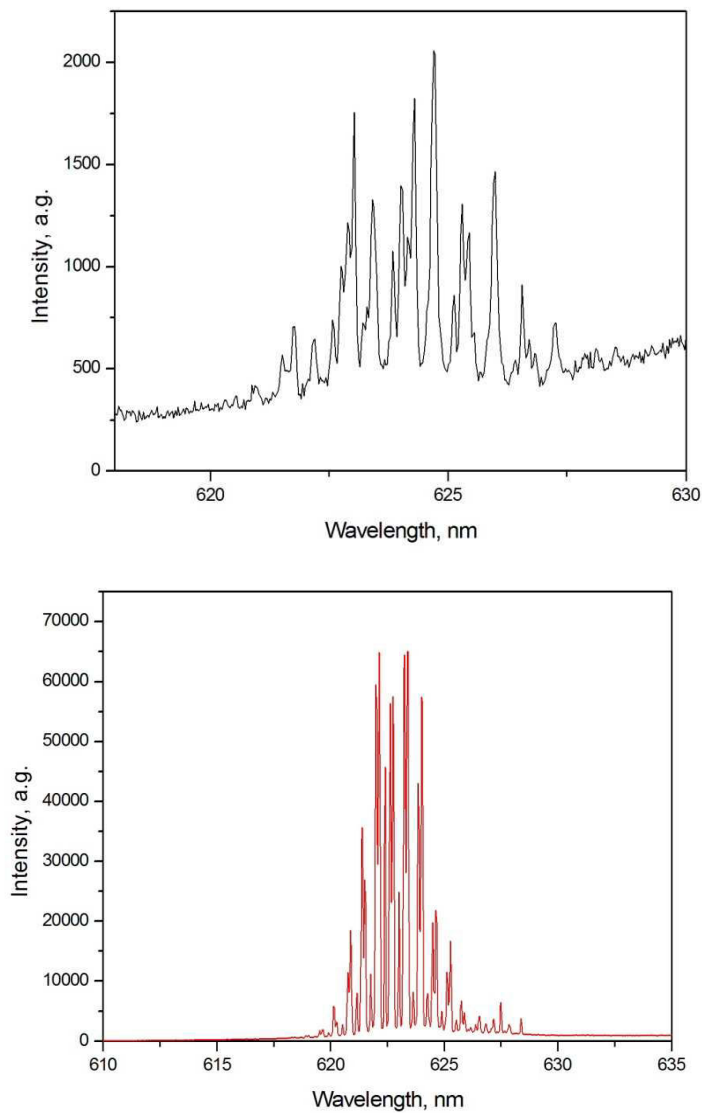


Figure 4.20 — Fabry-Perot microlasers spectra (SU-8 + Rhod640): at the top – microlaser’s width 70 μm , at the bottom – microlaser’s width 180 μm

It is important to notice that all the structures investigated before, either with PM597 or with RH640, were fabricated on a silicon/silica substrate (silicon substrate with 2 μm silica layer). For comparison, structures doped by Rhodamine 640 on a glass substrate were obtained and the measurements were performed. These spectra consist only from one equidistant part, observed from the width 120 μm .

All results with Fabry-Perot doped by RH640 are gathered in table 4.2:

L_{opt1} and L_{opt2} – experimental data obtained from the Fourier Transform of the spectra for 2 different samples on a silicon/silica wafer. They were fabricated in different times from different solutions (Rhodamine 640 0.5% wt).

$L_{opt\ glass}$ – experimental data (obtained from the Fourier Transform of the spectra) for a sample doped by Rhodamine 640 on a glass wafer.

$L_{opt\ calc\ FP}$ – calculated optical length for all considered widths. The used refractive index is $n_g = 1.64$. This value was obtained as an average value. The calibration process is described at the paragraph 4.3.2. Figure 4.21 graphically displays the data from the table 4.2.

Table 4.2 — Optical lengths dependence on the widths (experimental data – columns “ L_{opt1} ”, “ L_{opt2} ” and “ $L_{opt\ glass}$ ”; calculated data – column “ $L_{opt\ calc\ FP}$ ”, all structured are doped by Rhodamine 640). Experimental values having a good correspondence to Fabry-Perot orbit are bolded

Width	L_{opt1}	L_{opt2}	$L_{opt\ glass}$	$L_{opt\ calc\ FP}$ 1,64
60	274	270		196,8
70	307	307		229,6
80	340	375		262,4
90	409	397		295,2
100	440	438		328
120	560	570	420	393,6
140	615	600	490	459,2
160	665	650	565	524,8
180	611	611	625	590,4
200	683	685	690	656

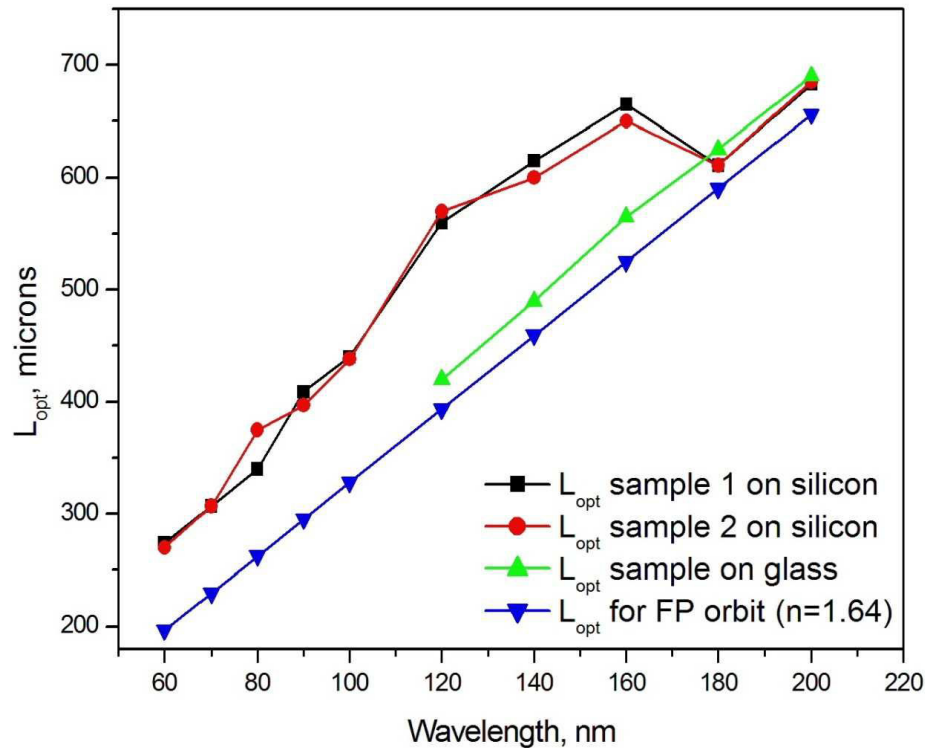


Figure 4.21 — Dependence of L_{opt} on the width of microlasers for samples on silicon and on glass (Rhodamine 640). L_{opt1} , L_{opt2} and L_{opt} glass – experimental data for 3 different samples, L_{opt} calc FP – calculated data

First of all, the experimental results from different samples (on silicon) are actually identical that evidences a rather high reproducibility. Secondly, in the case of glass substrate, we observe periodic orbits starting from 120 μm width and they correspond to the Fabry-Perot orbit. The agreement with the calculation is not good. The most probable reason is a discrepancy of the refractive index, because it seems that there is just a constant shift. For cavities on silicon, it looks like we observe Fabry-Perot periodic orbit only for the microlasers with the biggest widths (180 and 200 microns). For smaller widths, the lasing periodic orbits have longer lengths than the Fabry-Perot orbit, which are not identified yet. This issue is discussed in the next paragraph.

An important issue is that the results depend on the dye. A comparison is presented in the table 4.3 for RH640 and PM597 either on glass or on silicon.

Table 4.3 — Comparison of the results depending on the wafer and dye

Dye Wafer	Pyrromethene 597	Rhodamine 640
Silicon/silica	Lasing spectra observed from a microlaser width of 60 microns. Spectra for width 60-90 microns contains a lot of peaks and look non-equidistant. For widths 100-200 microns spectra consist of two parts: looking non-equidistant and corresponding to Fabry-Perot orbit.	Lasing spectra appear starting from a microlaser width of 60 microns. Spectra show a single part. Spectra look equidistant from the moment of observing any lasing. Optical lengths obtained from the FT do not correspond to Fabry-Perot orbit.
Glass	There is no enough data for Pyrromethene on glass. Some samples were made long ago just to see, that we can do it on glass too	Lasing spectra observed from a microlaser width of 120 microns. Optical lengths obtained from the FT correspond to Fabry-Perot orbit.

Such difference for two dyes can be explained by the fact that Pyrromethene 597 has a bigger gain than Rhodamine 640. Another possible explanation is that structures doped by Pyrromethene have a worse quality of the edges (see figures 3.13 and see 3.14). This phenomenon can lead to the spectra deterioration. So, in two microlasers with the same shape and dimensions, doped by different dyes in the same concentration, we can observe different periodic orbits with different thresholds.

It should be noted that optical length value obtained by FT from the spectrum on the Fig. 4.18 (70 microns width, Pyrromethene 597) is rather close to the optical length value for the microlaser with the same width doped by Rhodamine 640 (see Table 4.2): 320 and 307 microns, respectively. Due to the refractive index differences $n_{PM} = 1.73$ and $n_{RHOD} = 1.64$, we obtain the same geometrical length (185-187 microns) for the periodic orbit in both structures with the same dimensions.

4.3.3.3 Possible periodic orbits investigation

We face two main problems to interpret the above data. First the orbit optical lengths are different for the same structures (dimensions and dye) made either on silicon or on glass wafers. Secondly, in the case of RH640 on silicon, there are obviously periodic orbits which sustain the lasing modes, but their lengths are longer than the Fabry-Perot orbit. These are additional arguments that the observed orbits can have reflections from top and bottom microlasers facets. As the refractive index of silicon is 4, more complicated orbits can have total internal reflections at the interface polymer-air, and thus lower loss and consequently smaller thresholds.

The issue of threshold estimation in two-dimensional microlasers was considered in the work [109]. It can be described by the following equation:

$$re^{g_{th}L} = 1 \quad (4.4)$$

where g_{th} is the value of the linear gain coefficient which is necessary to compensate the losses, L – periodic orbit length, and r – the total reflection coefficient in intensity. For a Fabry-Perot orbit, $L=2w$ where w is the width of the laser, and:

$$r = \mathbf{R}^2 \quad (4.5)$$

where

$$\mathbf{R} = \left(\frac{n_2 - n_1}{n_2 + n_1} \right)^2 \quad (4.6)$$

is the Fresnel reflection coefficient at normal incidence at the interface of the two media with refractive indices n_1 and n_2 .

Using equation 4.4, it is possible to estimate the thresholds for periodic orbits of different shapes. It was found that microlaser emission is TE-polarized, which means that its polarization is parallel to the X-axis, and it is s-polarized for all the reflections in the Y-Z plane. That is why reflection coefficient \mathbf{R} was calculated as:

$$\mathbf{R} = \frac{\sin^2(\alpha - \beta)}{\sin^2(\alpha + \beta)} \quad (4.7)$$

where α is the angle of incidence of the light onto the interface, β – angle of refraction

or:

$$r = \frac{n \cos i - \sqrt{n_1^2 - n^2 \sin^2 i}}{n \cos i + \sqrt{n_1^2 - n^2 \sin^2 i}} \quad (4.8)$$

where \mathbf{n} – the refractive index of the polymer, \mathbf{n}_1 – the refractive index of the medium (air, silicon or glass), \mathbf{i} – angle of incidence.

Schematic explanations of the periodic orbits which are considered are given on the figures 4.22 and 4.23. Figure 4.22 explains that we consider orbits in the Y-Z plane only. This cross-section in the Y-Z plane is a rectangle. The simplest Fabry-Perot periodic orbit is indicated as a red arrow on the Figure 4.12. Due to the significant length of the microlaser along X and the optical traps, it is most probable that orbits can't have any reflections in the X direction, i.e. all considered orbits lie in the y-z plane.

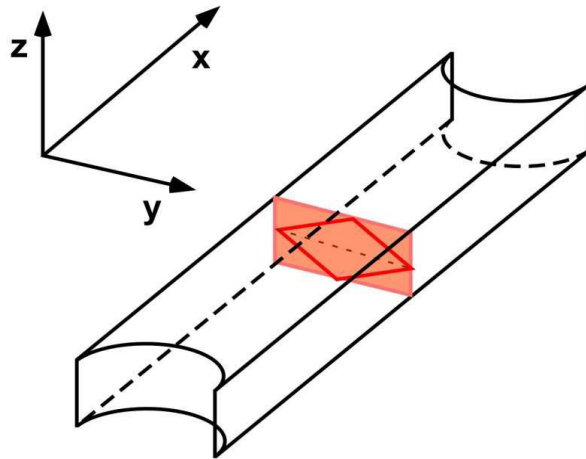


Figure 4.22 — Schematic image of a three-dimensional Fabry-Perot, not at scale. The red rectangle indicates the Y-Z plane, where plane orbits are expected to appear.

For convenience, we introduce the notation (y, z) , where \mathbf{y} is the number of reflections on each horizontal facets and \mathbf{z} – on each vertical wall. It is clear that we can have only the same number of reflections from the each vertical wall or from the each horizontal facet. In the case of different number of reflections for each pair, we should observe non-symmetrical orbit. This orbit must have some angles of incidence not equal to corresponding angle of reflection, which is not possible.

At first, orbits with one reflection on each vertical wall and different amount of reflections on the horizontal facets (1-5) are considered (see fig. 4.23). They are referred to as (1, 1), (2, 1), (3, 1), (4, 1) and (5, 1) orbits, respectively. The reflection coefficient \mathbf{r} was calculated according to equations (4.5) and (4.6) for each case. For example, for the simple diamond orbit (see orbit (1, 1) on the figure 23) it was necessary to take into account one reflection from the top face, one from the bottom and one from each vertical wall. In this case $\mathbf{R} = \mathbf{r}_{\text{top}}\mathbf{r}_{\text{bottom}}\mathbf{r}_{\text{wall}}^2$. Generally equation for \mathbf{R} calculation takes the form:

$$\mathbf{R} = \mathbf{r}_{\text{top}}^y \mathbf{r}_{\text{bottom}}^y \mathbf{r}_{\text{wall}}^{2z} \quad (4.9)$$

Coefficient \mathbf{r} was calculated with equation (4.8). The angle of incidence \mathbf{i} depends on the shape of the orbit and of the dimensions of the microlaser.

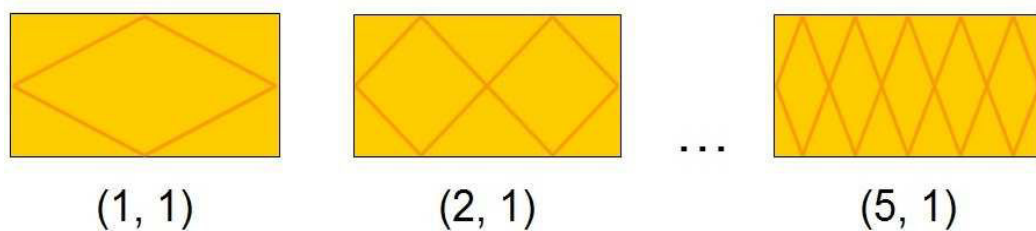


Fig. 4.23. Schemes of different periodic orbits in the Y-Z plane, with a single reflection on each vertical wall

Knowing \mathbf{R} it is possible to find \mathbf{g}_{th} using equation (4.4). In the figure 4.24, thresholds values are presented for microlasers with different widths for the periodic orbits (1, 1), (2, 1), (3, 1), (4, 1) and (5, 1). As the wafer material silicon with $n = 4$ was used. In fact we use silicon wafer with a 2 μm thick silica layer. As the refractive index of silica is very close to that of the polymer, it was estimated by Stefan Bittner that this silica layer can be neglected in the calculations, considering that the actual reflection occurs in fact at the silica-silicon interface.

For comparison, the calculated threshold for Fabry-Perot orbits (0,1) was added on the graph. The height of the microlasers was about 25 μm .

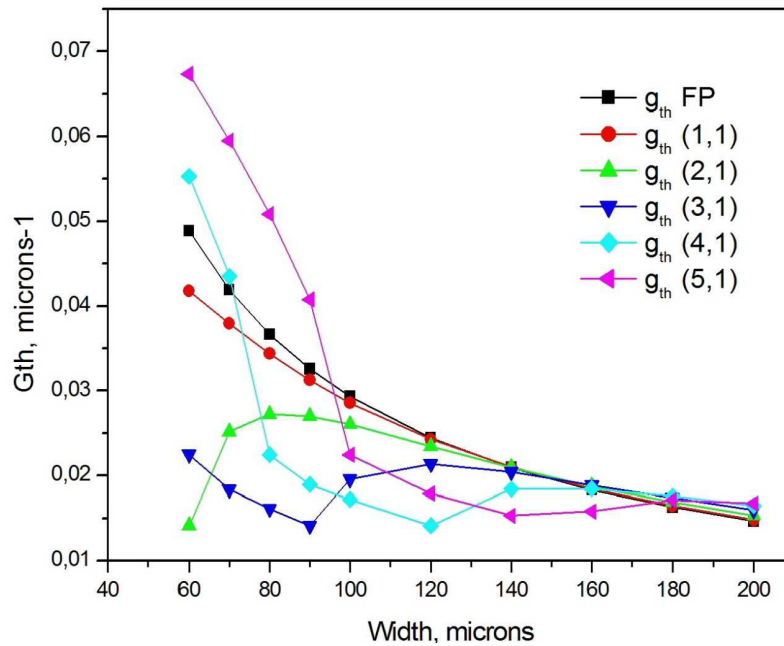


Figure 4.24 — Threshold values (calculated data) for microlasers with various widths for periodic orbits with different number of reflections (1-5) at the horizontal facets (Rhod 640, $n=1.64$, on silicon)

Due to the significant differences in the spectra for the microlasers on the silicon and on the glass it has sense to carry out the same threshold's estimations for the glass wafer. Graphically these calculations are presented on the figure 4.25. For the glass refractive index $n = 1.5$ was used. The thresholds are roughly higher than in Fig. 4.24, since the polymer and the glass have very close refractive indices.

We see that in the case of the glass wafer Fabry-Perot orbit has one of the lowest thresholds for the all considered widths that agrees well with the experimental data. For the silicon wafer, as expected, orbits with more complicated shapes have lower thresholds.

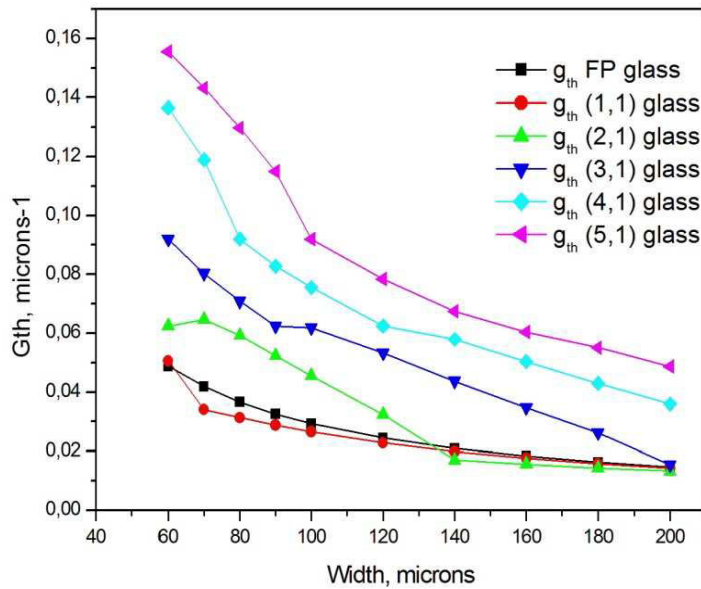


Figure 4.25 — Threshold values (calculated data) for microlasers with various widths for PO with different number of reflections (1-5) at the horizontal facets (Rhod 640, on glass)

The optical lengths are calculated for these periodic orbits considering RH640 and compared to experimental data with RH640 on silicon in the table 4.4.

Table 4.4 — Calculated optical lengths for different orbits (Rhodamine 640, on silicon) for different orbits and experimental results (L_{opt1}). Calculated values that have a good correspondence to the experimental data are bolded

Width	$L_{opt}(1, 1)$	$L_{opt}(2, 1)$	$L_{opt}(3,1)$	$L_{opt}(4, 1)$	$L_{opt}(5, 1)$	L_{opt1}	L_{FP}
60	213	256	315	382	454	274	196
70	243	282	336	400	469	307	229
80	274	309	359	420	486	340	262
90	306	337	384	441	505	409	295
100	338	366	410	463	525	440	328
120	402	426	464	512	568	560	393
140	466	487	520	564	615	615	459
160	531	549	579	618	665	665	524
180	596	612	639	675	718	611	590
200	661	676	700	733	773	683	656

Graphically data from the table 4.4 are represented on the figure 4.26.

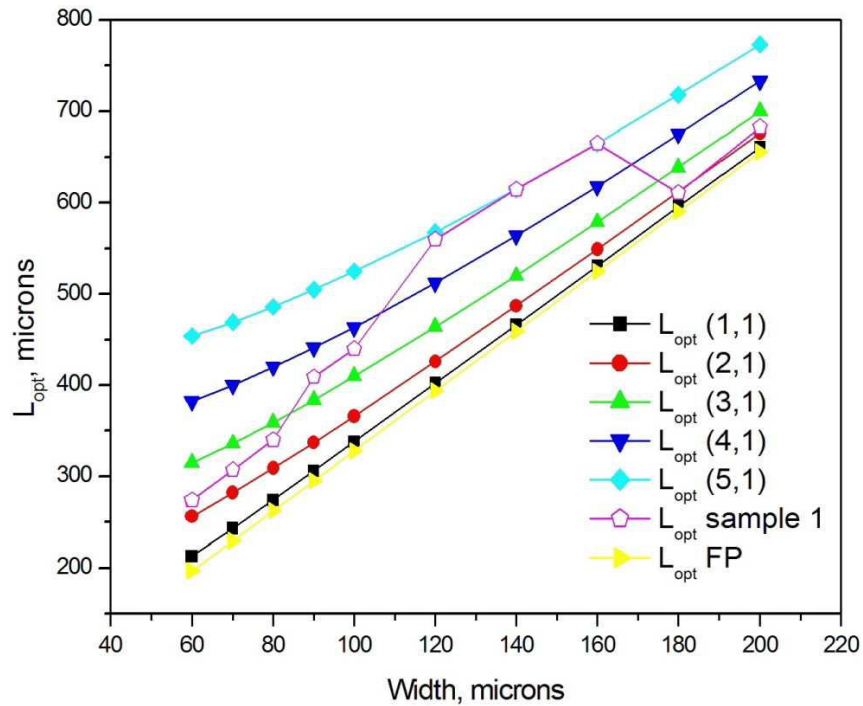


Figure 4.26 — Optical length values for periodic orbits in microlasers with different widths:

$L_{opt} (1, 1)..(5, 1)$ – calculated values for PO with different number of reflections at the horizontal facets and with a single reflection on the vertical walls (Rhodamine 640, on silicon, $n=1.64$), $L_{opt} \text{ sample 1}$ – experimental data for microlasers on silicon wafer (Rhodamine 640), $L_{opt} \text{ FP}$ – calculated for Fabry-Perot orbit (0,1)

Comparing data from the table 4.4 we see almost complete coincidence of the optical length values for the microlasers with the width 120, 140 and 160 microns in the case of the orbit (5, 1). From the figure 4.24, it follows that exactly for these widths this periodic orbit has one of the lowest thresholds which confirms the validity of our assumptions. For instance, for the Fabry-Perot microcavity with the width 140 μm and the height 25 μm , the lowest threshold among the considered periodic orbits is the orbit (5, 1). The calculated optical length for this PO with $n_g = 1.64$ is 615 μm and the experimental ones are 615 μm and 600 μm respectively for the samples 1 and 2 on a silicon wafer. Moreover the Fabry-Perot orbit has the lowest threshold only in the case of 180 and 200 μm widths and only in these cases the observed optical length value is closest to the optical length of the Fabry-Perot orbit.

However for microlasers with a width smaller than 100 μm , possible orbits are still not identified. Due to this, some additional estimations were carried out. More complicated shapes of the periodic orbits with the 2 reflections from the each wall and 1-7 reflections from each of the horizontal facets were considered. Calculations were performed using the same method presented above using the equations (4.4) – (4.9). Results are presented on figure 4.27.

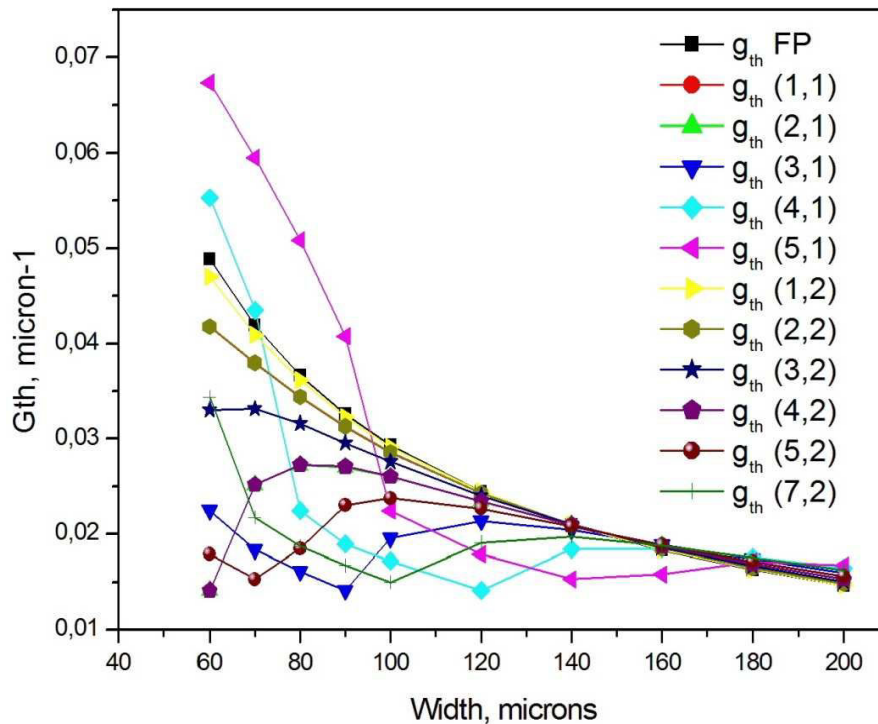


Figure 4.27 — Estimated threshold values for microlasers with various widths for further periodic orbits with 1-5 reflections at the horizontal facets and 1-2 reflections at the vertical walls (Rhodamine 640, on silicon)

Table 4.5 gathers the calculated optical lengths for all the considered periodic orbits with two reflections at the vertical walls. For comparison, experimental data for the sample 1 (L_{opt1} from Table 2) on silicon are added. In this case, it appears that for some specific widths the agreement is quite good, but the optical length must be multiplied by 2. Data from the table 4.5 are plotted on the graph 4.28.

Table 4.5 — Calculated optical lengths for different orbits (Rhodamine 640, on silicon) for different orbits and experimental results ($L_{opt1} * 2$). Calculated values that have a good correspondence to the experimental data are bolded

Width	$L_{opt} (1, 2)$	$L_{opt}(2, 2)$	$L_{opt} (3, 2)$	$L_{opt} (4, 2)$	$L_{opt} (5, 2)$	$L_{opt} (7,2)$	$L_{opt1} * 2$	L_{FP}
60	402	426	464	512	568	695	548	196
70	466	487	520	564	615	735	614	229
80	531	549	579	618	665	777	680	262
90	596	612	639	675	718	823	818	295
100	661	676	700	733	773	871	880	328
120	791	804	824	852	887	974	1120	393
140	922	932	950	975	1005	1083	1230	459
160	1052	1062	1078	1099	1126	1196	1330	524
180	1183	1192	1206	1225	1249	1312	1222	590
200	1314	1322	1334	1352	1374	1432	1366	656

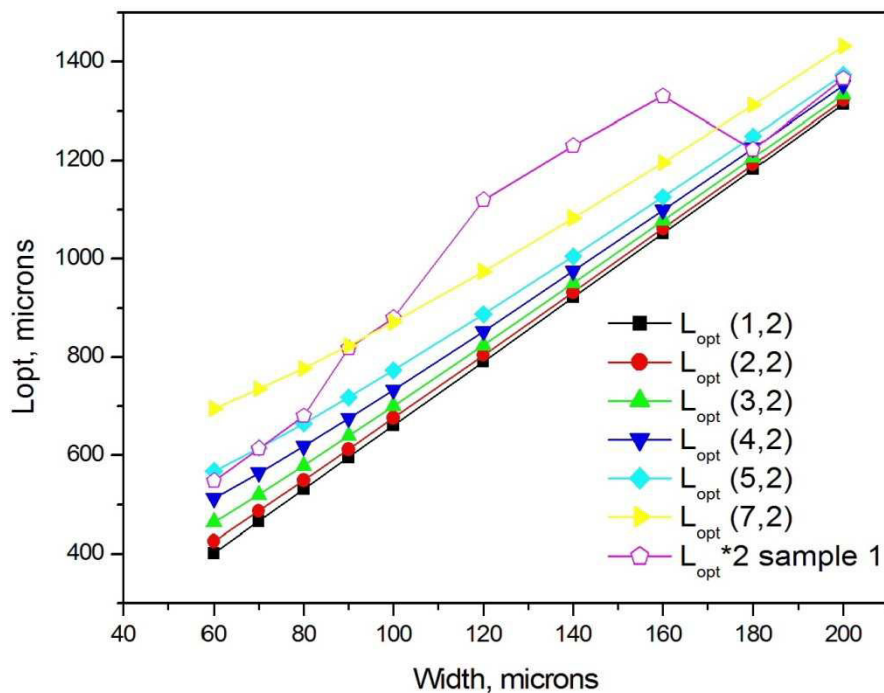


Figure 4.28 — Calculated optical length for periodic orbits in microlasers of different widths.

$L_{opt} (1, 1)..(7, 2)$ – calculated values for PO with different number of reflections at the horizontal facets and with two reflections at the vertical walls (Rhodamine 640, on silicon),
 $L_{opt} * 2$ sample1 – experimental data for microlasers on silicon wafer. The experimental optical lengths are multiplied by two (Rhodamine 640)

For the microlasers with the widths 60, 70 and 80 microns there is a good correspondence of the calculated and experimental optical lengths for the orbit (5, 2) and for microlasers with the widths 90 and 100 microns for the orbit (7, 2).

For example, for the width 100 μm the periodic orbit (7, 2) has the lowest threshold. Calculated optical length for this orbit is 871 μm ($n_g = 1.64$), obtained from the samples 1 and 2 - 876 μm and 880 μm , respectively.

For microlaser with the width 90 μm the best correspondence between the optical lengths is also observed for the orbit (7, 2): 823 μm is the calculated value, 818 μm and 794 μm are the experimental values for the samples 1 and 2 respectively. But the lowest calculated threshold g_{th} for this width corresponds to the orbit (3, 1). Optical length for this orbit is 384 μm or 768 μm (considering doubling). However it should be noted that the threshold value for the orbit (7, 2) for this width is also one of the lowest.

Chapter 4 conclusions

In this chapter periodic orbits in three-dimensional microlasers with the simplest forms were investigated. It was clearly identified that all observed periodic orbit in the cuboid microlasers with a square cross-section is two-dimensional (2D diamond orbit). As a consequence, we demonstrated a method to calibrate the refractive index. The refractive index of the material can be carried out from the cuboid spectra's treatment and is then used to analyze spectra from other microlaser shapes.

For the Fabry-Perot microlasers, the situation is not so obvious, against expectations. It was found that most part of observed orbits does not corresponds to the simplest Fabry-Perot orbit. It was shown that orbits with more complicated shapes (orbits reflections from the lateral, top and bottom facets) can exist. Calculations confirm that in general these orbits have lower thresholds than Fabry-Perot. It is the case in particular using silicon wafers. In general the predicted optical lengths have a good agreement with the experimental data obtained from Fourier transforms of the spectra.

Unfortunately, further investigations have shown that the calibration of the refractive index from cuboid spectra is not precise enough. For example, for some first samples (with RH640) the average refractive index obtained from cuboids measurements was $n = 1.7$ (not 1.64). It looks like from solution to solution and from sample to sample we can observe not significant variation in the refractive index value.

The figure 4.29 represents the generalization of the analysis of the possible periodic orbits in Fabry-Perot microlasers doped by Rhodamine 640 on a silicon substrate. Few dependences of the optical lengths on microlasers' width are shown: black line with the empty symbols – experimental data (Sample 1, see Table 2, column 2), other color lines – the most probable periodic orbit (see fig. 4.26 and 4.28) (5, 2), (7, 2), (5, 1), (2,1) and Fabry-Perot orbit. To simplify the comparison, the optical lengths of orbits with two reflections on the vertical facets ((7, 2) and (5, 2)) were divided by 2.

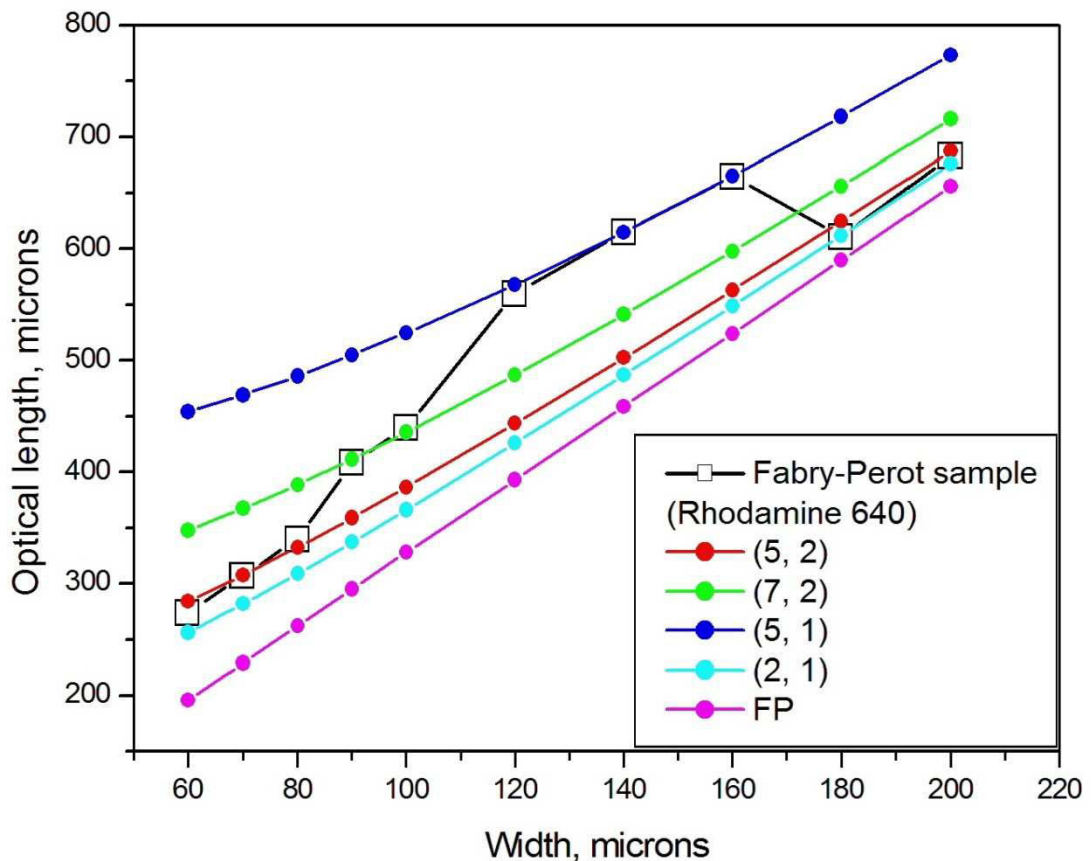


Figure 4.29 — Optical lengths versus microlaser widths for sample 1 on silicon (experimental data) and calculated data for orbits (5,2), (7,2), (5,1), (2,1) and Fabry-Perot orbit, with $n=1.64$. For the orbits (5,2) and (7,2), the optical lengths were divided by two

It is clear, that due to the uncertainty in the refractive index value, it is not possible in some cases to identify the lasing periodic orbit. For example, for the width 180 and 200 microns for the refractive index value $n=1.64$, the best correspondence for the orbit (2, 1) is observed, not for the expected Fabry-Perot periodic orbit. The orbit (5, 2) also has a calculated optical length very close to the experimental one inferred from the Fourier transform of the spectra. According to the calculations presented on the figure 4.27, threshold values of orbits (2,1) and (5,2) for these widths are almost equal. So, on this stage of the research it is not possible to draw a conclusion regarding the lasing periodic orbit with a dead certainty.

In fact in the case of three-dimensional Fabry-Perot microlasers, we considered periodic orbits in the plane of a two-dimensional rectangle (see figures 4.12 and 4.22). Coming from such a point of view, we can obtain other evidences by investigating periodic orbits in flat rectangular-shaped microlasers. This work on rectangular two-dimensional microlasers with different ratios was performed by master students of LPQM, Alister Trabattoni and Paul Hilaire, after my leave. The agreement with periodic orbits in 3D Fabry-Perot seems quite good and a publication is under writing.

CHAPTER 5. LUMINESCENT RARE EARTH OXIDE NANOPARTICLES

This chapter studies in detail the fabrication of rare earth oxide nanoparticles. Two types of synthesis methods are considered: standard high temperature decomposition of Er and Yb chlorids, as well as low temperature synthesis in an anhydrous alcoholic medium. Luminescence characteristics of fabricated materials are compared and their nano dimension is confirmed. The possibility of creating a transparent luminescent composite material based on the acrylic monomer matrix and synthesized nanoparticles is studied.

5.1 Materials

For the synthesis of nanoparticles and fabrication of nanocomposites the following substances and methods were used.

1) Chlorids of Er and Yb, as well as silica nanoparticles (diameter 14nm) were used as the raw material for the syntheses. The simplest trihydric alcohol, glycerol, was chosen as an anhydrous alcoholic medium. In the process of synthesis were also used NaOH aqueous solution and 1-butanol as a solvent.

2) Two-component acrylic matrix consisted of BisA/2-Car in 1:1 mass percentage was chosen for fabrication of the polymer nanocomposite. 2,2-dimethoxy-2-phenylacetophenone (In II) was the photoinitiator of polymerization. For a more detailed information about materials used in the study, see Annex A.

5.2 Synthesis of nanoparticles

Chapter 1 contains review of different nanoparticles synthesis methods and the problems arising when high temperatures are used in at least one of the stages of the synthesis.

Further we consider the technologies of four syntheses conducted within this study. I — low temperature synthesis of Er and Yb oxide nanoparticles in an anhydrous

alcoholic medium in the presence of silica nanoparticles. II — high temperature synthesis of Er and Yb oxide nanoparticles in an anhydrous alcoholic medium in the presence of silica nanoparticles. III — low temperature synthesis of Er and Yb oxide nanoparticles in an anhydrous alcoholic medium. IV — high temperature synthesis of Er and Yb oxide nanoparticles. All technological stages were completed in the chemistry lab at the Department of Photonics Engineering.

Glycerol was preannealed at 150°C for 2 hours to remove any residual water in the alcohol.

5.2.1 Syntheses I and II

The mixture of Er and Yb chlorids powders in 1:2 mass percentage was introduced into the heated glycerol in 1:50 mass percentage. The mixture was heated at 100°C for 1 or 2 hours with periodic ultrasonic stirring (with ultrasonic rod disperser) until the powder was visually completely dissolved in glycerol. 1–3ml of the prepared NaOH aqueous solution with molarity 3 mol/L was introduced into glycerol in small portions, with stirring and subsequent heating until the solution became transparent. The alkali was no longer added as soon as the solution ceased to become transparent after heating. Silica nanoparticles were introduced in parts into the homogenized solution in 1:2 mass percentage relative to the rare earth chlorides.

The mixture was incubated at 140°C with periodic stirring for 1 hour. Then the solution was heated at 180°C for 4 hours. After cooling, the solution was repeatedly washed with butanol to remove residual alkali and reaction byproducts (glycerolates). Washing continued until pH 7 was obtained. After precipitation, the solvent was poured off and the precipitate was dried at 50°C.

The dry residue was divided into two equal parts for low temperature synthesis (I) and high temperature synthesis (II).

5.2.1.1 Low temperature synthesis I

The powder obtained as described above was dissolved in glycerol and heated at 250°C for 1 hour. In the initial experiments the particles were not reheated, and

measurements took place immediately after the first stage (at maximum heating temperature of 180°C). However, the luminescence intensity was low, so it was decided to increase the heating temperature in order to enhance the conversion from hydroxide to oxide. The boiling point of glycerol is 290°C, so the temperature of 250°C was chosen as optimal. Synthesis was conducted in the closed heat-resistant bottle whose cover was not fully ground-in. This prevented the intense evaporation of glycerol, and at the same time provided a low vapor pressure inside the bottle. Presumably, during the low temperature synthesis the following chemical reactions took place:



For further studies the nanoparticles either remained in the glycerol solution or were repeatedly washed with butanol, dried and introduced into the polymer matrix.

5.2.1.2 High temperature synthesis II

The powder obtained as described above was heated at 700°C for 1 hour in the muffle furnace, and then cooled to room temperature.

5.2.2 Synthesis III and IV

The main difference of the second series of syntheses was the absence of silica nanoparticles on any technological stage of synthesis. The technology itself is similar to the described above technology of syntheses I and II.

1) The mixture of Er and Yb chlorids in 1:2 mass percentage was dissolved in the preheated glycerol (in 1:50 mass percentage) by heating at 100°C and periodic ultrasonic stirring for 1 or 1.5 hours;

2) 1–3ml of the NaOH aqueous solution with molarity 3 mol/L was introduced into glycerol solution;

3) The mixture was heated at 140°C for 1 hour;

4) The mixture was heated at 180°C for 4 hours;

5) After cooling, the solution was repeatedly washed with butanol to remove residual alkali and reaction byproducts;

6) The solution was dried in a thermostat at 50°C until the solvent was completely evaporated.

These preliminary stages are the same for low temperature synthesis (III) and for high temperature synthesis (IV). Low temperature synthesis III is identical from the technical point of view to the second stage of synthesis I, while high temperature synthesis IV is identical to the second stage of synthesis II.

5.3 Introduction of nanoparticles into polymer matrix

Composite made up of Bis A and 2-Car (in 1:1 mass percentage) was chosen as the polymer matrix. Properties of these monomers and features of the monomer compositions fabrication were considered in subparagraph 2.2.1 and in [110–112].

Rare earth oxide particles synthesized by all four methods were introduced directly into the mixture of acrylic monomers. Their mass concentration was in all cases about 0.5%. Particles dissolved poorly, so to improve the dissolution the repeated heating at moderate temperatures (40–50°C) and ultrasonic stirring were used. After the nanoparticles were visually completely dissolved, the photoinitiator of polymerization was introduced into the monomer mixture. 2,2-dimethoxy-2-phenyl-acetophenone was used as the photoinitiator in 0.2% mass concentration. The absorption spectrum of the photoinitiator is shown in figure 2.7.

The fabricated homogeneous composite was then used in production of solid polymer films. The drop of monomer mixture was placed between the two lavesan films (the thickness of films was 100µm) and was exposed for 5–10 minutes. The mercury-vapor lamp as the source of UV radiation was used. As a result of this UV curing, a solid transparent nanocomposite in the form of a polymer film was produced.

5.4 Study of synthesized nanoparticles

The studies of luminescence of the synthesized nanoparticles were conducted on the laser scanning microscope Zeiss LSM-710 (with the assistance of A. V. Veniaminov) with 3nm step/shift. Measurements were carried out with glycerol solution of nanoparticles (low-temperature syntheses), dry powder (high-temperature syntheses) and solid polymer films (for polymer composites). The drop of solution or some amount of the dry powder were placed on the glass substrate and after placed on the microscope stage. The 488nm wavelength source of radiation was mainly used for pumping. Photomicrographs of solutions, powders and films under investigation were also made by Zeiss LSM-710. Figure 5.1 shows photo of luminescent glycerol solution of nanoparticles (synthesis I).

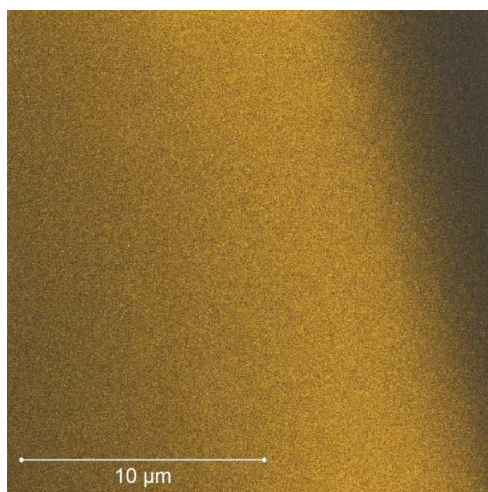


Figure 5.1 — Photo of luminescent glycerol solution of Er and Yb oxide nanoparticles, obtained by low temperature synthesis in the presence of silica nanoparticles (synthesis I); pumping wavelength is 458nm

Low dimensionality of particles and uniform luminescence throughout the entire volume of the solution are observed. This proves the nano dimension of the synthesized Er and Yb oxide particles, and the absence of agglomerations of particles in the case of low temperature synthesis. The glycerol solution of nanoparticles obtained by low temperature synthesis III is also homogeneous.

Different results were found when nanoparticles obtained by high temperature syntheses II and IV were studied. Figures 5.2 and 5.3 show fragments of powders under

investigation. Figure 5.2 shows the result of synthesis II (in the presence of silica nanoparticles), while figure 5.3 shows the result of synthesis IV (without silica nanoparticles). The powders do not seem homogeneous throughout the entire volume. The presence of different aggregates and the larger size of particles should be noted. The following spectra (for high temperature syntheses, curve 1 on the figure 5.7 and curve on the figure 5.8) were recorded at the areas of the most intense luminescence. At the other areas of powder, the luminescence intensity is lower or even zero.

The results of all four methods of syntheses were then subjected to the spectral analysis. Spectrum in figure 5.4 was obtained by measuring luminescence from glycerol solution of rare earth oxide nanoparticles with silica nanoparticles (synthesis I). Wavelength of maximum luminescence is about 555nm.

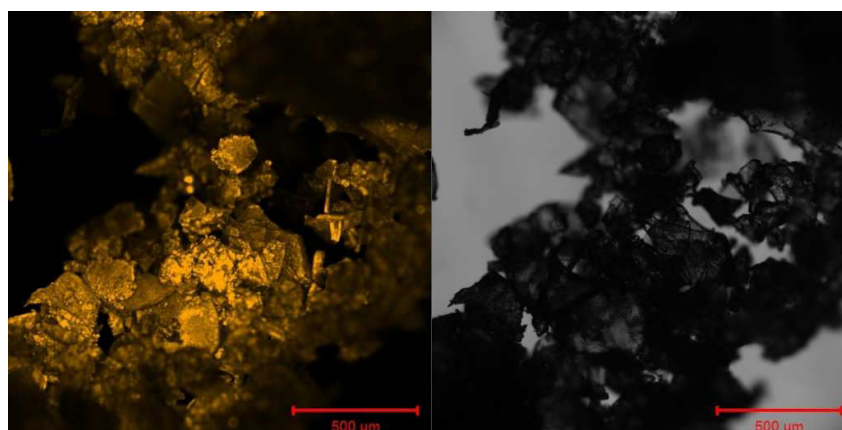


Figure 5.2 — Luminescence of Er and Yb oxide nanoparticles powder, obtained by high temperature synthesis in the presence of silica nanoparticles (synthesis II). Left: luminescent powder (pumping wavelength = 488nm). Right: no pumping

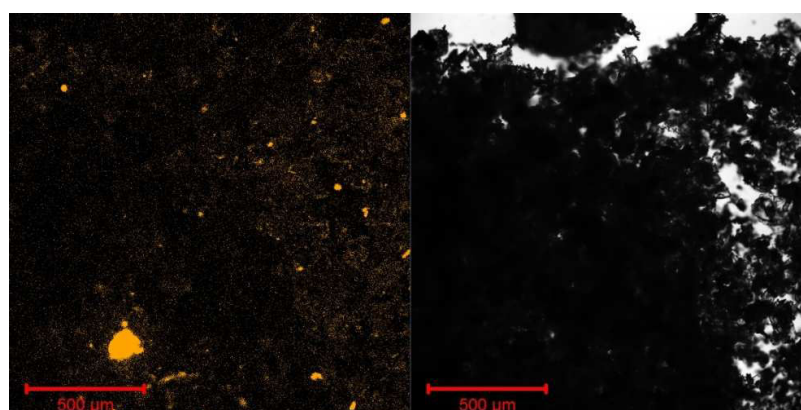


Figure 5.3 — Luminescence of Er and Yb oxide nanoparticles powder, obtained by high temperature synthesis without silica nanoparticles (synthesis IV). Left: luminescent powder (pumping wavelength = 488nm). Right: no pumping

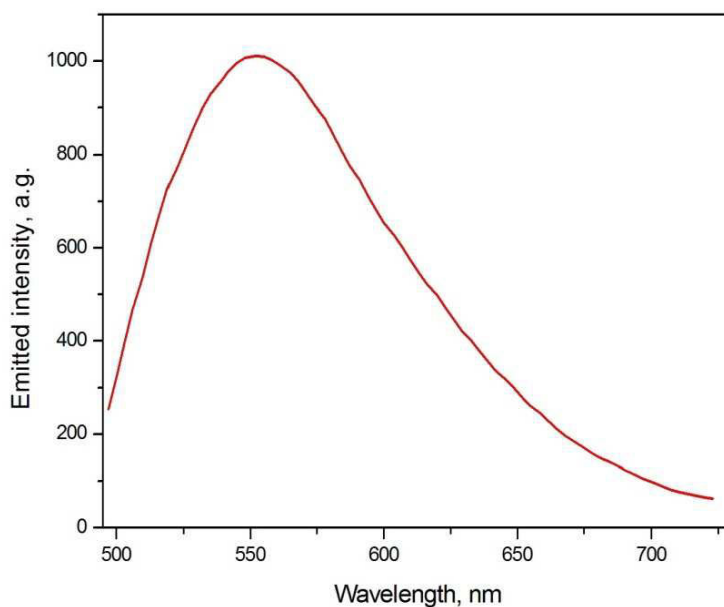


Figure 5.4 — Luminescence spectrum of Er and Yb oxide nanoparticles, obtained by low temperature synthesis in the presence of silica nanoparticles (synthesis I, nanoparticles in glycerol)

Figure 5.5 shows the energy level diagram of trivalent erbium ion [70].

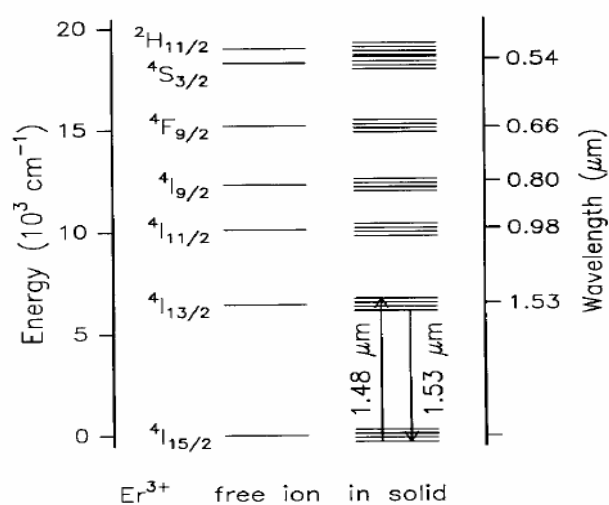


Figure 5.5 — Energy level diagram of Er^{3+} ion [70]

Based on this diagram, it can be concluded that the observed radiation corresponds to the energy level transition ${}^4\text{S}_{3/2} \rightarrow {}^4\text{I}_{15/2}$ (540nm maximum).

Due to the broadening of the spectrum, it is problematic to uniquely identify all of the observed optical transitions. Possibly there is also the ${}^2\text{H}_{11/2} \rightarrow {}^4\text{I}_{15/2}$ transition

(540nm maximum). Some intensity at the right end of the spectrum may indicate the ${}^4F_{9/2} \rightarrow {}^4I_{15/2}$ transition (660nm maximum).

For reference, figure 5.6 [86] shows spectra of yttrium oxide nanoparticles doped with Er and Yb. These nanoparticles were obtained by high temperature synthesis from polymeric precursor.

The shape and position of the peak of the spectrum are typical for all solutions and powders synthesized by all four methods. For reference, figure 5.7 shows spectra of nanoparticles obtained by low and high temperature syntheses with the presence of silica nanoparticles (syntheses I and II, curves 1 and 2 correspondingly). Figure 5.8 shows analogous pair of spectra for syntheses without silica nanoparticles (syntheses III and IV). In each pair, measurements were carried out at the same pump energy.

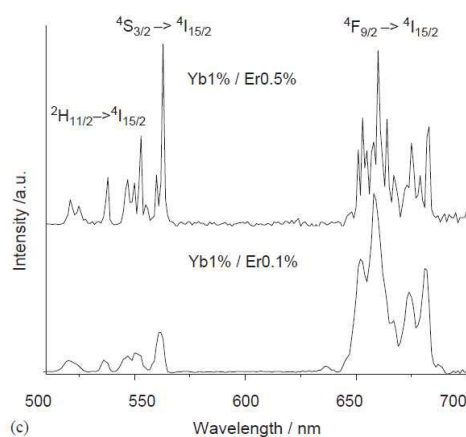


Figure 5.6 — Luminescence spectra of yttrium oxide nanoparticles doped with Er and Yb ions for different concentrations of Er and Yb [86]

It follows from the obtained spectra that luminescence intensity is higher for particles obtained by high temperature synthesis, than for particles obtained by low temperature synthesis. However, this may be explained by the fact that powders obtained using muffle furnace (syntheses II and IV) are heterogeneous in their structure. So the obtained spectra correspond to powder areas with the maximum of luminescence intensity.

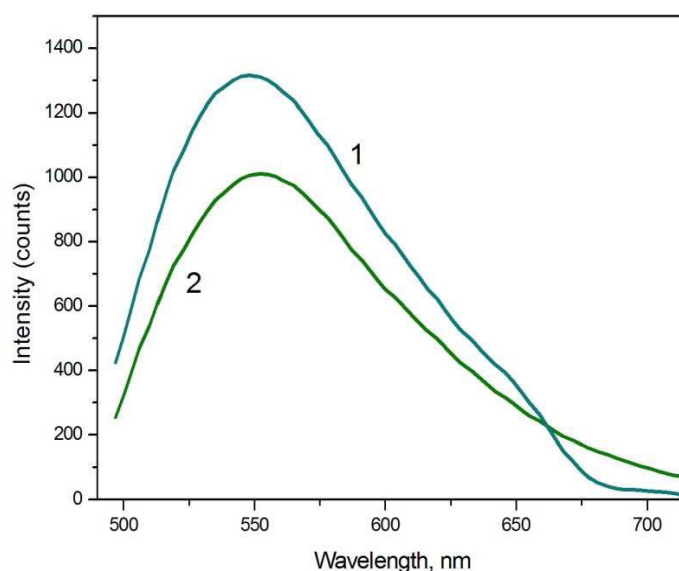


Figure 5.7 — Luminescence spectra of Er and Yb oxide nanoparticles obtained by low and high temperature syntheses in the presence of silica nanoparticles (syntheses I and II). Curve 1: high temperature synthesis. Curve 2: low temperature synthesis. Measurements were carried out at the same pump energy

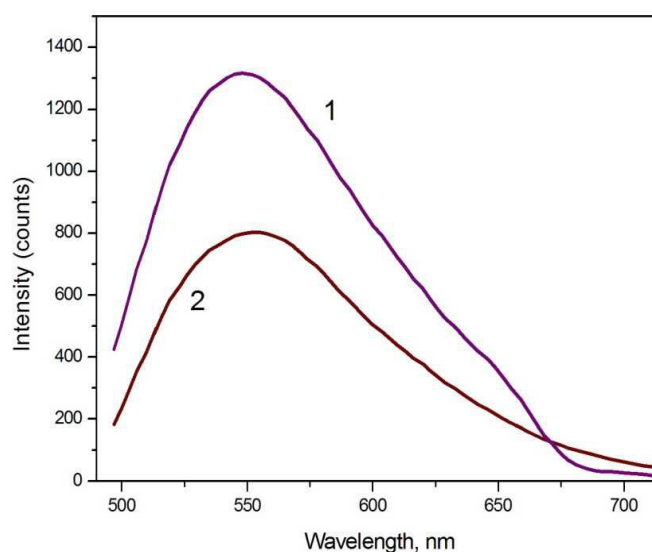


Figure 5.8 — Luminescence spectra of Er and Yb oxide nanoparticles obtained by low and high temperature syntheses without silica nanoparticles (syntheses III and IV). Curve 1: low temperature synthesis. Curve 2: high temperature synthesis. Measurements were carried out at the same pump energy

Figures 5.9 and 5.10 compare syntheses under the same temperature regime depending on the presence or absence of silica nanoparticles. Figure 5.9 shows

luminescence spectra of nanoparticles obtained by syntheses I and III. Figure 5.10 shows luminescence spectra of nanoparticles obtained by syntheses II and IV.

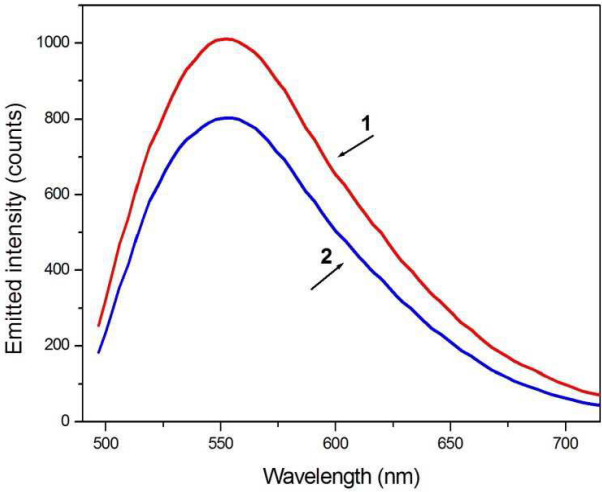


Figure 5.9 — Luminescence spectra of Er and Yb oxide nanoparticles obtained by low temperature synthesis in glycerol in the presence of silica nanoparticles (synthesis I, curve 1) and without silica nanoparticles (synthesis III, curve 2). Measurements were carried out at the same pump energy

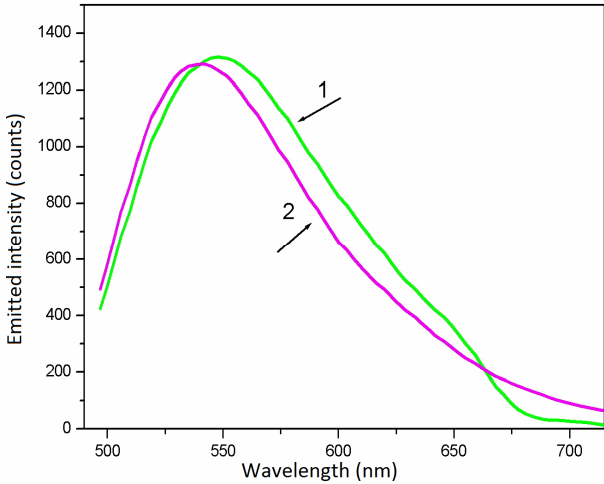


Figure 5.10 — Luminescence spectra of Er and Yb oxide nanoparticles obtained by high temperature synthesis in the presence of silica nanoparticles (synthesis III, curve 1) and without silica nanoparticles (synthesis IV, curve 2). Measurements were carried out at the same pump energy

In both cases the luminescence intensity is higher in the presence of silica nanoparticles. Note also the difference in the position of the maxima in the Er nanoparticles.

luminescence spectra in the presence and without silica nanoparticles. The shift of the maximum luminescence to longer wavelengths in the presence of silica is evident for the powders obtained by high temperature syntheses (II and IV), see figure 5.10.

Changes in the shape of the luminescence spectrum (broadening and shift) in fact are often observed in the nanodimensional systems. This broadening is a consequence of quantum size effects in due to the semiconductor nature of nanoparticles [65].

The broadening is caused by the fact that some ions are close to the surface of the nanoparticle and they are in a modified crystalline field, which shifts their bands. Available energies of transitions are different when ion is located on the surface of the particle or inside its volume. Consequently, the sum of transitions over all nanoparticles provides blurring and broadening of the spectrum.

For example [113] consider broadening and shift of spectrum when the size of particles changes. Figure 5.11 [113] compares the emission spectra of MgS:Eu micro- and nanoparticles. Nanoparticles were obtained from microparticles by pulsed laser deposition with pumping wavelength of 578nm. Spectra are recorded at the temperature of 10K. Broadening of spectrum is also can be explained by the polydispersity of the particles, and the higher the polydispersity is, the greater broadening is [114].

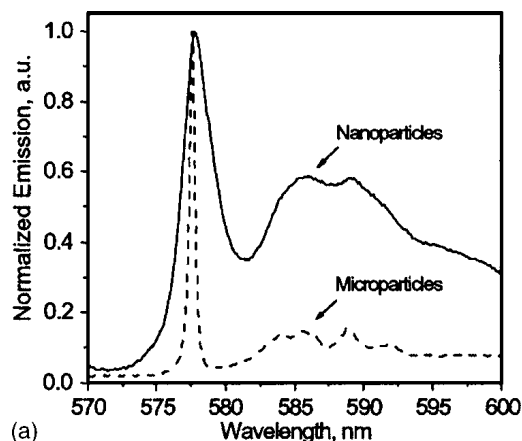


Figure 5.11 — Broadening of nanoparticles spectra: comparison of MgS:Eu micro- and nanoparticles spectra [113]

5.5 Study of nanocomposites

Nanoparticles synthesized by all four methods were introduced into the BisA/2-Car polymer matrix (see section 5.3). The structure of these films is quite homogeneous. Figure 5.12 shows luminescence fragment of the film based on the nanoparticles obtained by synthesis I. As in the case of particles in the glycerol solution (figure 5.1), the uniform luminescence throughout the entire volume of the film and the absence of any aggregate are observed.

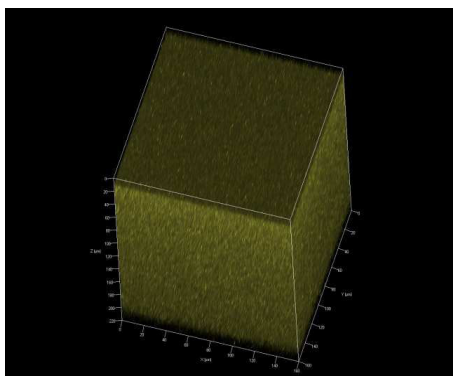


Figure 5.12 — Luminescence of the nanocomposite film obtained by low temperature synthesis I (dimensions of the film are $160 \times 160 \times 200 \mu\text{m}^3$)

Figure 5.13 shows four luminescence spectra corresponding to four films with nanoparticles synthesized by different methods. The highest luminescence's intensity was observed for the film with nanoparticles obtained by low temperature synthesis in the presence of silica nanoparticles (synthesis I). The lowest luminescence corresponded to the film with nanoparticles obtained by high temperature synthesis without silica nanoparticles (synthesis IV).

In all cases, the luminescence intensity reduces when nanoparticles are introduced into polymer. It is caused by not very high concentration of the nanoparticles due to their poor solubility in the polymer composite.

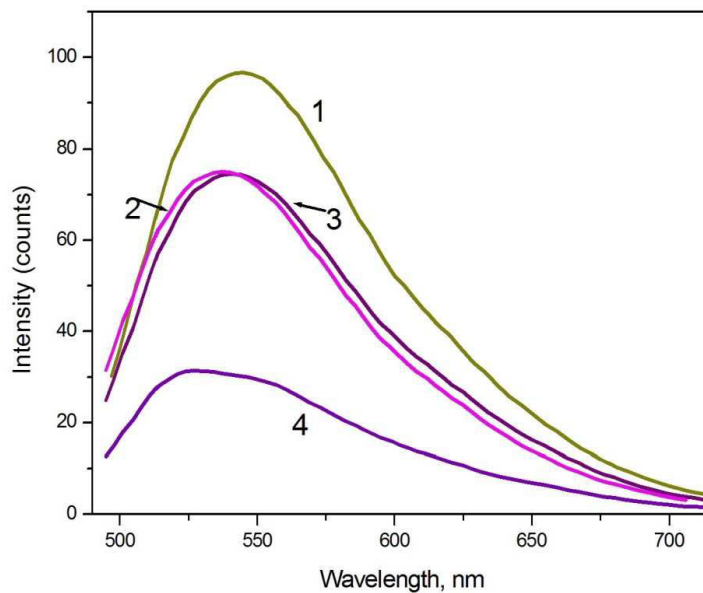


Figure 5.13 — Luminescence spectra of polymer films for four nanocomposites. 1 — low temperature synthesis in the presence of silica nanoparticles (synthesis I); 2 — high temperature synthesis in the presence of silica nanoparticles (synthesis II); 3 — low temperature synthesis without silica nanoparticles (synthesis III); 4 — high temperature synthesis without silica nanoparticles (synthesis IV)

Figure 5.14 compares luminescence spectra of nanoparticles obtained by low temperature synthesis in the presence of silica nanoparticles in glycerol solution (curve 1) and in polymerized nanocomposite (curve 2). Curve 3 is the curve 2 with the intensity multiplied by a factor of 5.

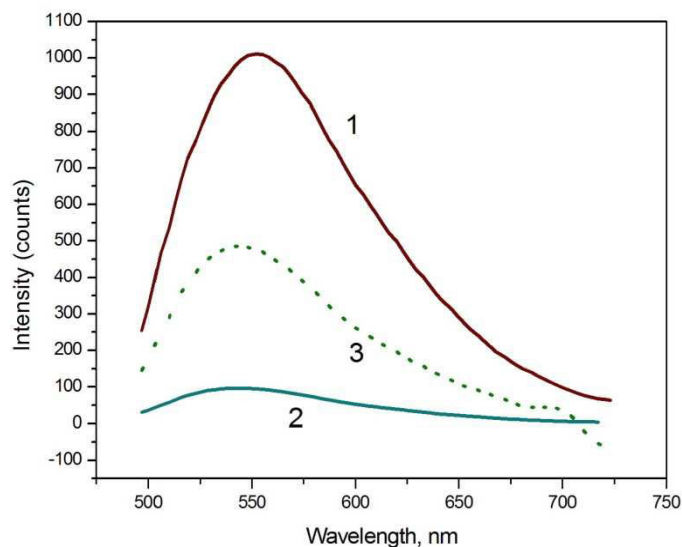


Figure 5.14 — Luminescence spectra of nanoparticles obtained by low temperature synthesis in the presence of silica nanoparticles (synthesis I) in glycerol solution (curve 1) and in solid polymer film (curve 2). Curve 3 is the curve 2 with the intensity multiplied by a factor of 5

5.6 Fabrication of three-dimensional polymer microlasers based on inorganic luminescent nanoparticles

The fabrication technology of three-dimensional organic microlasers by UV lithography (studied previously in Chapter 3) was used to produce a three-dimensional polymeric organic-inorganic microlasers based on luminescent rare earth oxide nanoparticles.

Broadly speaking, the technology is similar to the one considered in subparagraph 3.2.2. Er and Yb oxide nanoparticles obtained by low temperature synthesis I were introduced into the SU-8 2025 photoresist by multiple cycles of stirring using the ultrasonic bath, magnetic stirrer and ultrasonic rod disperser. The mass concentration of nanoparticles was 1% relative to the mass of the polymer in photoresist. The problem of dissolution of nanoparticles in the photoresist should be noted: it took a up to one week for the solution to become homogeneous.

Further technological process included the following stages:

1) Deposition of photoresist doped with nanoparticles on the silicon substrate by spin-coating. Speed is 1000–2000 rpm;

2) Soft bake process: two-stage heating of samples for 3 minutes (at 65°C) and 20–30 minutes (at 95°C). Thickness of the polymer film of the sample after drying was about 25µm;

3) Exposure of the sample using photolithography setup Mask Aligner MJB4 (Suss MicroTec). For exposure the same mask was used as for the fabrication of cubic and Fabry-Perot microlasers in Chapter 4. Exposure time was adjusted manually. The optimal exposure time for the 25µm thick film was 18 seconds;

4) Post-exposure bake involved two-stage heating, for 3 minutes (at 65°C) and for 10 minutes (at 95°C);

5) The development of the sample (10 minutes in the SU-8 developer) and after washing by the isopropyl alcohol.

Two series of samples with nanoparticles obtained by low temperature synthesis in the presence of silica nanoparticles (synthesis I) were fabricated. Two series differ in mass percentage of initial rare earth chlorides relative to silica nanoparticles, 1:2 and

1:20 correspondingly. Figure 5.15 shows microstructures from the first series (mass percentage 1:2), while figure 5.16 shows microstructures from the second series (mass percentage 1:20).

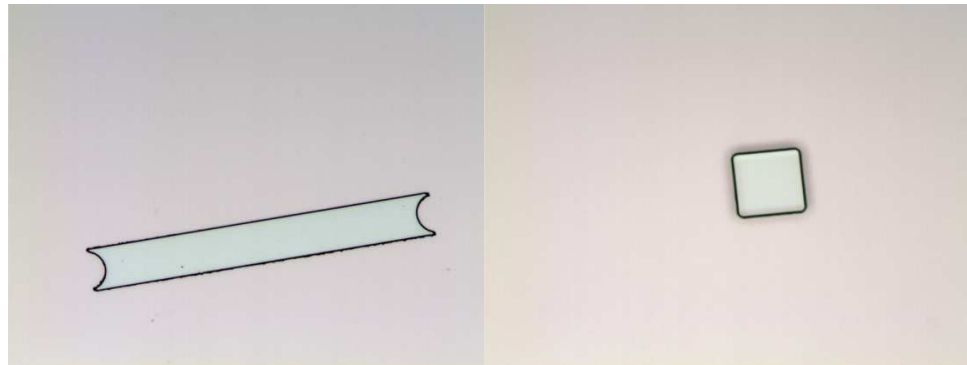


Figure 5.15 — Three-dimensional microresonators based on the SU-8 photoresist and inorganic rare earth oxide nanoparticles (mass percentage of rare earth chlorides relative to silica nanoparticles is 1:2). Photograph was taken through an optical microscope, the height of the structures is 25 μ m. Right: side of the cross section of cuboid is 100 μ m. Left: Fabry–Perot width is 70 μ m

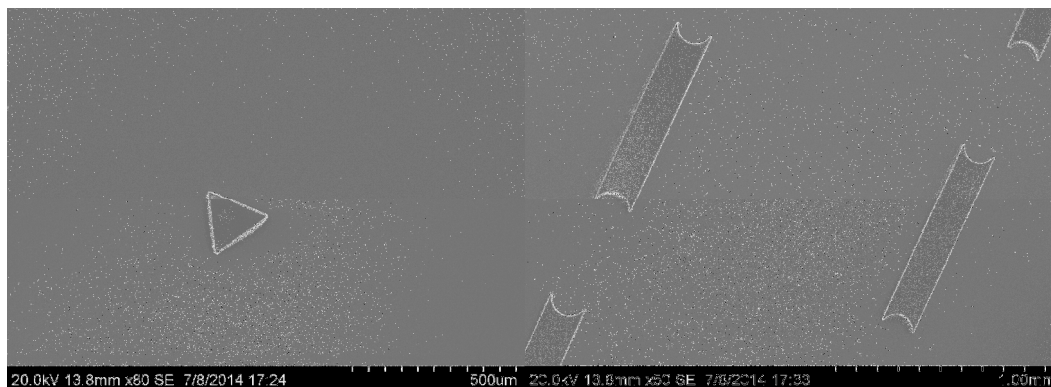


Figure 5.16 — Three-dimensional microresonators based on the SU-8 photoresist and inorganic rare earth oxide nanoparticles (mass percentage of rare earth chlorides relative to silica nanoparticles is 1:20). Photograph was taken through a scanning electron microscope

Note that figures 5.15 and 5.16 show examples of best quality microstructures obtained on the sample. When exposure is correctly chosen, all microlasers have perpendicular/parallel sides. However, unlike microlasers doped with organic dyes, microlasers with nanoparticles often have worse surface quality (figure 5.17). Samples from the first series (Er/Yb mass percentage 1:2) have better surface quality. Most

likely, the deterioration of the smoothness of sides is due to bad dissolution of the nanoparticles in the polymer and possible presence of aggregates.

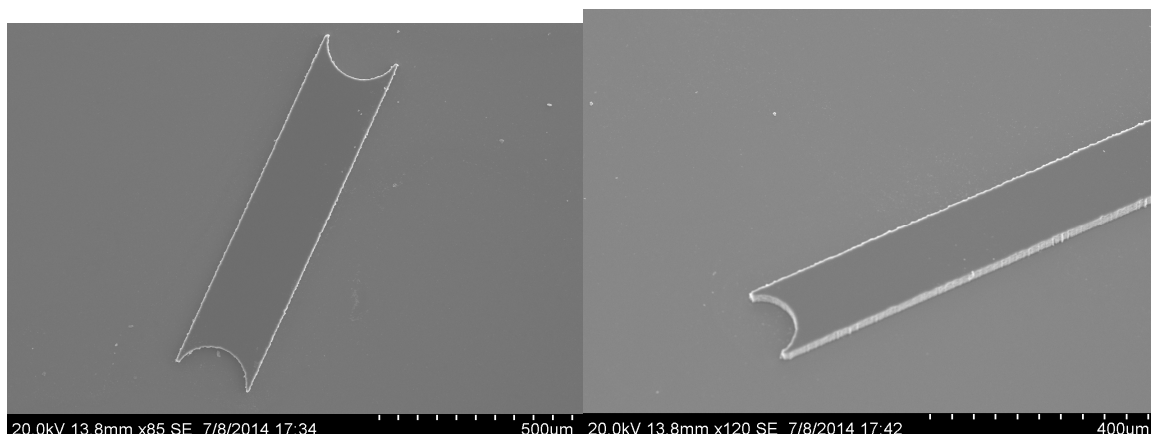


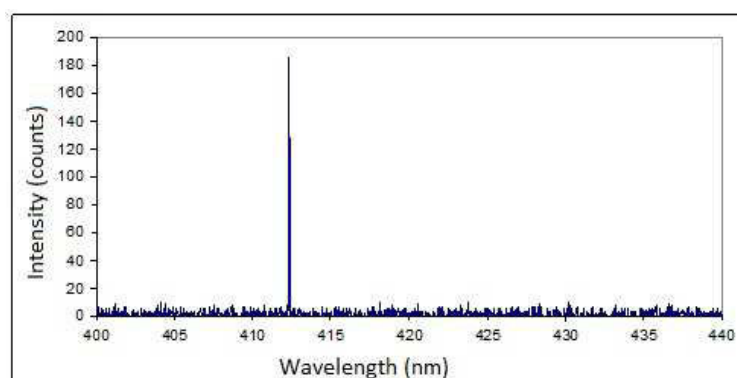
Figure 5.17 — SEM photographs of the microlasers doped with nanoparticles with surface defects (second series of samples, Er/Yb mass percentage 1:2)

Study of the spectral characteristics of both series of samples was performed using the same experimental setup as in the case of organic microresonators (see paragraph 4.1).

In both cases cuboid microlasers and Fabry–Perot microlasers were studied. The intensity of the detected radiation was low, so spectra were recorded at the maximum possible in this operating mode pump energy. This fact does not allow investigating the microresonators in details, to estimate the threshold curve, for example.

For first and second series the results were different.

1) In the first series (Er/Yb mass percentage 1:2) of samples, generation was observed only for microlasers with best surface quality regardless of the size. Figure 5.18 shows laser spectra of two cubic microlasers with sizes of 80µm (top) and 60µm (bottom), and height of 25µm.



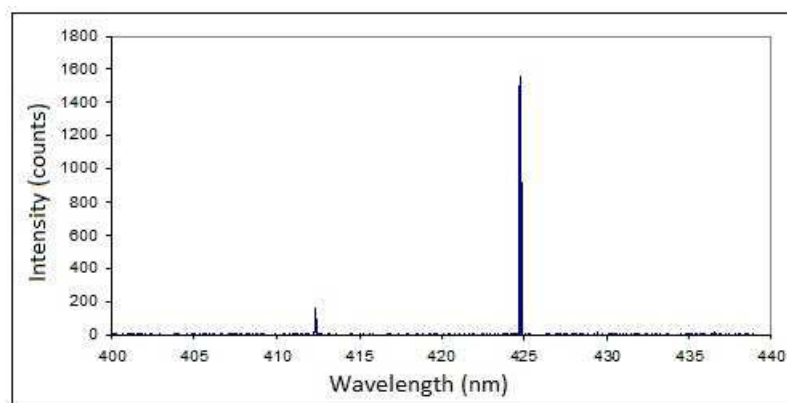


Figure 5.18 — Spectra of cubic microlasers based on the inorganic nanoparticles. Top: cuboid with sizes of $80 \times 80 \times 25 \mu\text{m}$. Bottom: cuboid with sizes of $60 \times 60 \times 25 \mu\text{m}$

2) In the second series (Er/Yb mass percentage 1:20) of samples, there was almost no generation. A very weak signal was obtained from microresonators of maximal size regardless of surface quality.

Chapter 5 conclusions

Studies conducted in chapter 5 show that the proposed and investigated method of low temperature synthesis in an anhydrous medium is an effective way of preparation of low-dimensional luminescent rare earth oxide particles. This method avoids the high temperature heating stage, which is replaced by obtaining nanoparticles in an anhydrous medium at temperatures low enough to convert the hydroxide to oxide. Therefore nanoparticles after the synthesis keep their shape and size, and do not aggregate. Fabricated nanoparticles can be successfully introduced into the polymer matrix and then used in production of three-dimensional organic microresonators. As an active medium these microresonators use inorganic particles, which have higher radiation resistance than organic dyes.

GENERAL CONCLUSIONS

This complex work is dedicated to obtaining and investigation of three-dimensional organic microlasers doped by organic dyes or inorganic luminescent nanoparticles.

First part of the work contains the investigation of self-organization processes in the polymer composites and nanocomposites. Performed research shows that formation of the self-organized elements can be described as a superposition of processes occurring during photopolymerization, including self-focusing of light in a medium with a positive change of the refractive index during photopolymerization and inhibiting effect of oxygen on the photopolymerization. Also the light-induced transfer of inorganic nanoparticles under nanocomposite exposure by periodic wave of light was investigated.

The main part of the work is devoted to obtaining three-dimensional polymer microlasers by UV-lithography. Comparison of the lasing threshold for microcavities obtained by different methods was performed (UV-lithography, two-photon polymerization and structures decoupled from the substrate). Periodic orbits in cuboids microlasers with square cross-section were clearly identified as 2D diamond orbit. It was shown that cuboids spectra analyses can be successful used for refractive index determination. Analysis of Fabry-Perot microlasers spectra shown that spectra shape depends from the type of the dye and the width of microlaser. Subsequent study confirms that orbits with reflections from top and bottom facets can exist. In general, the shape of the orbit depends on the dye, the type of substrate (silicon/silica or glass) and the size of the microlaser (width, height).

The last part of the work contains a study of low-temperature synthesis of luminescent nanoparticles of erbium and ytterbium oxides in an anhydrous medium and polymer composites based on them. Results of low temperature syntheses were compared with the standard high-temperature, absence of any aggregations was shown in the case of new technology. Obtained nanoparticles were successfully introduced in polymer composite and in the SU8 resist. Three dimensional organic microlasers doped by these luminescent nanoparticles were obtained by UV-lithography and investigated.

BIBLIOGRAPHY

1. S. Chenais, S. Forget Recent advances in solid-state organic lasers // *Polymer International*.— 2012.— Vol. 61.— Is. 3.—P. 390–406.
2. Kerry J. Vahala Optical microcavities // *Nature*.—2003.— Vol.424.—P. 839-846
3. B. Gayral, J. M. Gerard, A. Lematre, C. Dupuis, L. Manin, J. L. Pelouard High-Q wet-etched GaAs microdisks containing InAs quantum boxes // *Applied Physics Letters*.— 1999.— Vol. 75.— № 13.—P. 1908-1910.
4. Q. Huang, X. Zhan, Zh. Hou, Q. Chen, H. Xu Polymer photonic-molecule microlaser fabricated by femtosecond laser direct writing // *Optics Communications*.— 2015.— doi:10.1016/j.optcom.2015.08.018
5. S. K. Vanga, A.A. Bettiol Proton beam writing of dye doped polymer microlasers // *Nuclear Instruments and Methods in Physics Research Section B: Beam Interactions with Materials and Atoms*.— 2015.—Vol. 348.— P. 209–212.
6. M. Kuwata-Gonokami, R. H. Jordan, A. Dodabalapur, H. E. Katz, M. L. Schilling, R. E. Slusher, S. Ozawa Polymer microdisk and microring lasers // *Optics Letters*.— Vol. 20.— Is. 20, P. 2093-2095.
7. U. Mohideen, W. S. Hobson, S. J. Pearton, F. Ren, R. E. Slusher GaAs/AlGaAs microdisk lasers // *Applied Physics Letters*.— 1994.— Vol. 64.— №15.—P. 1911-1913.
8. H. Baek, Ch. Lee, K. Chung, G. Yi Epitaxial GaN Microdisk Lasers Grown on Graphene Microdots // *Nano Letters*.—2013.— Vol.13.— №6.— P. 2782–2785.
9. J. Ward, O. Benson WGM microresonators: sensing, lasing and fundamental optics with microspheres // *Laser & Photonics Reviews*.—2011.— Vol. 5.— Is. 4.— P. 553–570.
10. C. Arnaud, M. Boustimi, M. Brenci, P. Feron, M. Ferrari, G. Nunzi Conti, S. Pelli, G. Righini Microsphere laser in Er doped oxide glasses // *Proc. of SPIE* Vol. 5622 .— 2004.— doi: 10.1117/12.589474
11. V. Sandoghdar, F. Treussart, J. Hare, V. Lefèvre-Seguin, J.-M. Raimond, S. Haroche Very low threshold whispering-gallery-mode microsphere laser // *Physical Review*.— 1996.— Vol. 54.— Is. 3.— P. 1777-1780.

12. L. Collot, V. Lefevre-Seguin, M. Brune, J. M. Raimond, S. Haroche Very high-Q whispering-gallery mode resonances observed on fused silica microspheres // *Europhysics letters*.— 1993.— Vol. 23.— Is. 5. — P. 327-334.
13. Li, M., Zhou, X., Ding, Y., Chen, W., Yu, H., Kan, Q., Li, S., Mi, J., Wang, W., Pan, J. A directional-emission 1060-nm GaAs/InGaAs microcylinder laser // *Photonics Technology Letters, IEEE*.— 2015.— Vol.26.— Is.7.— P. 569 – 572.
14. Y. Huang, Sh. Wang, Y. Yang, J. Lin, K. Che, J. Xiao, Y. Du Investigation on multiple-port microcylinder lasers based on coupled modes // *Semiconductor Science and Technology*.— 2010.— Vol.25.— №10.— doi:10.1088/0268-1242/25/10/105005
15. S. Anders, W. Schrenk, E. Gornik, G. Strasser Room-temperature operation of electrically pumped quantum-cascade microcylinder lasers // *Applied Physics Letters*.— 2002.— Vol.80.— №22.— P. 4094–4096.
16. D. K. Armani, T. J. Kippenberg, S. M. Spillane, K. J. Vahala Ultra-high-Q toroid microcavity on a chip // *Nature*.— 2003.— Vol. 421.— P. 925-928.
17. R. Suzuki, T.Kato, T. Tetsumoto, T. Tanabe Octagonal toroid microcavity for mechanically robust optical coupling // *AIP Advances*.— 2015.— Vol. 5.— doi: 10.1063/1.4921201
18. K. D. Heylman, R. H. Goldsmith Photothermal mapping and free-space laser tuning of toroidal optical microcavities // *Applied Physics Letters*.—2013.— Vol. 103.— doi: 10.1063/1.4833539
19. B. D. Jones, M. Oxborrow, V. N. Astratov, M. Hopkinson, A. Tahraoui, M. S. Skolnick, A. M. Fox Splitting and lasing of whispering gallery modes in quantum dot micropillars // *Optics Express*.—2010.— Vol. 18.— Is. 21.— P. 22578-22592.
20. S. Michaelis de Vasconcellos, A. Calvar, A. Dousse, J. Suffczyński, N. Dupuis, A. Lemaître, I. Sagnes, J. Bloch, P. Voisin, P. Senellart Spatial, spectral, and polarization properties of coupled micropillar cavities // *Applied Physics Letters*.— 2011.— Vol. 99.— doi: 10.1063/1.3632111
21. J. Zhu, Ş. K. Özdemir, Y.-F. Xiao, L. Li, L. He, D.-R. Chen, L. Yang On-chip single nanoparticle detection and sizing by mode splitting in an ultrahigh-Q microresonator // *Nature Photonics*.— 2010.— Vol. 4.— P. 46–49.

22. V. Mulloni, L. Pavesi Porous silicon microcavities as optical chemical sensors // *Applied Physics Letters*.— 2000.—Vol. 76. — doi: 10.1063/1.126396
23. L. Jiang, J. Yang, S. Wang, B. Li, M. Wang Fiber Mach–Zehnder interferometer based on microcavities for high-temperature sensing with high sensitivity // *Optics Letters*.— 2011.—Vol. 36.— Is. 19.— P. 3753-3755.
24. G.Huang, V. A. Bolanos Quinones, F. Ding, S. Kiravittaya, Y. Mei, O.G. Schmidt Rolled-Up Optical Microcavities with Subwavelength Wall Thicknesses for Enhanced Liquid Sensing Applications // *ACS Nano*.—2010.— Vol. 4.— № 6.— P. 3123–3130.
25. V. Zamora, A. Díez, M.V. Andrés, B. Gimeno Cylindrical optical microcavities: Basic properties and sensor applications // *Photonics and Nanostructures - Fundamentals and Applications*.—2011.— Vol. 9.— Is.2.—P. 149–158.
26. McFarlane S, Manchee CP, Silverstone JW, Veinot J, Meldrum A. Synthesis and Operation of Fluorescent-core Microcavities for Refractometric Sensing// *J Vis Exp*.— 2013 Vol. 73.— doi: 10.3791/50256.
27. L.N. Acquaroli, R. Urteaga, R.R. Koropeccki Innovative design for optical porous silicon gas sensor // *Sensors and Actuators B: Chemical*.—2010.— Vol.149.— Is. .—P. 189–193.
28. M. A. Santiago-Cordoba, S. V. Boriskina, F. Vollmer, M. C. Demirel Nanoparticle-based protein detection by optical shift of a resonant microcavity // *Applied Physics Letters*.—2011.—Vol. 99.— doi: 10.1063/1.3599706
29. Yi Zou, S. Chakravarty, W. Lai, Ch. Lina, Ray T. Chena Methods to array photonic crystal microcavities for high throughput high sensitivity biosensing on a silicon-chip based platform // *Lab on Chip*.— 2012.— Vol. 12.— P. 2309-2312.
30. M. Yuna, Y. Wana, J. Lianga, F. Xiaa, M. Liua, L. Ren Multi-channel biosensor based on photonic crystal waveguide and microcavities // *Optik - International Journal for Light and Electron Optics*.— 2012.— Vol. 123.— Is. 21.— P. 1920–1922.
31. S. Pal, E. Guillermain, R. Sriram, B. Miller, P. M. Fauchet Microcavities in photonic crystal waveguides for biosensor applications // *Proc. SPIE 7553, Frontiers in Pathogen Detection: From Nanosensors to Systems*.—2010.— doi:10.1117/12.848237

32. S. Arnold, V. R. Dantham, C. Barbre, B. A. Garetz, X. Fan Periodic plasmonic enhancing epitopes on a whispering gallery mode biosensor // *Optics Express*.— 2012.— Vol. 20.— Is. 24.—P. 26147-26159.
33. S. V. Boriskina, L. D. Negro Self-referenced photonic molecule bio(chemical)sensor // *Optics Letters*.— Vol. 35.— Is. 14.—P. 2496-2498.
34. S. Soria, S. Berneschi, M. Brenci, F. Cosi, G. Nunzi Conti, S. Pelli, G. C. Righini Optical Microspherical Resonators for Biomedical Sensing // *Sensors*.— 2011.— Vol. 11.— P. 785-805.
35. A. B. Matsko Practical Applications of Microresonators in Optics and Photonics// CRC Press.—2009.—ISBN 9781420065787.
36. A. W. Poon, F. Xu, X. Luo Cascaded active silicon microresonator array cross-connect circuits for WDM networks-on-chip // *Proc. SPIE 6898, Silicon Photonics III*.— 2008.— doi: 10.1117/12.765090
37. J. Pfeifle, C. Weimann, F. Bach, J. Riemensberger, K. Hartinger, D. Hillerkuss, M. Jordan, R. Holtzwarth, T. J. Kippenberg, J. Leuthold, W. Freude, C. Koos Microresonator-Based Optical Frequency Combs for High-Bitrate WDM Data Transmission // *OSA Technical Digest (Optical Society of America)*. —2012.— doi:10.1364/OFC.2012.OW1C.4
38. I. Lazarou, G. Kanakis, N. Iliadis, D. Kalavrouziotis, G. Pouloupoulos, D. Apostolopoulos, P. Bakopoulos, H. Avramopoulos Bandwidth and Wavelength-Selective MUX/DEMUX Microresonator Elements for Flexible-Grid Applications // *OSA Technical Digest (online) (Optical Society of America)*.— 2015.— doi:10.1364/IPRSN.2015.IT4A.6
39. Y. Okawachi, S. Miller, S. Ramelow, K. Luke, A. Farsi, M. Lipson, A. L. Gaeta Spectrally Efficient Comb Source with Coupled Microresonators // *OSA Technical Digest (online) (Optical Society of America)*.— 2015.— doi:10.1364/CLEO_SI.2015.SM2M.3
40. S. Trebaol, Y. Dumeige, P. Féron High-Q Microresonators: Characterization Method and Application to Amplifying Optical Delay Lines // *(Optical Society of America)*.— 2010.— doi: 10.1364/IPRSN.2010.IME4

41. B. Kuhlow, G. Przyrembel, S. Schlüter, W. Fürst, R. Steingrüber, C. Weimann Photonic Crystal Microcavities in SOI Photonic Wires for WDM Filter Applications // *Journal of Lightwave Technology*.— 2007.— Vol.25.— Is.1.— P.421-431
42. Zhiping Zhou, Bing Yin, Jurgen Mische On-chip light sources for silicon photonics // *Light: Science & Applications*.— 2015.— 4.— e358; doi:10.1038/lsa.2015.131
43. I. Braun, G. Ihlein, F. Laeri, J.U. Nockel, G. Schulz-Ekloff, F. Schuth, U. Vietze, O. Weiß, D. Wöhrle Hexagonal microlasers based on organic dyes in nanoporous crystals // *Applied Physics B*.— 2000.— Vol. 70.— P. 335-343.
44. G. Wirnsberger, G. D. Stucky Microring Lasing from Dye-Doped Silica/ Block Copolymer Nanocomposites // *Chemistry of Materials*.— 2000.— Vol.12.— №9.— P.2525–2527.
45. C. Brüggemann, A. V. Akimov, A. V. Scherbakov, M. Bombeck, C. Schneider, S. Höfling, A. Forchel, D. R. Yakovlev, M. Bayer Laser mode feeding by shaking quantum dots in a planar microcavity // *Nature Photonics*.— 2012.— Vol. 6.— P.30–34.
46. A. Matsudaira, C. Lu, M. Zhang, Sh. Chuang, E. Stock, D. Bimberg Cavity-Volume Scaling Law of Quantum-Dot Metal-Cavity Surface-Emitting Microlasers // *IEEE Photonics Journal*.— 2012.— Vol. 4, №4.— P. 1103-1114.
47. Ce Shi, Soheil Soltani, A.M. Armani Gold Nanorod Plasmonic Upconversion Microlaser // *Nano Letters*.— 2013.— Vol.13.— №12.— P. 5827–5831.
48. А.Б. Андросик, В.Ш. Берикашвили, С.А. Воробьев, П.А. Лучников, С.Д. Мировицкая, А.В. Панков, А.И. Шевченко Микрорезонаторные структуры для коммуникационных систем ВОЛС // *Материалы Международной научно-технической конференции (Москва, 3 – 7 декабря 2012)*.— С. 193-202.
49. M. Pollinger, D. O’Shea, F. Warken, A. Rauschenbeutel Ultrahigh-Q tunable whispering-gallery-mode microresonator // *Physical Review Letters*.—2009.— Vol.103.— Is.5.— P. 053901.
50. S. V. Alyshev, A. O. Zabezhaylov, V. I. Kozlovsky, E. M. Dianov Strained AIBVI nanostructures as active media for visible range ring resonator microlasers // *19th Int. Symp. “Nanostructures: Physics and Technology”*, Ekaterinburg, Russia (June 20–25, 2011).— P.102-103.

51. D. Nilsson, T. Nielsen, A. Kristensen Solid state microcavity dye lasers fabricated by nanoimprint lithography // *Review of Scientific Instruments*.—2004.— Vol.75.—Is. 11.— <http://dx.doi.org/10.1063/1.1794411>.
52. Лазеры на красителях Под ред. Ф.П. Шефер.— М.: Мир.—1976. — С. 330
53. Изучение лазеров на органических красителях. Online access: <http://www.rfe.by/media/kafedry/kaf2/publications/karikh/QRF-rab5.pdf>
54. M. Lebental, J. S. Lauret, R. Hierle, J. Zyss Highly directional stadium-shaped polymer microlasers // *Applied Physics Letters*.— 2006.— Vol. 88.— P. 031108.
55. S. Lozenko, N. Djellali, I. Gozhyk, C. Delezoide, J. Lautru, C. Ulysse, J. Zyss, M. Lebental Enhancing performance of polymer-based microlasers by a pedestal geometry // *Journal of Applied Physics*.— 2012.— Vol. 111.— P.103116.
56. C. Lafargue, S. Bittner, S. Lozenko, J. Lautru, J. Zyss, C. Ulysse, C. Cluzel, M. Lebental Three-dimensional emission from organic Fabry-Perot microlasers // *Applied Physics Letters*.— 2013.— Vol. 102.— P. 251120.
57. I. Gozhyk, S. Forget, S. Chénais, C. Ulysse, A. Brosseau, R. Méallet-Renault, G. Clavier, R. Pansu, J. Zyss, M. Lebental Towards polarization controlled organic microlasers // *Proc. SPIE 8258, Organic Photonic Materials and Devices XIV, 82580K*.— 2012.— doi:10.1117/12.909102
58. M. Lebental, J. S. Lauret, J. Zyss, C. Schmit, E. Bogomolny Directional emission of stadium-shaped microlasers // *Physical Review A*.—2007.— Vol. 75.— P. 033806.
59. M. Lebental, N. Djellali, C. Arnaud, J.-S. Lauret, J. Zyss, R. Dubertrand, C. Schmit, E. Bogomolny Inferring periodic orbits from spectra of simply shaped microlasers // *Physical Review A*.—2007.— Vol. 76.— P. 023830 .
60. I. Gozhyk, G. Clavier, R. Mreallet-Renault, M. Dvorko, R. Pansu, J.-F. Audibert, A. Brosseau, C. Lafargue, V. Tsvirkun, S. Lozenko, S. Forget, S. Chrenais, C. Ulysse, J. Zyss, M. Lebental Polarization properties of solid-state organic lasers // *Physical Review A*.—2012.— Vol. 86.— P. 043817 .
61. E. Bogomolny, N. Djellali, R. Dubertrand, I. Gozhyk, M. Lebental, C. Schmit, C. Ulysse, J. Zyss Trace formula for dielectric cavities. II. Regular, pseudointegrable, and chaotic examples // *Physical Review E*.—2011.— Vol. 83.— P. 036208 .

62. C. Lafargue, M. Lebental, A. Grigis, C. Ulysse, I. Gozhyk, N. Djellali, J. Zyss, S. Bittner Localized lasing modes of triangular organic microlasers // *Physical Review E*.—2014.— Vol. 90.— P. 052922.
63. Tang Jinkui, Zhang Peng Basis for Lanthanide Single-Molecule Magnets // *Lanthanide Single Molecule Magnets*. — Springer Berlin Heidelberg, 2015. — P. 1-39. — ISBN 978-3-662-46998-9
64. А. М. Голуб. Загальна та неорганічна хімія. — К.: Вища школа. — 1971. — Т. 2. — С.416
65. Timmerman D., Izeddin I., Stallinga P., Yassievich I., Gregorkiewicz T. Space-separated quantum cutting with silicon nanocrystals for photovoltaic applications // *Nature Photonics*. —2008. —Vol. 2.—P. 105–109.
66. Е.В. Мальчукова, А.С. Абрамов, А.И. Непомнящих, Е.И. Теруков Алумоборосиликатные стекла, содопированные редкоземельными элементами, как радиационно-защитные покрытия солнечных батарей // *Физика и техника полупроводников*. —2015. — Т. 49. — В.6. — С. 753-757.
67. M. Nakazawa Evolution of EDFA from Single-Core to Multi-Core and Related Recent Progress in Optical Communication // *Optical Review*. — 2014. — Vol. 21. — Is. 6. — P. 862-874.
68. Bouzigues C., Gacoin T., Alexandrou A. Biological applications of rare-earth based nanoparticles // *ACS Nano*. — 2011. — Vol. 11. — P. 84–88.
69. Wang C., Tao H., Cheng L., Liu Z. Near-infrared light induced in vivo photodynamic therapy of cancer based on up-conversion nanoparticles // *Biomaterials*. — 2011. — Vol. 32. — P. 6145–6154.
70. Polman A. Exciting erbium-doped planar optical amplifier materials // *Proc. SPIE 3942, Rare-Earth-Doped Materials and Devices IV, 2*. — 2012. — doi:10.1117/12.382844
71. Quang A., Hierle R., Zyss J., Ledoux I. Demonstration of net gain at 1550 nm in an erbium-doped polymer single mode rib waveguide // *Applied Physical Letters* . —2006. —Vol. 89. — № 14. — P. 141124.

72. Quang A., Zyss J., Ledoux I., Truong V.G., Jurdyc A.-M., Jacquier B., Le D.H., Gibaud A. An hybrid organic–inorganic approach to erbium-functionalized nanodots for emission in the telecom window // *Chemical Physics*. — 2005. — Vol. 318. — № 1–2. — P. 33–43
73. G. Tessari, M. Bettinelli, A. Speghini, D. Ajo, G. Pozza, L. E. Depero, B. Allieri, L. Sangaletti Synthesis and optical properties of nanosized powders: lanthanide-doped Y₂O₃ // *Applied Surface Science*. — 1999. — Vol. 144–145. — P. 686–689.
74. H.M. Ismail, G.A.M. Hussein Texture properties of yttrium oxides generated from different inorganic precursors // *Powder Technology*. — 1996. — Vol. 87. — Is.1. — P. 87-92.
75. G.A.M. Hussein Erbium oxide from erbium acetate hydrate; formation, characterization and catalytic activity // *Powder Technology*. — 2001. — Vol. 118. — Is. 3. — P. 285–290.
76. T. Peng, H. Yang, X. Pu, B. Hu, Z. Jiang, C. Yan Combustion synthesis and photoluminescence of SrAl₂O₄:Eu,Dy phosphor nanoparticles // *Materials Letters*.— 2004.— Vol.58.— Is. 3–4.— P. 352–356.
77. S. Shikao, W. Jiye Combustion synthesis of Eu³⁺ activated Y₃Al₅O₁₂ phosphor nanoparticles // *Journal of Alloys and Compounds*.—2001.— Vol. 327.— Is. 1–2.— P. 82–86.
78. S. Polizzi, S. Bucella, A. Speghini, F. Vetrone, R. Naccache, J.C. Boyer, J.A. Capobianco Nanostructured Lanthanide-Doped Lu₂O₃ Obtained by Propellant Synthesis // *Chemistry of Materials*. — 2004. — Vol. 16. — P. 1330-1335.
79. Konrad, U. Herr, R. Tidecks, F. Kummer, K. Samwer Luminescence of bulk and nanocrystalline cubic yttria // *Journal of Applied Physics*. — 2001.—Vol. 90.— P. 3516-3523.
80. A. M. Gabay, N. G. Akdogan, M. Marinescu , J. F. Liu, G. C. Hadjipanayis Rare earth–cobalt hard magnetic nanoparticles and nanoflakes by high-energy milling // *Journal of Physics: Condensed Matter*.— 2010.— Vol. 22.— № 16.— P. 1-6.
81. T. Tsuzuki, P.G. McCormick Mechanochemical synthesis of metal sulphide nanoparticles // *Nanostructured Materials*.— 1999.— Vol.12.—Is. 1–4.— P.75–78.

82. R. Srinivasan, R. Yogamalar, A. Bose Structural and optical studies of yttrium oxide nanoparticles synthesized by co-precipitation method // *Materials Research Bulletin*.— 2010.— Vol.45.— Is. 9.— P. 1165–1170.
83. B. Allieri, L. E. Depero, A. Marino, L. Sangaletti, L. Caporaso, A. Speghini, M. Bettinelli Growth and microstructural analysis of nanosized Y₂O₃ doped with rare-earths // *Materials Chemistry and Physics*. — 2000. — Vol. 66. — P. 164–171.
84. J. Dhanaraj, R. Jagannathan, T.R.N. Kutty, C.-H. Lu Photoluminescence Characteristics of Y₂O₃:Eu³⁺ Nanophosphors Prepared Using Sol–Gel Thermolysis // *The Journal of Physical Chemistry*. — 2001. — Vol.105.— № 45.— P. 11098–11105.
85. F. Mangiarini, R. Naccache, A. Speghini, M. Bettinelli, F. Vetrone, J.A. Capobianco Upconversion in Er³⁺-doped Gd₂O₃ nanocrystals prepared by propellant synthesis and flame spray pyrolysis // *Materials Research Bulletin*.— 2010.— Vol. 45.— Is. 8.— P. 927–932.
86. A. M. Pires, O. A. Serra, M. R. Davolos Morphological and luminescent studies on nanosized Er, Yb–Yttrium oxide up-converter prepared from different precursors // *Journal of Luminescence*.— 2005.— Vol. 113.— P. 174–182.
87. T. Ye, Z. Guiwen, Z. Weiping, X. Shangda Combustion synthesis and photoluminescence of nanocrystalline Y₂O₃:Eu phosphors // *Materials Research Bulletin*.—1997.— Vol.32.—№ 5, P. 501-506.
88. S. Hosokawa, S. Iwamoto, M. Inoue Synthesis of nanocrystalline rare earth oxides by glycothermal method // *Materials Research Bulletin*.— 2008.— Vol. 43.— P. 3140–3148.
89. R. Bazzi, M.A. Flores, C. Louis, K. Lebbou, W. Zhang, C. Dujardin, S. Roux, B. Mercier, G. Ledoux, E. Bernstein, P. Perriat, O. Tillement Synthesis and properties of europium-based phosphors on the nanometer scale: Eu₂O₃, Gd₂O₃:Eu, and Y₂O₃:Eu // *Journal of Colloid and Interface Science*.— 2004.— Vol. 273.— P. 191–197.
90. M.Ou, B. Mutelet, M. Martini, R. Bazzi, S. Roux, G. Ledoux, O. Tillement, P. Perriat Optimization of the synthesis of nanostructured Tb³⁺-doped Gd₂O₃ by in-situ luminescence following up // *Journal of Colloid and Interface Science*.— Vol. 333.— Is. 2.— P. 684–689.

91. R. Bazzi, A. Brenier, P. Perriat, O. Tillement Optical properties of neodymium oxides at the nanometer scale // *Journal of Luminescence*.— 2005.— Vol. 113.— P. 161–167.
92. F. Goubard, F. Vidal, R. Bazzi, O. Tillement, C. Chevrot, D. Teyssie Synthesis and luminescent properties of PEO/lanthanide oxide nanoparticle hybrid films // *Journal of Luminescence*.— 2007.— Vol. 126.— P. 289–296.
93. Фокина М.И., Собещук Н.О., Денисюк И.Ю. Исследование процессов формирования полимерного микроэлемента на торце оптического волокна в условиях значительного ингибирующего влияния кислорода на процесс фотополимеризации// *Известия вузов. Приборостроение*.—2011.— №03.—С.69-75.
94. M. Hocinea, R. Bachelot, C. Ecoffet, N. Fressengeasa, P. Royerb, G. Kugel End-of-fiber polymer tip: manufacturing and modeling// *Sythetic Metals*.— 2002.— №127.— P313-318.
95. N. Suzuki, Y. Tomita, T. Kojima Holographic recording in TiO₂ nanoparticle-dispersed methacrylate photopolymer films // *Applied Physics Letters*.— 2002.— Vol. 81.— №22.— P. 4121–4123.
96. Y. Tomita, N. Suzuki, K. Chikama Holographic manipulation of nanoparticle distribution morphology in nanoparticle-dispersed photopolymers // *Optics Letters*.— 2005.—Vol. 30.— №8.— P.839–84.
97. Sergii Lozenko. Heavy metal ion sensors based on organic microcavity lasers. Other. Ecole normale superieure de Cachan - ENS Cachan, 2011. English // HAL Id: tel-00744846
98. H. Lorenz, M. Despont, N. Fahrni, N. LaBianca, P. Renaud, P. Vettiger SU-8: A low-cost negative resist for MEMS // *Journal of Micromechanics and Microengineering*.—1997.— Vol. 7.— P. 121–124.
99. Composition for photo imaging: US patent No. 5304457 // R. A. Day, J.D. Gelorme, D. J. Russell, S. J. Witt.— 1994.

100. S. Jiguet, A. Bertsch, M. Judelewicz, H. Hofmann, P. Renaud SU-8 nanocomposite photoresist with low stress properties for microfabrication applications // *Microelectronic Engineering*.— 2006.— Vol. 83.— Is. 10.— P. 1966–1970.
101. H. Lorenz, M. Despont, P. Renaud High-aspect-ratio, ultrathick, negative-tone near-UV photoresist and its applications for MEMS // *Sensors and Actuators A: Physical*.— 1998.— Vol. 64.— Is. 1.— P. 33–39.
102. В.К. Варадан, К.Д. Виной, К.А. Джозе ВЧ МЭМС и их применение // *Техносфера*.— 2008.— С. 528.— ISBN 5-94836-030-X.
103. MicroChem datasheets SU-8 2002-2025, SU-8 2025. Online access: <http://www.microchem.com/Prod-SU82000.htm>
104. S. Kuo, C. Lin Fabrication of aspherical SU-8 microlens array utilizing novel stamping process and electrostatic pulling method // *Optics express*.—2010.—Vol. 18.—№18.— P. 19114-19119.
105. J. Serbin, A. Egbert, A. Ostendorf, B. N. Chichkov Femtosecond laser-induced two-photon polymerization of inorganic–organic hybrid materials for applications in photonics // *Optics Letters*.— 2003 .—Vol. 28.—№ 5.— P.301-303.
106. Chen V. W., Sobeshchuk N., Lafargue C., Mansfield E. S., Yom J., Johnstone L., Hales J. M., Bittner S., Severin Charpignon, Ulbricht D., Lautru J., Denisyuk I., Zyss J., Perry J. W., Lebental M. Three-Dimensional Organic Microlasers with Low Lasing Thresholds Fabricated by Multiphoton and UV Lithography // *Optics Express*.— 2014.—Vol. 22.—Is. 10.— P. 12316-12326
107. Online access: <http://www.nanoscribe.de/en/>
108. Iryna Gozhyk. Polarization and gain phenomena in dye-doped polymer microlasers. *Optics*. Ecole normale supérieure de Cachan - ENS Cachan, 2012. English.— HAL Id: tel-00785721
109. I. Gozhyk, M. Boudreau, H. Rabbani Haghighi, N. Djellali, S. Forget, S. Chenais, C. Ulysse, A. Brosseau, R. Pansu, J.-F. Audibert, S. Gauvin, J. Zyss, M. Lebenta Gain properties of dye-doped polymer thin films // <http://arxiv.org/pdf/1403.7461.pdf>

110. Burunkova J., Denisyuk I.Yu., Bulgakova V., Kokenyesi S. TiO₂-acrylate nanocomposites elaborated by UVcuring with tunable properties // *Solid State Phenomena*. 2013. V. 200. P. 173–177.
111. Burunkova J., Denisiuk I., Vorzobova N., Daroczi L., Hegedus Cs., Charnovych S., Kokenyesi S. Fabrication and characterization of gold/acrylic polymer nanocomposites // *European Polymer Journal*. 2013. V. 49. № 10. P. 3072–3077.
112. Denisyuk I., Burunkova J., Kokenyesi S, Bulgakova V., Fokina M. Optical nanocomposites based on high nanoparticles concentration and its holographic application // *Book Nanocrystals / Ed. by Sudheer Neralla*. Croatia: InTech Europe, 2012. P. 81–102.
Online access: <http://www.intechopen.com/articles/show/title/optical-nanocomposites-based-on-high-nanoparticles-concentration-and-its-holographic-application>
113. Z. Hasan, S. Dardona, A. Konjhodzic Photoluminescence and spectral holeburning in europium-doped MgS nanoparticles // *The Journal of Chemical Physics*.— 2005.— Vol. 123.— P. 224715
114. T.R. Ravindran, A. K. Arora, B. Balamurugan, B.R. Mehta Inhomogeneous broadening in the photoluminescence spectrum of CdS nanoparticles // *NanoStructured Materials*.— 1999.— Vol. 11.— № 5.— P. 603–609.

Table 1 — List of materials used in the work

Product name	Supplier, №	Chemical formula	Note
Bisphenol A glycerolate (1 glycerol/phenol) diacrylate	Aldrich, 411167	$C_{27}H_{32}O_8$	Liquid diacrylate
2-Carboxyethyl acrylate (2Car)	Aldrich, 552348	$CH_2=CHCO_2(CH_2)_2CO_2H$	The surface-active liquid monoacrylate
Ethylene glycol phenyl ether acrylate (PEA)	Aldrich, 408336	$H_2C=CHCO_2CH_2CH_2OC_6H_5$	Liquid linear acrylate
Silica, 14 nm	Aldrich, 066K0110	SiO_2	Nanoparticles
2,2-Dimethoxy-2-phenylacetophenone (InII)	Aldrich, 196118	$C_6H_5COC(OCH_3)_2C_6H_5$	Polymerization photoinitiator sensitive in UV
1-Butanol	«Ekros-1», GOST 6006-78	$C_4H_{10}O$	Solvent
Glycerol		$C_3H_5(OH)_3$	Trihydric alcohols
Erbium(III) chloride	Aldrich, 449792	$ErCl_3$	
Ytterbium(III) chloride	Aldrich, 439614	$YbCl_3$	
Dichloromethane	«Ekros-1»	CH_2Cl_2	Organic solvent
Sodium hydroxide, aqueous solution	«Ekros-1», GOST 4328-77	$NaOH$	Alkaline solution

Continuation of the Table 1

Dimethylformamide (DMF)	«Reahim», GOST 20189-74	$(\text{CH}_3)_2\text{NC}(\text{O})\text{H}$	The polar aprotic solvent
Isopropyl alcohol	«Vekton»	$\text{CH}_3\text{CH}(\text{OH})\text{CH}_3$	Organic solvent
Zinc oxide		ZnO	Inorganic nanoparticles, 20 nm
SU8	MicroChem		Negative epoxy based photoresist
Rhodanime 640 perchlorate	Exciton, 06400	$\text{C}_{32}\text{H}_{31}\text{N}_2\text{O}_3 \cdot \text{ClO}_4$	Organic dye
Pyromethene 597	Exciton, 05970		Organic dye
DCM	Exciton, 06490	$\text{C}_{19}\text{H}_{17}\text{N}_3\text{O}$	Organic dye
Pyromethene 605	Exciton, 06050	$\text{C}_{20}\text{H}_{27}\text{N}_2\text{O}_2\text{BF}_2$	Organic dye
SU8 developer	MicroChem		

3D organic microlasers fabrication by UV-lithography (clean room of Institut d'Alembert, ENS de Cachan)

1) SU8 dye solution preparation (SU8 2025: Pyrromethene 597, Rhodamine 640)

Preliminary bottle for solution (with the cap) was weighed. After it was cleaned by acetone; acetone residues were washed away by isopropanol before their evaporation. At the final stage bottle was dried by compressed nitrogen.

At first, 10-20 gram of photoresist were poured into the bottle and weighted. Next, the calculation of pure monomer mass in the resist were performed, particularly for SU8 2025 the percentage of monomer was 68.55% due to the total weight of the photoresist. Based on the obtained value, the amount of the dye necessary for obtaining structure with the desired concentration of the dye in the polymer matrix was calculated. In most cases, the concentration was 0.5% weight percent. Attempts to increase the concentration were not very successful; Pyrromethene 597 solubility limit in SU8 2025 is 0.8% wt.

Weighing dye was carrying out by adding it in the bottle by small portions. It is possible to weight it in one portion using special weighing containers available in the clean room, but a significant amount of dye is used to remain in the container.

Further, pre-weighted magnetic stir bar were placed into the bottle. Stir bar desirable to put in the middle of the resist surface. In this way, immersing in the resist stir bar will move the dye into the resist volume. This contributes to fewer undissolved dye on the bottle walls.

It is easier to put the resist in the bottle first and after add the necessary amount of the dye. SU8 2025 is rather viscous and it is difficult to weight precise amount without using additional stuff.

For its homogenization solution was treated by ultrasonic and magnetic stirring. At first, bottle with the solution was placed in a cylindrical bowl with water, which was placed in the ultrasonic bath for 30-40 minutes. It was controlled that the temperature of

solution did not exceed the T_g for the SU-8 which is about 55°C. No additional heating was used; solution became warm just due to mechanical nature of ultrasonic action. Then the warm solution (with lower viscosity due to the heating) was stirred until it gets to the room temperature. At room temperature the stir bar moving is stopped by solution viscosity. Repetition of 7-10 cycles (as a cycle we mean on iteration of ultrasonic (40min) and subsequent stirring) provides dye dissolution. The technology of the dye introduction does not depend on the specific laser dye.

It is better not to use the solution for the film deposition on the day of preparation, it is better to leave it overnight for maximum dissolution.

2) Resist deposition on the substrate

The photoresist deposition on the substrate was implemented by spin-coating. In this work, experiments were performed on two different substrates: silicon wafer covered by 2µm silica layer (bought from Process Specialties) and borax-silica glass slides (1mm thickness, cleanroom cleaned, supplied by Schott Nexterion). Also it is possible to use non pre-cleaned glass wafers. In this case wafers were wiping by fiber napkin soaked in ethyl alcohol; after cleaned by acetone, which was fully wash away by isopropanol.

Before resist deposition the silicon substrate (4 inches diameter) was divided into 4 equal parts with a diamond cutter. Glass wafer with standard elongated rectangular shape also was divided into 2-3 parts.

Since substrates size is smaller than the size of the spin-coater holder for samples it's desirable to use paraffin film for sample fixing. A rectangular piece of film with a small hole slotted in the middle (the square with 5-8 mm side) is placed between the substrate and the holder. Using paraffin film prevents wicking solution with the dye into the vacuum feeder mechanism. After deposition the substrate was cleaned again from dust with compressed nitrogen. The resist was placed on substrate so that a drop of photoresist completely covers the center of the substrate. After deposition of the resist it is better to wait to 20-30 seconds allows resist distributes uniformly over the surface of the substrate.

The spin-coating speed mode consists of two parts: slow rotation for the uniform distribution of the resist on the substrate and the fast rotation, which speed is determined by the targeted thickness.

Table 1 shows data for several speed modes being used in the work. Measurement of the thickness were carrying out at the center of the films; the edges thickness is higher.

Table 1 — The dependence of the film thickness on deposition speed

Speed I, RPM	Acceleration I, RPM/second	Time I	Speed II, RPM	Acceleration II, RPM/second	Time II	Film thickness, MKM
500	100	5	3000	300	60	20-22
500	100	5	2000	300	60	24-27
500	100	5	1000	300	60	38-44

3) Soft Bake Procedure

After the film deposition, the soft bake procedure follows. Before putting the sample on the hotplate it is necessary to remove excess photoresist from the back side of the sample with napkin soaked in acetone.

Recommended by producer Soft Bake mode for such film thickness is 3-6 minutes at 95°C. However, in our case, after this time the film still contains sufficient amount of solvent - resist is not a solid film, but rather viscous liquid layer. For thicker films MicroChem recommends two-stage drying: relaxation of the film at 65°C and drying at 95°C.

For all samples, the same mode of drying was used: 5-7 minutes at 65°C, and 40-60 minutes at 95°C. The duration of the second stage can be adjusted with respect to the film thickness. Soft Bake mode does not depend on the used dye.

4) Exposure step

The exposition step was performed on the commercial lithography setup Manual Mask Aligner MJB4 by Suss MicroTec operating with i-line of mercury lamp (exposure power was 17.3 mJ/cm^2).

Irradiation occurred at 1 cycle in mode "soft contact". Exposition was carrying out through negative chrome masks designed specifically for that purpose and produced by Photronics company (the mask scale was 1:1). For pure resist exposure time depends on the power of the radiation and the thickness of the film. The irradiation time was modified individually for each dye and varied depending on the thickness of the film. Dye concentration also has influence on the exposure time. Values shown below were obtained for the mass concentration 0.5%.

Table 2 — The exposure time dependance on the thickness of the resist film (for Rhodamine 640, a silicon substrate)

Thickness, μm	Exposure time, sec
25	100
40	150
100-150	200-250

For a glass substrate exposure time should be increased in 1,5 times compared with the samples on a silicon substrate.

For Pyrromethene 597 exposure time is 17-19 seconds for films of 20-40 μm thickness. Resist doped by PM 597 it is more sensitive to exposure changes. Increasing exposure time on 1-2 seconds for 25 microns thickness film results in significant deterioration of the structures surface due to overexposure.

5) Post Exposure Bake

Post-exposure thermal treatment of the photoresist (PEB) includes heating of irradiated sample for its polymerization (in exposed areas). For the considered range of thicknesses MicroChem recommends to heat sample for 0-3 minutes at 65°C and for 4-7

min at 95°C. As well as for Soft Bake, PEB time was increased too: 3 minutes (65°C) and 10 minutes (95°C).

It is worth noting that in the result of heating at 65°C on the surface of the sample should begin to appear the outlines of microstructures. If it does not, it means that the exposure was unsuccessful.

6) Development

After PEB sample must be cooled to room temperature (3-5 minutes). Washing out uncured resist takes place during development process. The sample is placed in a bowl with developer (SU-8 developer) for 5 minutes. After it is possible to check did all unpolymerized material was washed away. For this purpose the sample should be removed with tweezers and gently flush with isopropyl alcohol in another bowl. The presence of white traces indicates the undissolved residues of the resist. After this, sample must be put back in the developer, but for a shorter period of time (e.g., 2 minutes). Repeat the washing in isopropanol. Repeat washing in a developer as needed. The third and subsequent times better to put the sample in the developer for 1 minute, not longer. For sufficiently thicker microstructures total development time increases from 7-8 minutes to 10-12 minutes. After the final wash sample should be dried with compressed air.

Titre : Micro-lasers à base de polymères composites (en français)

Mots clés : micro-lasers, matériaux organiques, composants tridimensionnels

Résumé : L'objectif de la thèse est la fabrication et caractérisation de microlasers 3D à base de polymères dopés par des colorants organiques et des nanoparticules d'erbium et Ytterbium.

Au début, nous avons étudié des structures polymères avec de très bons facteurs d'aspect, ainsi que le déplacement de nanoparticules lors de l'exposition à un éclairage périodique.

La réalisation majeure de cette thèse est l'obtention de microlasers 3D par lithographie UV. Ensuite nous avons comparé les seuils lasers de ces structures pour différentes méthodes de fabrication.

Dans des micro-cubes, nous avons identifié des orbites périodiques planes en forme de carré. L'analyse des orbites périodiques dans des microlasers Fabry-Perot 3D a montré que leur forme dépend du colorant, de la nature du substrat et de la taille de la structure (largeur et épaisseur).

La dernière partie de ce travail consiste en la synthèse de nanoparticules d'oxyde d'erbium et ytterbium à basse température et en milieu anhydre. Ces nano-particules ont ensuite été introduites dans des composites à base de polymères qui ont donné lieu à la fabrication de micro-lasers 3D et à leur caractérisation.

Title : Micro-lasers based on polymer composites (in English)

Keywords : Micro-lasers, organic materials, tridimensional device

Abstract: The aim of the thesis is the fabrication and optical characterization of three-dimensional organic microlasers based on organic dyes and luminescent erbium/ytterbium nanoparticles.

At the beginning, we considered submicron polymer structures with high aspect ratio, as well as the phenomenon of redistribution of nanoparticles in the volume of the composite during the exposure by a periodic light field pattern.

The main part of the work is devoted to obtaining three-dimensional polymer microlasers by UV-lithography. Comparison of the lasing threshold for microcavities obtained by different methods was performed.

Periodic orbits in cuboid microlasers with square cross-section were identified. Analysis of possible periodic orbits in microlasers Fabry-Perot showed that the shape of the orbit depends on the dye, the type of substrate and the size of the microlaser (width, height). The last part of the work contains a study of low-temperature synthesis of luminescent nanoparticles of erbium and ytterbium oxides in a anhydrous medium, and polymer composites based on them. Three dimensional organic microlasers doped by these luminescent nanoparticles were obtained and investigated.

